SAPIENZA
UNIVERSITÀ DI ROMA

DIPARTIMENTO DI INGEGNERIA ASTRONAUTICA, ELETTRICA ED ENERGETICA

DOTTORATO DI RICERCA IN INGEGNERIA AEROSPAZIALE
CICLO XXV

THE GEODESY OF MERCURY WITH THE MISSIONS MESSENGER AND BEPICOLOMBO

Author
Antonio Genova

Advisor
Prof. Luciano Iess

ANNO ACCADEMICO 2011-2012

To my family. Their support, encouragement,
and constant love have always sustained me.

To Federica. We have shared fabulous years
together. The best is yet to come.

"... I leave here believing more than I had
And there's a reason
A reason I'll be back ..."

No Ceiling, Eddie Vedder

Acknowledgements

Working on the Ph.D. has been a wonderful and all-involving experience. This thesis has benefited greatly from the support of many people, some of whom I would sincerely like to thank here.

First of all, I am deeply grateful to my advisor Prof. Luciano Iess. He has been a steady influence throughout my Ph.D. career. He has oriented and supported me with promptness and care, and has always been patient and encouraging in times of new ideas and difficulties.

Furthermore, I am very grateful to Prof. David E. Smith for his support, and for many motivating discussions. I have been very privileged to collaborate with him and his team at the NASA's Goddard Space Flight Center.

Finally, I would like to thank my colleagues of the Radio Science Laboratory at "La Sapienza" University of Rome I had the pleasure to work with. They make a really good team.

Table of Contents

List of Figures

List of Tables

Introduction

Mercury is the innermost planet of the solar system and the eighth in size and mass. Its closeness to the Sun and its smallness make it the most elusive of the planets visible to the unaided eye. Because its rising or setting is always within about two hours of the Sun's, it is never observable when the sky is fully dark.

Even in more recent eras, many sky observers passed their entire lifetimes without ever seeing Mercury. It is reputed that Nicolaus Copernicus, whose heliocentric model of the heavens in the 16th century explained why Mercury and Venus always appear in close proximity to the Sun, expressed a deathbed regret that he had never set eyes on the planet Mercury himself[1]. Until the last part of the 20th century, Mercury was one of the least-understood planets, and even now the shortage of information about it leaves many basic questions unsettled. Indeed, the length of its day was not determined until 1960s, and, even after the flybys of the Mariner 10 probe, the surface of the planet had not been completely observed. At first glance the portion of the planet that has been imaged looks similar to the cratered terrain of the Moon, an impression reinforced by the roughly comparable size of the two bodies.

Mercury is far denser, however, having a metallic core that takes up about *61%* of its volume (compared with *4%* for the Moon and *16%* for Earth) showing not conformity with the other terrestrial planets, nor with the Moon. Mercury's high density suggests that it has a large core, accounting for *70-80%* of the planet's mass.

A possible theory that explains why Mercury has such a large core is that it was impacted by a large planetesimal early in its history (Solomon et al., 2007). The impact would have stripped away much of the planet's crust, leaving just the thick iron core. This is a similar process that explains the formation of the Moon. It's also possible that Mercury formed before the Sun's energy output settled down. If it had twice its original mass, the Sun could vaporize the surface of the planet, blasting it away with its power solar wind.

The determination of Mercury's deep interior provides, therefore, crucial information to the formation and evolution of the solar system. In absence of a network of

[1] http://www.britannica.com

seismometers on the surface, the only available experimental tool is the measurement of the planet's gravity and rotational parameters by means of a deep space probe. Such an experiment requires a combination of precise positioning of the spacecraft with respect to the planet and an accurate referencing of the planet's surface to an inertial frame. Radio links between spacecraft and Earth stations provide accurate measurements of spacecraft relative position and velocity (range and range rate) that contribute significantly to achieving these geophysics objectives (Iess and Boscagli, 2001). Most of the present knowledge on the planetary gravity fields and interiors has been derived from accurate spacecraft tracking and precise orbit determination, referred to as radio science experiment. Interplanetary tracking systems rely on microwave links for obtaining the key navigation data, namely the frequency and propagation time of radio signals. These observables quantities are input to complex orbit determination codes, where the observed quantities are compared with their predicted values to produce an estimate of the spacecraft state and other parameters of the model. In planetary geodesy, the estimated quantities are typically the coefficients of the spherical harmonics expansion of a gravity field.

A confluence of events now allows for an intensive study of Mercury by means of interplanetary space probes. The National Aeronautics and Space Administration (NASA) and the European Space Agency (ESA) developed two independent missions to Mercury. MESSENGER (MErcury Surface, Space ENvironmentm GEochemestry, and Ranging), selected by NASA in July 1999 has been orbiting about Mercury since March 11, 2011. The ESA dual-spacecraft mission BepiColombo will be inserted in orbit about Mercury in 2022. Both missions are equipped with on board radio science instrumentation necessary to the estimation of Mercury's gravity field and interior structure. The MESSENGER radio frequency telecommunications subsystem operates only at X-band frequencies (Srinivasan et al., 2007) entailing high plasma noise on range and range rate measurements. The Mercury Orbiter Radio science Experiment (MORE) of the mission BepiColombo was designed to provide an accurate estimation of Mercury's gravity field by means of high stable, multi-frequency radio link in X and Ka band. Accurate range and range rate measurements are possible using the plasma noise cancellation system, developed for the Cassini mission (Asmar et al., 2005; Tortora et al., 2004). Furthermore, the spacecraft hosts a high sensitivity accelerometer ISA (Italian Spring Accelerometer) that removes to a large extent the dynamical noise from non-gravitational accelerations (Iafolla and Nozzoli, 2001). In this work we report on a new set of numerical simulations of the BepiColombo radio science experiment taking into account the development in the new spacecraft design, the mission profile and the tracking system. In this context we have developed the orbit determination procedures, referred to as batch-sequential processing.

In September 2011, the MESSENGER radio tracking data of the first six months of operations were published with the ancillary information necessary for the MESSENGER orbit determination. This data set has offered an excellent opportunity to test the batch-sequential processing and furthermore, to estimate preliminary the Hermean gravity field.

Therefore, we present here the results of our analysis of the first six months of the MESSENGER radio tracking data that provides a model of Mercury's gravity field.

The knowledge of the lower spherical harmonics of the gravity field allows us not only to determine the interior structure of Mercury, but also to predict accurately the orbital evolution of BepiColombo spacecraft. This last goal is especially important for the planning of the ESA mission, as the maneuvering capabilities of both spacecraft are very limited and the perturbations to the orbital elements depend crucially on the gravity field and the initial conditions.

The work is organized in six chapters.

Chapter 1 introduces briefly the exploration of Mercury highlighting the generic characteristics of the planet and its research with space probes.

Chapter 2 is focused on the orbit determination for the geodesy of Mercury. We present here the overall description of radio science experiments, showing the measurements and the geodetic models, and the codes of the orbit determination for interplanetary spacecraft.

Chapter 3 describes the MESSENGER mission and radio science experiment. Here, we report on the analysis of the radio tracking data showing the orbit reconstruction and the estimated model of the Hermean gravity field and ephemeris.

Chapter 4 is about the mission BepiColombo and the Mercury Orbiter Radio science Experiment. We carried out a new set of numerical simulations that provides attainable accuracies in the gravity field estimation.

Chapter 5 summarizes the consequences of the estimated Hermean gravity field on the geodesy of the planet and the orbit evolution of the BepiColombo spacecraft.

Chapter 6 gives conclusions about our work.

Chapter 1

The exploration of Mercury

Outline. Mercury is the innermost planet of the solar system and, thereby, a difficult object to study by astronomical observation and spacecraft exploration. A substantially improved knowledge of the planet Mercury is nonetheless critical to our understanding of how the terrestrial planets formed and evolved. Determining the surface composition of Mercury, a body with a ratio of metal to silicate higher than any other planet or satellite, provide a unique window on the processes by which planetesimals in the primitive solar nebula accreted to form planets. Despite this great interest, Mariner 10 had been the only spacecraft to visit Mercury before 2007. Its three flybys, more than *30* years ago, yielded the first view of this little-understood world. With advances in spacecraft technology, two missions have been developed for more intensive Mercury exploration. The first one is the MESSENGER (MErcury Surface, Space ENvironment, GEochemistry and Ranging) mission, competitively selected under the NASA Discovery Program, which sent a spacecraft to flyby Mercury in 2007 and 2008 and to orbit Mercury for one Earth year (nominal mission) extended to an other year. The second is the more comprehensive BepiColombo mission, consisting in two orbiters: the Mercury Planetary Orbiter (MPO) and the Mercury Magnetospheric Orbiter (MMO), which will orbit Mercury in 2022. Synergetic strategies of exploration enable efficient use of BepiColombo resources in a more detailed study of the planet.

1.1 The planet Mercury

Mercury is an important target of planetary exploration in the solar system. It is the smallest of the terrestrial planets, but its density (corrected for self-compression) and by inference its mass fraction of metal are the highest of any planet in the solar system. Its ancient surface suggests that internal geological activity ceased earlier than on any other terrestrial planet, yet it retains a global magnetic field of internal origin. As the closest planet to the Sun, Mercury displays the largest range in diurnal temperature in the solar system, but the floors of its polar craters remain sufficiently cold to trap highly volatile species. It is the only solar system body locked in a spin-orbit resonance where the ratio

of orbital period to spin period is precisely *3:2* (unlike the more common *1:1*, as for the Moon). Mercury's atmosphere is both the most tenuous and the most strongly variable among the terrestrial planets and the only atmosphere in which such crustally derived elements as sodium, potassium, and calcium are major constituents.

A further context in which to regard Mercury's unusual attributes is provided by the recent discovery of planets and planetary systems in orbit about other stars. While the extra-solar planets documented to date are all analogues to the gas-giant planets of our solar system, the orbital parameters of Mercury fall within those of known extra-solar planets, and Mercury provides our nearest laboratory for studying planetary system processes in the vicinity of a host star. Further, a variety of efforts are under way to detect and characterize extra-solar Earth-like planets, and Mercury provide a relevant point of comparison with those less than 1 Astronomical Unit (AU) from their parent star.

1.1.1 Interior structure

Mercury is one of four terrestrial planets in the solar system with a mass and an equatorial radius of respectively 3.302×10^{23} *kg* and *2439.7 km* (Anderson et al., 1987). Mercury's uncompressed density (about $5300\ kg\ m^{-3}$), the highest of any planet, has long been taken as evidence that iron is the most abundant contributor to the bulk composition. Interior structure models in which a core has fully differentiated from the overlying silicate mantle indicate that the core radius is approximately 75% of the planetary radius and the fractional core mass is about 60% if the core is pure iron (Solomon et al., 2007); still larger values are possible if the core has a light element such as sulfur alloyed with the iron. Such a metallic mass fraction is at least twice that of the Earth, Venus, or Mars (Figure 1.1).

Calculations of dynamically plausible scenarios for the accretion of the terrestrial planets permit a wide range of outcomes for Mercury. Given an initial protoplanetary nebular disk of gas and dust, planetesimals accrete to kilometer size in 10^4 years (Weidenschilling and Cuzzi, 1993), and runaway growth of planetary embryos of Mercury- to Mars-size accrete by the gravitational accumulation of planetesimals in 10^5 years (Kortenkamp et al., 2000). During runaway growth, Mercury-size bodies can experience substantial migrations of their semimajor axes. Furthermore, each of the terrestrial planets probably formed from material originally occupying a wide range in solar distance, although some correlation is expected between the final heliocentric distance of a planet and those of the planetesimals from which it formed.

Three explanations for the high metal fraction of Mercury have been put forward. The first invokes differences in the response of iron and silicate particles to aerodynamic drag by nebular gas to achieve fractionation at the onset of planetesimal accretion (Weidenschilling, 1978). The second and third explanations invoke processes late in the planetary accretion process, after the Mercury protoplanet had differentiated silicate mantle from metal core. In one, the high metal content of Mercury is attributed to

preferential vaporization of silicates by radiation from a hot nebula and removal by a strong solar wind (Cameron, 1985; Fegley Jr. and Cameron, 1987). In the other, selective removal of silicate occurred as a result of a giant impact (Benz et al., 1988; Wetherill, 1994).

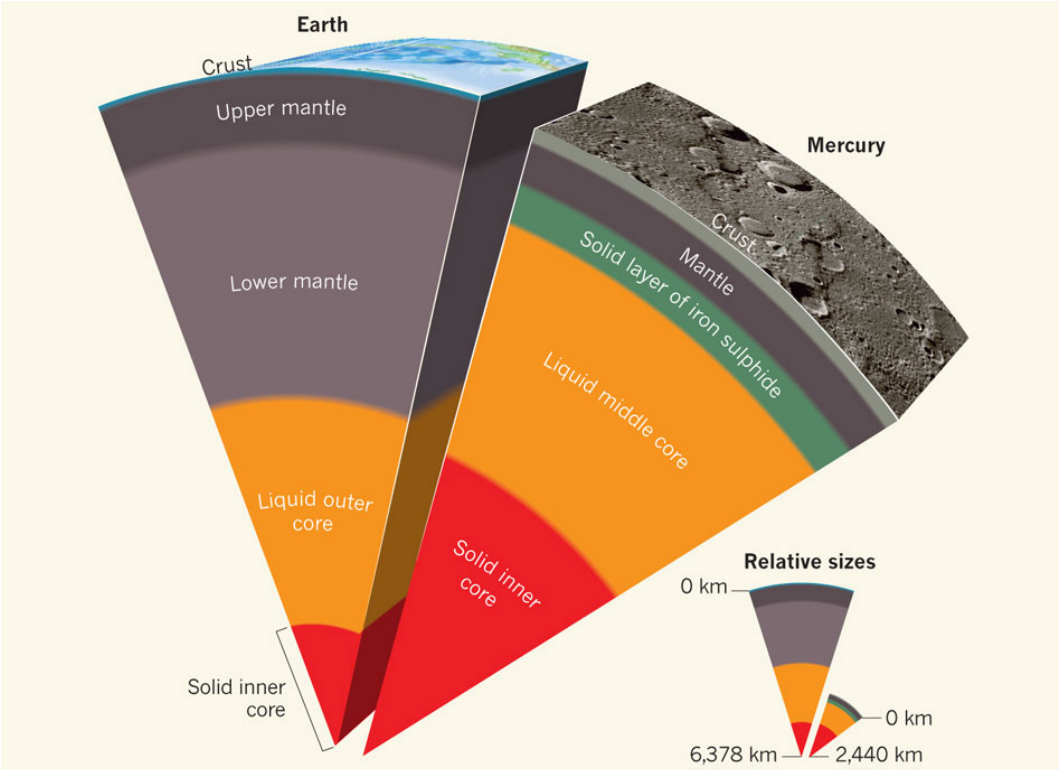

Figure 1.1 Internal structure of Earth and Mercury (Stevenson, 2012)

These three hypotheses lead to different predictions for the bulk chemistry of the silicate fraction of Mercury (Lewis, 1988; Boyton et al., 2007). Present information on the chemistry and mineralogy of the surface of Mercury, however, is still limited to distinguish clearly among the competing hypotheses. Substantial progress on understanding the composition of Mercury may be provided with remote sensing by orbiting spacecraft.

Also important to an assessment of bulk composition and formation hypotheses is the estimation of the thickness of Mercury's crust and the radius of Mercury's core. The thickness can be estimated by a combined analysis of gravity and topography measurements if such data are sensitive to variations on horizontal scales of several hundred kilometers and greater. An upper bound on crustal thickness can also be obtained from isostatically compensated long-wave-length topographic variations, on the grounds that the temperature at the base of the crust cannot be so high that variations in crustal

thickness are removed by viscous flow on timescales shorter than the age of the crust (Solomon et al., 2007).

An observation that can demonstrate the existence and determine the radius of a liquid outer core on Mercury is the measurement of the amplitude of Mercury's forced physical libration. The physical libration of the mantle (manifested as an annual variation in the spin rate about the mean value) is the result of the periodically reversing torque on the planet as Mercury rotates relative to the Sun. The amplitude of this libration ϕ_0 is approximately equal to $(B-A)/C_m$ where A and B are the two equatorial principal moments of inertia of the planet and C_m is the polar moment of inertia of the solid outer shell (Peale, 1988). The moment differences also appear in expressions for the second–degree coefficients of the planetary gravity field expanded in spherical harmonics. The latter relations, the libration amplitude, and an expression resulting from Mercury's resonant state and relating the planet's small but non-zero obliquity to moment differences and other orbital parameters together yield C_m/C, where C is the polar moment of inertia of the planet (Peale, 1988). The quantiy C_m/C is *1* for a completely solid planet and about *0.5* if Mercury has a fluid core.

Two conditions on the above relationship for ϕ_0 are that the fluid outer core does not follow the *88-day* physical libration of the mantle and that the core does follow the mantle on the time scale of *~300 000-year* precession of the spin axis (Peale, 1988). These constraints lead to bounds on the viscosity of outer core material, under the assumption that coupling between the outer core and solid mantle is viscous in nature, but the bounds are so broad as to be readily satisfied. Alternative core–mantle coupling mechanisms, including pressure forces on irregularities in the core–mantle boundary, gravitational torques between the mantle and an axially asymmetric solid inner core, and magnetic coupling between the electrically conductive outer core and a conducting layer at the base of the mantle, do not violate either of the required conditions (Peale et al., 2002).

The BepiColombo mission will determine accurately the four quantities needed to determine whether Mercury has a fluid outer core. Up to the present, the MESSENGER team has estimated the second-degree coefficients of the Hermean gravity field that combined with Earth-based radar measurements of Mercury's pole position, provide moment of inertia parameters of Mercury. Comparison of the internal structure models with the measured moment of inertia parameters indicates that the outer radius of the liquid portion of the core (constraining the mean radius, *2440 km*, and bulk density of Mercury, *5430 kg* m^{-3}) is *2030±37 km*, and the density of the outer shell overlying the liquid core is *3650±225 kg* m^{-3} (Smith et al., 2012).

1.1.2 Surface geology

A generalized geological history of Mercury has been developed from Mariner 10 images. The *45%* of Mercury's surface imaged by Mariner 10 can be divided into four

major terrains. Heavily cratered regions have an impact crater density suggesting that this terrain records the period of heavy bombardment that ended about *3.8* billion years ago on the Moon. Intercrater plains, the most extensive terrain type, were emplaced over a range of ages during the period of heavy bombardment. Hilly and lineated terrain occurs antipodal to the Caloris basin (large impact crater at *30°N* and *189°W*) at *1300 km* diameter the largest and youngest known impact structure on Mercury, is thought to have originated at the time of the Caloris impact by the focusing of impact-generated shock waves. Smooth plains, the youngest terrain type, cover *40%* of the area imaged by Mariner 10, are mostly associated with large impact basins, ad are in a stratigraphic position similar to that of the lunar maria. On the basis of the areal density of impact craters on the portion of Mercury's surface imaged by Mariner 10, as well as the scaling of cratering flux from the Moon to Mercury, smooth plains emplacement may have ended earlier on Mercury than did mare volcanism on the Moon (Neukum et al., 2001).

The role of volcanism in Mercury's geological history is uncertain. Both volcanism and impact ejecta emplacement mechanism have been suggested for the intercrater and smooth plains. Images obtained by MESSENGER established the presence and diversity of volcanism on Mercury early in the planet's history and indicated an association with ancient impact basins. MESSENGER's third Mercury flyby revealed a *290-kilometer*-diameter peak-ring impact basin, among the youngest basins yet seen, having an inner floor filled with spectrally distinct smooth plains. These plains are sparsely cratered; postdate the formation of the basin, apparently formed from material that once flowed across the surface, and are therefore interpreted to be volcanic in origin. An irregular depression surrounded by a halo of bright deposits northeast of the basin marks a candidate explosive volcanic vent larger than any previously identified on Mercury. Volcanism on the planet thus spanned a considerable duration, perhaps extending well into the second half of solar system history (Prockter et al., 2010).

Mercury's tectonic history is unlike that of any other terrestrial planet. The most prominent tectonic features on the surface are lobate scarps (Figure 1.2), *20-500 km* in length and hundreds of meters to several kilometers in height. On the basis of their asymmetric cross-sections, rounded crests, sinuous but generally linear to arcuate planforms, and the transection relationships with craters, the scarps are interpreted to be the surface expression of major thrust faults. Because the scarps are more or less evenly distributed over the well-imaged portion of the surface and display a broad range of azimuthal trends, they are thought to be the result of global contraction of the planet. From the lengths and heights of the scarps, and from simple geometric fault models or fault length-displacement relationships, the inferred *0.05-0.10%* average contractional strain if extrapolated to the full surface area of the planet would be equivalent to a decrease of *1-2 km* in planetary radius.

This estimate of global contraction poses a potentially strong constraint on models for cooling of Mercury's interior. Thermal history calculations that incorporate parameterized core and mantle convection as well as the generation and upward transport of mantle partial melt indicate that models consistent with *0.05-0.10%* surface contraction

since the end of heavy bombardment are limited to those with a mantle rheology appropriate to anhydrous conditions, modest concentrations of heat-producing elements, and a significant fraction of a light alloying element in the core to limit inner core solidification (Solomon, et al. 2007).

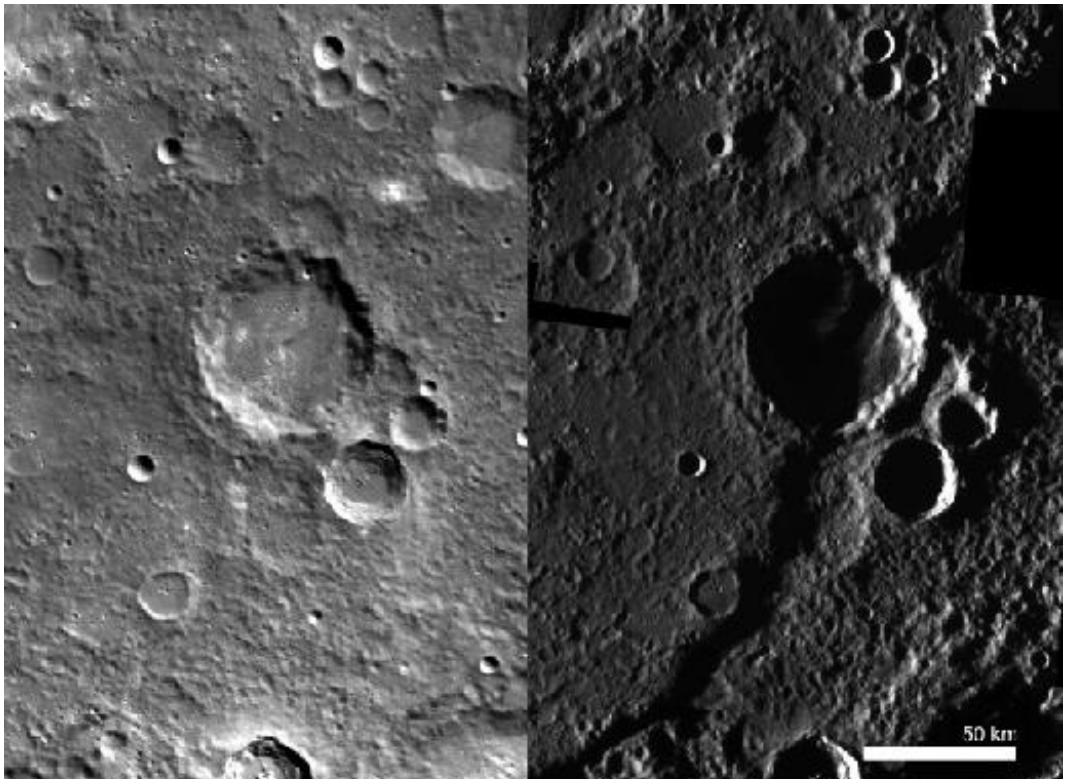

Figure 1.2 Discovery Rupes with different illumination conditions, incidence angle of 62° (left image) and 85.6° (right image)[1]

Global multicolor imaging of the surface with the missions MESSENGER and BepiColombo will provide a substantial improvement in our knowledge of the full geological history of Mercury. The side-by-side comparison of interesting features with high-resolution imaging under different illumination conditions is crucial to determine Mercury's geological history.

Both missions are also equipped with on board gamma ray and neutron spectrometer that attempt to map the entire surface in several different wavelengths, and to find water ice in polar craters, which are permanently in shadow from the Sun's rays. The discovery in 1991 of radar-bright regions near Mercury's poles and the similarity of the radar reflectivity and polarization characteristics of these regions to those of icy satellites and the south residual polar cap of Mars led to the proposal that these areas host deposits of

[1] http://www.nasa.gov/

surface or near-surface water ice. New evidence from MESSENGER is building support for the idea that the tiny planet may be harboring water ice in some of its most extreme terrain. The NASA probe has found that those same radar-bright spots appear to be in permanent shadow, according to camera views from the spacecraft's Mercury Dual Imaging System (MDIS).

1.1.3 Exosphere

Mercury's atmosphere is a surface-bounded exosphere whose composition and behavior are controlled by interactions with the magnetosphere and the surface (Domingue et al., 2007). The atmosphere is known to contain six elements (H, He, O, Na, K, Ca). The Mariner 10 airglow spectrometer detected H, He and O (Broadfoot et al., 1976), while ground-based spectroscopic observations led to the discovery of Na (Potter and Morgan, 1985), K (Potter and Morgan, 1986), and Ca (Bida et al., 2000). The exosphere is not stable on timescales comparable to the age of the planet, so there must be sources for each of the constituents. H and He are likely to be dominated by solar wind ions neutralized by recombination at the surface, but the other species are likely derived from impact vaporization of micrometeoroids hitting Mercury's surface or directly from Mercury surface materials (Domingue et al., 2007).

Proposed source processes for supplying exospheric species from Mercury's crust include diffusion from the interior, evaporation, sputtering by photons and energetic ions, chemical sputtering by protons, and meteoritic infall and vaporization (Killen et al., 1999). That several of these processes play some role is suggested by the strong variations in exospheric characteristics observed as functions of local time, solar distance, and level of solar activity as well as by correlations between atmospheric Na and K enhancements and surface features (Sprague et al., 1998).

The presence of the volatile elements Na and K in Mercury's exosphere poses a potential challenge for the hypothesis advanced to account for Mercury's high ratio of metal to silicate. Whether Mercury is metal-rich because of mechanical segregation between metal and silicate grains in the hot, inner solar nebula or because of extensive volatilization or impact removal of the outer portions of a differentiated planet, the planetary crustal concentrations of volatile elements should be very low. For several of the proposed sources of exospheric Na and K, crustal abundances ranging from a few tenths of a percent by weight are commonly required (Killen et al., 2001).

Spacecraft in orbit about Mercury provide a range of opportunities for elucidating further the nature of the exosphere. Limb scans conducted with an ultraviolet-visible spectrometer can monitor variations in the major exospheric constituents and search for new species. MESSENGER and BepiColombo are therefore equipped with γ-ray, X-ray, and neutron spectrometer. The first results have been obtained in 2008 with the MESSENGER probe's Fast Imaging Plasma Spectrometer (FIPS) that discovered several molecular and different ions in the vicinity of Mercury, including H_2O^+ (hydroxonium),

OH (hydroxyl), O_2^+ and Si^+ are present as well (Zurbuchen et al., 2008). During its 2009 flyby, the Ultraviolet and Visible Spectrometer (UVVS) channel of the Mercury Atmospheric and Surface Composition Spectrometer (MASCS) on board the MESSENGER spacecraft first revealed the presence of magnesium in the Hermean exosphere. The near-surface abundance of this newly detected constituent is roughly comparable to that of sodium (McClintock et al., 2009).

1.1.4 Magnetic field and magnetosphere

Mercury's intrinsic magnetic field, discovered by Mariner 10 (Ness et al., 1976), is about 1.1% as strong as Earth's (Coffey, 2011). At the Hermean equator, the relative strength of the magnetic field is around *300 nT* (Kabin et al., 2008). Although much weaker than Earth's magnetic field (about 1/100 its magnitude) according to Mariner 10 data, the magnetic field is still strong enough to deflect solar wind emissions, inducing a magnetosphere (Figure 1.3). Mercury's magnetic field being weaker than Earth's may be because its core had cooled and solidified more quickly than the Earth.

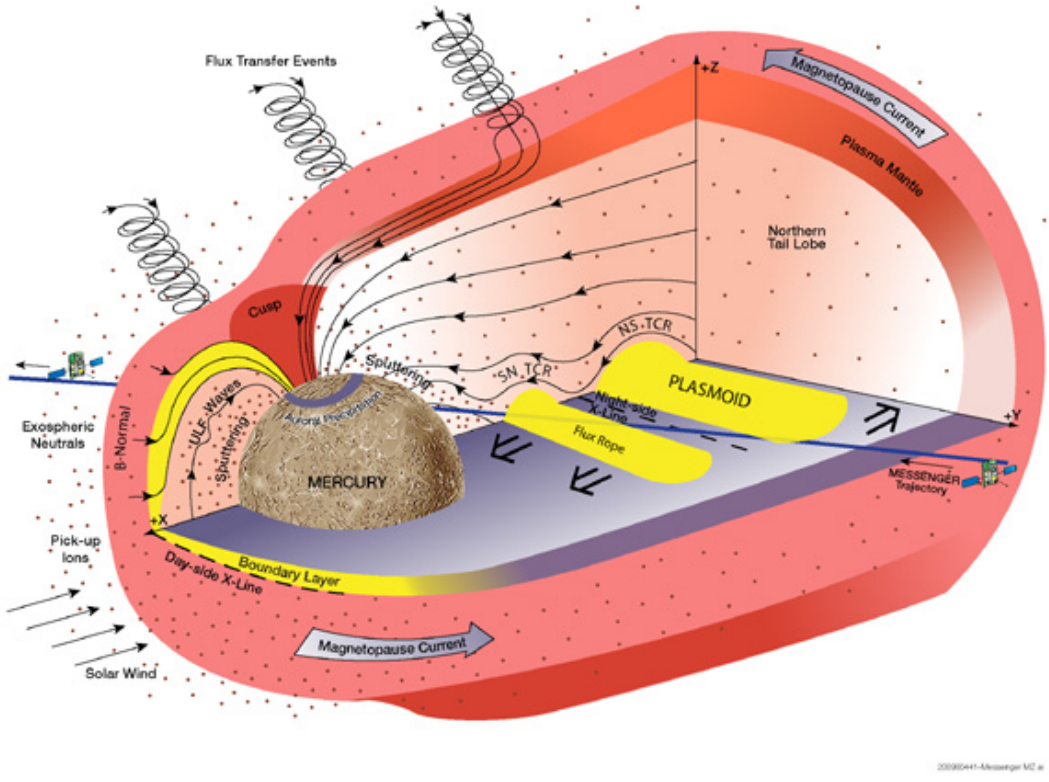

Figure 1.3 Mercury's magnetic field[2]

[2] http://www.universetoday.com/35873/mercury-magnetic-field/

Whether the magnetic field changed to any significant degree between the Mariner 10 mission and the MESSENGER mission remains an open issue. A 1988 Connerney and Ness review of the Mariner 10 magnetic data noted eight different papers in which were offered no less than fifteen different mathematical models of the magnetic field derived from spherical harmonic analysis of the two close Mariner 10 flybys, with reported centerered magnetic dipole moments ranging from *136* to *350 nT-R_M^3* (R_M=*2436 km* is Mercury's mean radius).

The origin of this field, however, is not fully understood (Stevenson, 2003). Mercury's magnetic field cannot be externally induced because the measured planetary field is far greater in magnitude than the interplanetary field (Connerney and Ness, 1988). The dipole field could be a remanent or fossil field acquired during lithospheric cooling in the presence of an internal or external field, or it could be the product of a modern core dynamo (Stevenson, 2003). Permanent magnetization from an external source has been discounted on the grounds that a thick shell of coherently magnetized material is needed to match the observed dipole moment, and the lithosphere of Mercury would not have been able to cool and thicken sufficiently in the time interval during which strong solar or nebular fields were present (Schubert et al., 1988). Permanent magnetization from an internal source has been questioned on the grounds that a high specific magnetization of the shell and a characteristic interval between field reversals much longer than on Earth are both required (Schubert et al., 1988).

The hypothesis that Mercury's internal field is remanent is receiving renewed attention after the discovery of strongly magnetized regions in the crust of Mars (Acuna et al., 1999). Mars may not be a good analogue to Mercury in all respects, because the potential magnetic carriers on Mars are iron-rich oxides and Mercury's crust appears to be very low in Fe^{2+}. The possibility remains, however, that Mercury's crust may not contain sufficient metallic iron or iron sulfides to display magnetic thermoremanence and crustal fields detectable from orbit (Solomon et al., 2007).

A new look at the idea that crustal remanence may give rise to the dipolar field has come from a consideration of the strong variation of solar heating with latitude and longitude on Mercury (Aharonson et al., 2004). Because Mercury's obliquity (the angle that the spin axis makes with the normal to the planet's orbital plane) is small, equatorial regions are heated by the Sun to a greater degree than polar regions. Further, Mercury's eccentric orbit and 3:2 spin-orbit resonance result in two equatorial 'hot poles' that view the Sun at zenith when Mercury is at perihelion (and two equatorial 'cold poles' midway between them). Despite a theorem that a uniform spherical shell magnetized by an internal field displays no external field after the internal field has been removed, a result that is not strictly correct when the magnetizing effect of the crustal field is included, the thickness of Mercury's crust that is below the Curie temperature of a given magnetic carrier varies spatially (Aharonson et al., 2004). As a result, there is strong dipolar contribution to the external field that would be produced by a crust magnetized by a past internal field, the predicted dipole moment (Aharonson et al., 2004) is within the range of

estimates for Mercury (Connerney and Ness, 1988), and the predicted ratio of quadrupole to dipole terms (Aharonson et al., 2004) is testable with spacecraft measurement.

The origins of the magnetic field can be also explained by dynamo theory. A dynamo is generated by a large iron core that has sank to a planet's center of mass, has not cooled over the years, an outer core that has not been completely solidified, and circulates around the interior. Before its discovery in 1974, it was thought that Mercury's core had cooled over the years of evolution of the solar system, regarding the planet's small size. A hydromagnetic dynamo in a liquid, metallic outer core requires both that a substantial fraction of Mercury's core is presently fluid and that there are sufficient sustained sources of heat or chemical buoyancy within the core to drive the convective motions needed to maintain a dynamo. Because it is not known that either requirement is met in Mercury, more exotic dynamo models have been considered. If the fluid outer core is sufficiently thin and the core-mantle boundary is distorted by mantle convective patterns, thermoelectric currents might be driven by temperature differences at the top of the core. A thermoelectric dynamo is likely to produce a field richer in shorter-wavelength harmonics than an Earth-like dynamo, and these harmonics may correlate with those for the gravity field, so distinguishing among dynamo models should be possible from orbital measurements.

Recent magnetometer data acquired by the MESSENGER spacecraft in orbit about Mercury permit the separation of internal and external magnetic field contributions. The global planetary field is represented as a southward-directed, spin-aligned, offset dipole centered on the spin axis. Positions where the cylindrical radial magnetic field component vanishes were used to map the magnetic equator and reveal an offset of 484 ± 11 km northward of the geographic equator (Anderson et al., 2011). The magnetic axis is tilted by less than 3° from the rotation axis. Anderson *et al.* (2011), using high-quality MESSENGER data from many orbits around Mercury found that the dipole moment is $195 \pm 10\ nT\text{-}R_M^3$.

1.2 Research with space probes

The exploration of Mercury has taken only a minor role in the space interests of the world. Earth-based astronomical observations must contend with the fact that Mercury is never far from the Sun in the sky. Mercury is a forbidden target of the Hubble Space Telescope and presumably of other space imaging systems for which direct observations near the Sun must be avoided. Mercury poses severe thermal and dynamical challenges to observation by spacecraft, and to date the planet has been visited only by Mariner 10, which flew by Mercury three times in 1974-1975. Immediately following the Mariner 10 mission, a Mercury orbiter was widely recognized as the obvious next step in the exploration of the planet. Further, the primary complex objectives of such an orbiter mission were defined: " to determine the chemical composition of the planet's surface on both a global and regional scale, to determine the structure and state of the planet's

interior, and to extend the coverage and improve the resolution of orbital imaging (COMPLEX, 1978). In the late 1970s, however, it was thought that the change in spacecraft velocity required for orbit insertion around Mercury was too large for conventional propulsion systems, and this belief colored the priority placed on further exploration of the innermost planet (COMPLEX, 1978).

In the mid-1980s, about a decade after the end of the Mariner 10 mission, multiple gravity-assist trajectories were discovered that could achieve Mercury orbit insertion with chemical propulsion systems. This finding stimulated detailed studies of Mercury orbiter missions in Europe and the United States between the mid-1980s and early 1990s. During the same time interval there were important discoveries made by ground-based astronomy, including the Na and K components of Mercury's atmosphere (Potter and Morgan, 1985) and the radar-reflective deposits at Mercury's north and south poles (Harmon and Slade, 1992). A re-examination of the primary objectives of a Mercury orbiter mission during that period affirmed those defined earlier and added "that characterization of the Mercury's magnetic field be [an additional] primary objective for exploration of that planet" (COMPLEX, 1990).

In the early 1990s, after re-examining its approach to planetary exploration, NASA initiated the Discovery Program, intended to foster more frequent launches of less costly, more focused missions selected on the basis of rigorous scientific and technical competition. Mercury was the target of a number of early unsuccessful proposals to the Discovery Program for flyby and orbiter missions. The MESSENGER concept was initially proposed to the NASA Discovery Program in 1996, and after multiple rounds of evaluation the mission was selected for flight in July 1999.

In parallel with the selection, development and launch of MESSENGER, the European Space Agency (ESA) and the Institute of Space and Astronautical Science (ISAS) of the Japan Aerospace Exploration Agency (JAXA) have approved and are currently developing the BepiColombo mission to send two separate spacecraft into Mercury orbit. BepiColombo was selected by ESA as its fifth cornerstone mission in the Science Programme's long term plan, Horizons 2000, and ISAS announced its intent to collaborate on the project that same year. The two spacecraft, scheduled for launch on Ariane 5 in July 2015, will be coplanar polar orbits. An ESA-supplied Mercury Planetary Orbiter (MPO) will emphasize observations of the planet, and an ISAS-supplied Mercury Magnetospheric Orbiter (MMO) will emphasize observations of the magnetosphere and its interactions with the solar wind. Payload instruments on the two spacecraft were selected in 2004 (Hayakawa et al., 2004; Schulz and Benkhoff, 2006).

1.2.1 Mariner 10

Mariner 10 was the seventh successful launch in the Mariner series and the first spacecraft to visit Mercury. It was also the first spacecraft to use the gravitational pull of one planet (Venus) to reach another (Mercury), and the first spacecraft mission to visit

two planets. The spacecraft flew by Mercury three times in a retrograde heliocentric orbit and returned images and data on the planet. Mariner 10 returned the first-ever close-up images of Venus and Mercury. The primary scientific objectives of the mission were to measure Mercury's environment, atmosphere, surface, and body characteristics and to make similar investigations of Venus. Secondary objectives were to perform experiments in the interplanetary medium and to obtain experience with a dual-planet gravity-assist mission.

The spacecraft structure was an eight-sided forger magnesium framework with eight electronics compartments (Figure 1.4). It measured *1.39 m* diagonally and *0.457 m* in depth. Two solar panels, each *2.69 m* long and *0.97 m* wide, were attached at the top, supporting *5.1* m^2 of solar cell area. Fully deployed the spacecraft measured *8.0 m* across the solar panels and *3.7 m* from the top of the low-gain antenna to the bottom of the heat shield. A scan platform with two degrees of freedom was mounted on the anti-sunward face. A *5.8 m* long hinged magnetometer boom extended from one of the octagonal sides of the body.

Figure 1.4 Mariner 10 probe[3]

Mariner 10 carried a motor driven high-gain dish antenna, a *1.37 m* diameter aluminum honeycomb-disk parabolic reflector, which was mounted on a boom on the side of the spacecraft. A low-gain omnidirectional antenna was mounted at the end of a *2.85 m* boom extending from the anti-solar face of the spacecraft. Feeds enabled the spacecraft to transmit at S- and X-band frequencies; data could be transmitted at a maximum rate of *117.6 kilobits per second*.

[3] http://www.nasa.gov/

Instruments on-board the spacecraft measured the atmospheric, surface, and physical characteristics of Mercury and Venus. Experiments included television photography, magnetic field, plasma, infrared radiometry, ultraviolet spectroscopy, and radio science detectors. An experimental X-band, high-frequency transmitter was flown for the first time on this spacecraft.

Mariner 10 (also known as Mariner Venus Mercury 1973) was placed in a parking orbit after launch for approximately *25 minutes*, and then placed in orbit around the Sun en route to Venus. The protective cover of the sunward-facing electrostatic analyzers did not open fully after launch, and these instruments, part of the Scanning Electrostatic Analyzer and Electron Spectrometer experiment, could not be used. It was also discovered that the heaters for the television cameras had failed, so the cameras were left on to prevent low temperatures from damaging the optics.

In January 1974 Mariner 10 made ultraviolet observations of Comet Kohoutek and another mid-course correction was made on 21 January. The spacecraft passed Venus on February 5, 1974, at a closest range of *5768 km* at 17:01 UT and returned the first close-up images of Venus. This also marked the first time a spacecraft used a gravity assist from one planet to help it reach another.

En route to Mercury an attitude control anomaly occurred for the second time, using up attitude control gas. Some new procedures were used from that point on to orient the spacecraft, including Sun-line maneuvers and the use of solar wind on the solar panels to orient the spacecraft. Mariner 10 crossed the orbit of Mercury on March 29, 1974, at 20:46 UT, at a distance of about *704 km* from the surface. A second encounter with Mercury, when more photographs were taken, occurred on September 21, 1974, at an altitude of *48 069 km*. Unfortunately the lighted hemisphere was almost the same as the first encounter, so a large portion of the planet remained unimaged. A third and last Mercury encounter at an altitude of *327 km*, with additional photography of about *300* frames and magnetic field measurements occurred on March 16, 1975. Engineering tests were continued until March 24, 1975, when the supply of attitude-control gas was depleted and the mission was terminated.

Mariner 10 three flybys about Mercury allowed mapping *40-45%* of Mercury's surface. Taking *2800* photos, Mariner 10 revealed a crater, dormant Moon-like surface. It thus contributed enormously to our understanding of the planet, whose surface had not been successfully resolved through telescopic observation. The regions mapped included most or all of the Shakespeare, Beethoven, Kuiper, Michelangelo, Tolstoj, and Discovery quadrangles, half of Bach and Victoria, and small portions of Solitudo Persephones, Liguria, and Borealis. Furthermore, Mariner 10 also discovered that Mercury has a tenuous atmosphere consisting primarily of helium, as well as a magnetic field and a large iron-rich core. Its radiometer readings suggested that Mercury has a nighttime temperature of *-183°C* and maximum daytime temperatures of *187°C*. The gravity analysis of radio Doppler and range data during two of its encounters with Mercury has resulted in a determination of two second degree gravity harmonics, $J_2 = (6.0 \pm 2.0) \times 10^{-5}$

and $C_{22} = (1.0 \pm 0.5)\times10^{-5}$, referred to an equipotential surface of *2439 km* (Anderson et al., 1987).

1.2.2 Synergy of MESSENGER and BepiColombo

The advances in spacecraft technology and a growing realization of how important Mercury is to our understanding of the solar system and its formation led to the development of two missions for more intensive Mercury exploration. The MErcury Surface, Space ENvironment, GEochemestry, and Ranging (MESSENGER) mission, selected under the NASA Discovery Program, launched a spacecraft on August 3, 2004, which has been orbiting about Mercury for two years. The mission, spacecraft, and payload were designed to answer crucial issues pointed out by Mariner 10 regarding the innermost planet. The mission has focused to date on commissioning the spacecraft and science payload as well as planning for flyby and orbital operations. MESSENGER completed three Mercury flybys in January and October 2008 and September 2009. Those flybys provided opportunities to image the hemisphere of the planet not seen by Mariner 10, obtain high-resolution spectral observations with which to map surface mineralogy and assay the exosphere, and carry out an exploration of the magnetic field and energetic particle distributions in the near-Mercury environment. The orbital phase, begun on March 11, 2011, is near-polar-orbital observational campaign that addresses all mission goals. These two years have been focused on complete global imaging of the planet, detailed surface compositional and topographic data over the northern hemisphere, geometry of Mercury's internal magnetic field and magnetosphere, radius and physical state of Mercury's outer core, the nature of Mercury's polar deposits, and exospheric neutrals and magnetospheric charged particle species over a range of dynamic conditions. MESSENGER is definitely expanding our understanding of the formation and evolution of the innermost planet providing interesting data about Mercury's chemical composition, geology and magnetic field.

The second mission is the more comprehensive BepiColombo to explore the planet Mercury through a partnership between ESA and JAXA. Two spacecraft, the Mercury Planetary Orbiter (MPO) and the Mercury Magnetospheric Orbiter (MMO), will study the planet and its environment from two different orbits. Both orbiters will be launched together on Ariane 5 in July 2015 with arrival in January 2022. The MMO provided by JAXA focuses on investigating the wave and particle environment of the planet from an eccentric orbit. The MPO a three-axis-stabilized and nadir-pointing spacecraft in a low-eccentricity polar orbit is dedicated to the characterization of Mercury. It will provide high accuracy measurements of the planet's interior structure, a thoroughly investigation of Mercury's exosphere, and a full coverage of the planet surface at high resolution, whereby surface morphology will be correlated to surface composition. Major effort was input into optimizing the scientific return by defining complement such that individual measurements can be interrelated and complement each other. With its two-spacecraft,

interdisciplinary approach, the BepiColombo mission will provide the detailed information necessary to understand the process of planetary formation and evolution in the hottest part of the proto-planetary nebula, as well as the similarities and differences between the magnetospheres of Mercury and Earth. In addition, the mission offers unique possibilities for testing Einstein's theory of general relativity.

The cooperation between the missions MESSENGER and BepiColombo began in an initial meeting that was held among the principals of the projects in September 1999, shortly after NASA's selection of MESSENGER for development. A joint memorandum of cooperation was signed, highlighting explicitly the mutual desire for cooperation between the two projects to ensure the maximum return of knowledge from Mercury during this new era of Mercury exploration. Additional discussions have been at the European Geophysical Union (EGU) in May 2000, the EGS General Assemblies in 2001 and 2002, and the World Space Congress in 2002. Such regular contacts have ensured open communication between the two projects holding periodically joint workshops.

There are common scientific questions that define the objectives of the two missions at Mercury. All of the significant scientific topics identified since the Mariner 10 mission are covered, hence it is not surprising that the objectives of the two missions are similar.

MESSENGER arrived in Mercury orbit prior to the BepiColombo spacecraft and, therefore, can be used as a pathfinder for detailed BepiColombo observations. In particular, MESSENGER observations can target high-resolution measurements by BepiColombo. In addition, MPO and MMO observations will provide complementary phase angles for viewing geological landforms, an aid to removing ambiguities for interpretation. Additional observations (and the better downlink capabilities) will allow BepiColombo to extend altimetric coverage and radio occultation observations while also extending the temporal baseline for gravitational physics measurements. Finally, the cooperative use of ground stations will provide opportunities for downlinking data that would not otherwise be present.

Opportunities for cooperation in the magnetosphere include a baseline of observations of how Mercury's magnetosphere evolves over a solar cycle, something made possible by the different arrival times of the spacecraft. Simultaneous measurements by MESSENGER and BepiColombo are highly desirable, but the nominal MESSENGER orbital extended mission ends in April 2013. Spatially, Mercury magnetospheric coverage by MESSENGER focuses on polar measurements while MMO coverage, coordinated with MPO, explicitly targets Mercury's magnetosheric structure and variations.

Given the commonality and overlap of broad objectives, it is not surprising that the general functionality of some of the nominal BepiColombo payload should be similar to that of MESSENGER. However, the extent of commonality of performance depends upon the detailed requirements. At the same time, with the broader scope of the BepiColombo mission, there are also many nominal instruments that may permit measurements that are not made by MESSENGER. For dealing with tasks such as measurement of the changing magnetic field and viewing the same geological formations

from different phase angles, commonality of function at some level is desirable to maximize the total scientific return made possible by combining the two full datasets.

In conclusion, the selection of MESSENGER by NASA and BepiColombo by ESA and ISAS to explore Mercury offers a unique opportunity. Even though the two missions are not formally joined programmatically, each brings unique capabilities to a long overdue, detailed exploration of the innermost planet. By pursuing international cooperation, both team have established lines of communication that will ensure that the maximum amount of new knowledge will be returned to the international scientific community and that the total knowledge returned will be greater than the sum of the two parts (McNutt Jr. et al., 2004).

Chapter 2

Orbit determination for the geodesy of Mercury

Outline. Most of the present knowledge on the planetary gravity fields and interiors has been derived from accurate spacecraft tracking and precise orbit determination. Interplanetary tracking systems rely on microwave links for obtaining the key navigational data, namely the frequency and propagation time of radio signals. These observables quantities are input to complex orbit determination codes, where the observed quantities are compared with their predicted values to produce an estimate of the spacecraft state and other parameters of the model. The missions MESSENGER and BepiColombo aim to estimate the Mercury's gravity field with a precise orbit determination of the spacecraft. The complexity of the mission scenarios suggests the adoption of an estimation process able to reduce the risk of parameter aliasing from mismodeled non-conservative forces. To this end, we have adopted a batch-sequential estimation scheme. This estimator is tailored to provide a reconstruction of the spacecraft orbit and the gravity field of Mercury with increasing fidelity, as additional data are received.

2.1 Radio science experiments

The radio science experiments on board interplanetary missions make a virtue out of a necessity by using the radio signals that convey data and instructions between the spacecraft and Earth to probe surfaces and interior structures of planets and satellites of the solar system. Beyond planetary science, the tools and techniques of Radio Science (RS) on planetary missions are applied to investigations of the solar wind, corona and magnetic field, as well as tests of fundamental physics including the theory of General Relativity. RS techniques are also highly important in monitoring mission critical maneuvers or spacecraft emergencies under conditions of low signal level and/or high signal dynamics.

The broad sense of radio science is the use of propagating electromagnetic waves to explore the universe. RS observations can be passive, as in observations of naturally occurring emissions, or active, as in the results of probing with artificial signals. In planetary exploration, the term radio science has been commonly used for about four decades to describe the scientific utilization of radio signals from spacecraft as opposed to natural celestial radio emissions. This field is distinguished from other sciences by its definition in terms of methods rather than by objects of study.

The current investigations include microwave radio occultations by planetary rings, ionosphere, and neutral atmosphere, propagation through the solar corona, reflection from surfaces, and distance/velocity measurements leading to determinations of mass and density distribution and construction of models for gravity fields and interior structure. The investigations can be grouped into two classes: *propagation* and *gravitation*, where the first investigates the effects of media on the signals and treats the effects of spacecraft motion as noise to be calibrated out of the data, and the second investigates the effects of forces on the spacecraft causing shifts in the signal and treats the effects of media as noise to be calibrated out of the data (Asmar et al., 2009).

Radio science often benefits from collaborative fields such as the interactions between waves and charged particles, radar surface imaging, planetary topography, accelerometry, spacecraft navigation, VLBI (Very Long Baseline Interferometry) precision measurements of angular motion, and relativistic gravity. The discipline came of age in 1964 when the National Bureau of Standards renamed Section D of its *Journal of Research* to *Radio Science*; the journal has been published by the American Geophysical Union since 1969. RS data are preserved for future generations within the Planetary Data System since the measurements are self-calibrating and never outdated; as long as quality instrumentation is operated properly, measurements made today can be included in future analyses for very long periods of time.

2.1.1 Radio tracking data

The fundamental RS observations parameters are amplitude, frequency, phase, time, polarization, and direction of propagation of the wave. Measurement accuracy depends on the phase and amplitude stability of the equipment and signal-to-noise ratio. Extraction of the highest quality science requires calibration of the intervening medium and non-gravitational forces as well as accurate reconstruction of position, attitude, and motion of the transmitter, receiver, and target. Precision time/frequency standards are essential; when possible, multiple links, water vapor radiometers, accelerometers and noise power standards lead to accurate calibration of the data observables.

Prior to the Voyager mission, RS experiments were conducted using the spacecraft and ground telecommunications and tracking without modification to enhance the science. Voyager was the first deep space mission to be equipped with an Ultra Stable Oscillator (USO), added to provide a higher quality “clock” for atmospheric and ring occultations. Voyager was also the first mission to employ two coherently related

wavelengths simultaneously, S- and X-bands, which improved the ionospheric occultations and enabled calibration of dispersive noise sources. Galileo was upgraded with elliptically polarized transmission to investigate Faraday rotation but the payoff was not realized due to the deployment failure of the high gain antenna. Mars Global Surveyor used the next generation USO, more stable by an order of magnitude than the USO of Voyager; Cassini, New Horizons, GRACE, GRAIL, MESSENGER and other missions later used this class of USO. European deep space missions such us Ulysses, Rosetta, Mars Express, and Venus Express also had the capability for simultaneous S- and X-band links. Rosetta and Venus Express carry also USOs.

The on-board radio frequency subsystem (RFS) is an essential element for implementing high accuracy range and range rate measurements. Usually the RFS is made up by a transponder, which receives a single frequency signal and coherently retransmits it to ground. This simple implementation is not adequate for high precision experiments, where plasma noise is a limiting factor. Cassini is the first deep space mission supporting multi-frequency radio links for plasma noise calibration, due to a suitable configuration of the onboard RFS, made up by a deep space transponder (DST) and a Ka-band frequency transponder (KaT). The KaT is simply a coherent frequency translator, dedicated to radio science experiments. Other functions (such as ranging, telecommand and telemetry) are not implemented. This RFS architecture allows simultaneous measurements from three coherent frequency links, namely X(up)/X(down), X(up)/(Ka(down), Ka(up)/Ka(down). Lacking a ranging channel for both Ka-band signals, plasma calibration is possible for Doppler measurements only. The ranging measurements are affected by the plasma error contribution, because the ranging tone modulates only the X/X link. The mission BepiColombo, because of the stringent scientific goals, requires upgraded performances on the ranging function (a factor 10 better than for typical deep space missions) entailing a complete plasma calibration on the ranging observables. This implies that the ranging turn-around function is implemented on all three-frequency links (X/X, X/Ka and Ka/Ka).

The technological advances in flight instrumentation have joined with the technological development in ground instrumentation. Ka-band uplink capabilities have been installed at one Deep Space Network (DSN) station, designated Deep Space Station (DSS) 25 at Goldstone (California, USA), specifically to support RS experiments; Ka-band downlink capabilities exist at all NASA complexes. At the same time, the European Space Agency has been assessing to provide Ka-band uplink capabilities at one ESA station with a view to the mission BepiColombo. This RS upgrade included advanced systems for pointing at Ka-band and media calibration especially of the Earth troposphere with advanced water-vapor radiometers. Additional infrastructure improvements throughout the DSN, such as improved frequency and timing, general media calibrations antenna pointing, antenna vibration reduction, and microwave amplitude and phase stability, also benefit RS. A key component for DSN observations is the Radio Science Receiver, which was developed (in predecessor design) to preserve the characteristics of the enhanced downlink signals from Voyager. It is a specially designed ultra-stable multi-

channel open-loop receiver independent of the tracking receivers, comprised of a dedicated full-spectrum processor tuned by a prediction file. The current digital generation receives a down-converted signal in a pre-selected bandwidth appropriate to the specific RS experiment. The multi-mission Radio Science Receiver is operated remotely from the Jet Propulsion Laboratory (JPL) by science teams and their staff for optimal configuration, reaction to fast changes (requires high-speed data return) increase the scope of RS activities and allow for improved feedback when needed and low operational cost.

The advanced in flight and ground instrumentations provide therefore high accurate radio tracking observables: range rate, range and Differential One Way Ranging (Δ-DOR), which lead to precise orbit determination of spacecraft in deep space missions.

2.1.1.1 Range rate

Range rate observables are provided through measurement of the received carrier integrated phase shift. The relative velocity of the spacecraft in the line-of-sight gives rise to a frequency shift in the received carrier. When the signal transmitted by the spacecraft is derived from an on-board oscillator (e.g. an ultra stable oscillator), the measurement is said to be "one-way". If the spacecraft transponds a signal transmitted from the ground and the ground-based reference for the Doppler is the same one that drives the transmitter, the observation is "two-way". The measurement is "three-way" if the ground station receives a signal transponded by the spacecraft but the uplink is from a different ground station. These distinctions are relevant because, depending on the Doppler mode, both signals and noises have different transfer functions connecting them to the observation.

If the loop Ground Station (GS) – Spacecraft (SC) - Ground Station is non-coherent the frequency shift can provide an estimate of velocity with an accuracy that is dependent on the stability of the reference frequency sources. If the GS-SC-GS is coherent then the integrated phase observation provides a very accurate measurement of the change in range over the observational interval (delta-range). This parameter is a key input to the orbit determination process since it can be used, with knowledge of the ground station motion, to determine a direction component. A key determinant of the performance of an integrated Doppler system is the phase stability of the GS-SC-GS loop. Range rate observables can be obtained from 1-way, 2-way or 3-way links but normal deep-space operation in the current NASA and ESA is 2-way coherent.

In the coherent configuration the downlink carrier frequency is determined by a coherent turnaround of the transponder. The two-way coherent Doppler is given by:

$$f_{dr}(t_3) = f_{ut}(t_1)\sqrt{\frac{1-v(t_2)/c}{1+v(t_2)/c}}\frac{N}{M}\sqrt{\frac{1-v(t_2)/c}{1+v(t_2)/c}} = f_{dt}(t_1)\frac{N}{M}\frac{c-v(t_2)}{c-v(t_2)} \qquad (2.1)$$

where f_{ut} is the uplink frequency (which may be constant or pre-steered), f_{dr} is the downlink frequency, t_1 is the time of ground transmission, t_2 is the time of turnaround at the spacecraft, t_3 is the time of ground reception and v is the radial velocity of the spacecraft relative to the ground station at the turnaround time (positive away). The transponder turnaround ratio is (N/M).

The ground station records the uplink and downlink unwrapped carrier phase and uses these measurements, along with the two-way Expected Propagation Delay ($EPD= t_3 - t_1$) to form an Integrated Doppler (ID) phase measurement (measured in phase turns):

$$\begin{aligned} ID(T) &= \int_0^T f_{dr}(t)\,dt - \frac{N}{M}\int_0^T f_{ut}(t - EPD)\,dt = \\ &= -\frac{N}{M}\int_0^T f_{ut}(t - EPD)\frac{2v(t_2)}{c + v(t_2)}dt \end{aligned} \tag{2.2}$$

If the uplink frequency is constant and the radial velocity is much smaller than c (speed of light) the integrated Doppler directly translates to one-way delta-range over the period T:

$$\frac{ID(T)}{f_{ut}}\frac{M}{N}\frac{c}{2} = -\int_0^T v(t)dt \tag{2.3}$$

The accuracy of this measurement is dependent on the phase stability of the ground station up and downlinks paths, the phase stability of the transponder path and the frequency stability of the ground station reference between t_1 and t_3. Since integrated Doppler is a relative measurement the absolute ground station delay is not important however the phase stability of the ground station electronics for the duration of the pass is important.

In non-coherent configuration the oscillator on board the spacecraft determines the downlink carrier frequency:

$$f_{dr}(t_2) = f_{dt}(t_1)\sqrt{\frac{1 - v(t_1)/c}{1 + v(t_1)/c}} \tag{2.4}$$

where f_{dt} is the spacecraft downlink frequency, t_1 is the time of spacecraft transmission, t_2 is the time of ground reception and v is the radial velocity of the spacecraft relative to the ground station at the turnaround time (positive away). Non-coherent Doppler can be treated in the same way as coherent Doppler except that there is now an uncertainty in the actual transmitted downlink frequency. Even in the case of a very high quality onboard USO the non-coherent Doppler quality is several order of magnitude worse than the coherent Doppler.

The principal disturbances in a Doppler link are due to instrumental noise (random errors introduced by ground or spacecraft themselves), propagation noise (random frequency/phase fluctuations caused by refractive index fluctuations along the line of sight), or systematic errors. Instrumental noises include phase fluctuations associated with finite signal-to-noise ratio (SNR) on the radio links, ground and spacecraft electronics noise, un-modeled bulk of motion of the spacecraft or ground station, frequency standard noise (ground standards and, in one-way observations, the spacecraft oscillator to which the downlink is referenced), and antenna mechanical noise (un-modeled phase variation within the ground station). Propagation noise is caused by phase scintillation as the radio wave passes through the troposphere, ionosphere, and solar wind. Instrumental and propagation noises display varying degrees of non-stationarity.

Geodesy and fundamental physics measurements at Mercury require very accurate orbit determination. The estimation of the relevant physics quantities, as the gravity field, is based especially on precise Doppler observables determined from microwave links between earth and spacecraft. Because of the orbit of Mercury, the principal disturbance of the range rate observations is due to plasma scintillation as the radio wave passes close to the Sun. The NASA mission MESSENGER, equipped with the Deep Space Transponder that allows the two-way coherent link in X-band, have necessary made the range rate observations for the radio science experiment at high Sun-Probe-Earth (SPE) angles. The plasma noise not only renders unusable the data at small SPE angles but also increases the noise standard deviation at about *0.1 mm/s* with a count time of *30 s*. This reduced performance of the radio science experiment limits considerably the scientific goals of the mission. For this reason, the future mission BepiColombo foresees a multi-link plasma cancellation system (e.g., like Cassini's) that could calibrate plasma noise to Allan deviations of about 10^{-14} (Asmar et al., 2005), even very close to the Sun. Therefore the expected Doppler data accuracy is about *1.5 μm/s* (at 1000 s of integration time).

2.1.1.2 Range

Range measurements are typically used to improve the trajectory models of spacecraft tracked by the Deep Space Network. When a spacecraft is in flight, the observables from range measurements are compared with values computed from a model of the trajectory, and discrepancies (called "residuals") are used to improve the model.

Within the DSN, the most common type of range measurement is produced by means of two-way coherent ranging. A DSS transmits an uplink carrier whose phase is modulated by a ranging signal. Within the spacecraft transponder, the uplink carrier is demodulated and the recovered ranging signal then phase-modulates the downlink carrier. The DSS receives and demodulates the downlink carrier and measures the round-trip delay of the ranging signal. This technique is coherent because the transponder uses a phase-locked technique to ensure that the uplink and downlink carriers are coherently related.

It is worthwhile considering why the round-trip delay, as opposed to a one-way delay, is measured. If the absolute delay of the downlink signal is measured without having a coherent uplink (or the uplink delay measured without a coherent downlink), the lack of synchronization between the spacecraft and the ground clocks translates directly into an error in the measured delay. The spacecraft clock is the biggest contributor to this error. With a round-trip (two-way) measurement, one clock marks the departure of the ranging signal and its return, and there is no clock synchronization issue.

One-way delay differences are measured with excellent accuracy in a technique called differential one-way ranging (Δ-DOR) described in *Section 2.1.1.3*. Three-way coherent ranging is similar to two-way coherent ranging. One DSS transmits the uplink carrier and a second DSS receives the downlink carrier. The delay measured in this way is not simply related to range, since the ranging signal does not execute a round trip. Nevertheless, the observables of three-way ranging can be compared with values computed from a trajectory model, providing feedback for the model. Three-way delay data are less accurate than two-way delay data. This is a consequence of clock offsets between the two DSSs as well as an inability to accurately calibrate three-way delay. Three-way ranging is useful when the round-trip delay is large.

The most accurate range measurements are made under the condition that the uplink and downlink carriers are coherently related. Uplinks in the band *2110-2120 MHz* (S-band) and the band *7145-7190 MHz* (X-band) are used in the DSN (BepiColombo requires also the Ka-band). The spacecraft transponder generates a downlink carrier frequency equal to the uplink carrier frequency multiplied by a rational number, the transponding ratio. The downlink is in the band *2290-2300 MHz* (S-band), *8400-8450* MHz (X-band) or *31800- 32300 MHz* (Ka-band).

The range measurement in deep space applications is based on a sequential procedure, both for ESA and NASA tracking system. Two different kinds of ranging signal are considered: sinusoidal tones and codes (square-wave combination). During the measurement, the ranging signal phase modulates the uplink carrier. The onboard transponder demodulates the carrier, recovers the uplink ranging signal and retransmits it to ground, phase modulating the downlink carrier. The tone/code at highest frequency defines the accuracy of the measurement, while the other tones/codes are sequentially applied for ambiguity resolution. The error contributions to the ranging measurement are mainly due to delays from the propagation media (plasma and troposphere) and group delay variation for the ground station and onboard electronics.

Both ranging techniques rely on the modulation of a waveform onto the Radio Frequency (RF) carrier which has a relatively narrow fractional bandwidth compared with the Intermediate Frequency (IF). This makes ranging insensitive to pure phase shifts (i.e. non-delay shifts) in the signal path since the carrier phase is tracked out by a much wider band Phased Locked Loop (PLL). Comparing the phase of a received ranging tone/clock with the transmitted tone/clock makes the range measurement. The phase is unwrapped by some form of ambiguity resolution method (e.g. code or tone harmonics)

however this does not affect the ranging accuracy which is dependent only on the accuracy with which the transmitted and received tones at time *t* can be reconstructed.

The uplink tone frequency may be constraint or it may be pre-steered. The transmitted phase at time *t* is:

$$\phi_T(t) = 2\pi f_0 t + 2\pi \cdot \int_0^t F(x)dx \tag{2.5}$$

where f_0 is the tone frequency at time *0* and *F(x)* is an arbitrary pre-steering frequency function. If the total round trip delay at time *t* is *R(t)* then the received phase at *t* is:

$$\phi_R(t) = 2\pi f_0\big(t - R(t)\big) + 2\pi \cdot \int_0^{t-R(t)} F(x)dx \tag{2.6}$$

The range observable is therefore given by:

$$\phi_R(t) - \phi_T(t) = -2\pi f_0 R(t) + 2\pi \cdot \int_t^{t-R(t)} F(x)dx \tag{2.7}$$

If the uplink tone is constant (i.e. *F(x)=0*) then the range, *R(t)*, can be extracted directly from the range observable. If the frequency is not constant it is necessary for the ground station to record *F(t)* precisely so that the range can be computed by an iterative process.

The measured range delay, *R(t)*, is made up of the uplink and downlink station delays, the propagation delay and the spacecraft turnaround delay. The range calibration allows corrections of the delay for two-way coherent ranging with a typical accuracy of a few nanoseconds, which corresponds to a range accuracy of about *1 m* or better (Berner et al., 2007). In general, the delay correction is different from one tracking pass to the next, even for a given DSS. The correction may depend, for example, on the equipment configuration at the DSS and on the band pairing (for example, a X-band uplink paired with a Ka-band downlink). For this reason, mission navigation and radio science teams usually solve for these biases, referred to as *range bias*, as part of orbit determination in order to enhance the accuracy of the range observables for each tracking pass. Rather, the correction of three-way coherent ranging data has an additional problem because the clocks of the two stations are not synchronized. The offset between the clocks can be as large as *3 μs* that represents a bias in the three-way time delay.

2.1.1.3 Delta-Differential One Way Ranging (Δ-DOR)

Very Long Baseline Interferometry (VLBI) is a technique that allows determination of angular position for distant radio sources by measuring the geometric time delay

between received radio signals at two geographically separated stations. The observed time delay is a function of the known baseline vector joining the two radio antennas and the direction to the radio source.

An application of VLBI is spacecraft navigation in space missions where delay measurements of a spacecraft radio signal are compared against similar delay measurements of angularly nearby quasar radio signals. In the case where the spacecraft measurements are obtained from the phases of tones emitted from the spacecraft, first detected separately at each station, and then differenced, this application of VLBI is known as Delta-Differential One-Way Ranging (Δ-DOR). Even though data acquisition and processing are not identical for the spacecraft and quasar, both types of measurements can be interpreted as delay measurements and they have similar information content and similar sensitivity to error sources. The data produced in such a measurement session are complementary to Doppler and ranging data.

The Δ-DOR technique requires that the same quasar and spacecraft be tracked essentially simultaneously during the same tracking pass, at two distinct radio antennas. Thus a viewing overlap between the two antenna complexes is required; the degree of overlap is dependent upon the relative station locations, and varies for each pair of antenna complexes. Normally, a Δ-DOR pass consists of three or more scans of data recording, each of a few minutes duration. A scan consists of pointing the antennas to one radio source and recording the signal. The antennas must slew to another radio source for the next scan, and so on. The observing sequence is spacecraft-quasar-spacecraft, quasar-spacecraft-quasar, or a longer sequence of alternating observations depending on the characteristics of the radio sources and the objectives of the measurement session. A minimum of three scans is required to eliminate clock-epoch and clock-rate offsets and then measures spacecraft angular position. Normally a three-scan sequence is repeated several times. Once collected, the received signals are brought to a common site and correlated. A Δ-DOR observable is generated from a differential one-way range measurement made between the spacecraft and the two ground antennas, and by a measurement of the difference in time of arrival, at the same two stations, of the quasar signal. The observed quantity in a Δ-DOR observation is time delay for each radio source.

For a spacecraft, the one-way range is determined for a single station by extracting the phases of two or more signals emitted by the spacecraft. Modulating a sine wave or square wave onto the downlink carrier at S-band, X-band, or Ka-band generates the DOR tones. Either a pure waveform may be used, producing a spectrum of pure tones, or a modulated waveform may be used, producing a spectrum that more closely resembles the spectrum of a natural radio source. Subtracting the one-way range measurements generated at the two stations forms DOR observables. While the unknown offset in the spacecraft clock affects each one-way range measurement, the station differencing eliminates this effect. However, DOR measurements are still biased by ground station clock offsets and instrumental delays.

For measuring the quasar, each station is configured to acquire data from it in frequency channels centered on the spacecraft tone frequencies. This receiver

configuration choice ensures that the spacecraft-quasar differencing eliminates the effects of ground station clock offsets and instrumental delays. By selecting a quasar that is close in an angular sense to the spacecraft, and by observing the quasar at nearly the same time as the spacecraft, the effects of errors in the modeled station locations, Earth orientation, and transmission media delays are diminished.

In navigation processing, the delay or DOR observable is modeled for each scan of each radio source. The measured observable depends on both geometric factors and on delays introduced by transmission media. Weather data are provided from each tracking site so that, possibly in conjunction with other data such as GPS measurements, corrections can be computed to account for tropospheric and ionospheric path delays. The modeled or 'computed' observable is based on geometric parameters and available calibrations for tropospheric and ionospheric delays. Subtracting the computed observables from the measured time delay values forms residuals. The 'Delta' between spacecraft and quasar observations is generated internal to the navigation processing by subtracting residual values of quasar observations from residual values of spacecraft observations.

Because each Δ-DOR measurement requires the use of two antennas, and navigation accuracy is improved by baseline diversity, this technique is highly conducive to interagency cooperation. The use of Δ-DOR has been very beneficial for the navigation of numerous NASA, ESA, and JAXA missions, beginning with Voyager in 1979. Current and future missions, as MESSENGER and BepiColombo, have planned Δ-DOR for the interplanetary cruise. However, range rate and range observables are still the main data that provide important information about the planetary geodesy. During the orbital phase, both radio science experiments have planned essentially Doppler and ranging data.

2.1.2 Geodetic models

The radio science experiments aim mainly to determine the gravity field of planets or planetary satellites. Radio tracking data, during flybys or orbits, provide information about the gravitational potential of the central body. The quantitative statements of the gravitational field of a generic, non-spherical body is given by a powerful mathematical tool, the multipole series of the spherical harmonic functions. The spherical harmonics provide a representation of the gravitational potential energy per unit mass, produced outside by an isolated body:

$$U = -\frac{GM}{r}\left[1 + \sum_{l=2}^{\infty}\sum_{m=0}^{l}\left(\frac{R_B}{r}\right)^l \bar{P}_{lm}(sin\varphi)[\bar{C}_{lm}cos(m\lambda) + \bar{S}_{lm}sin(m\lambda)]\right] \tag{2.8}$$

where GM is the central body gravitational parameter, l and m are the spherical harmonic's degree and order, R_B is the reference radius of the central body, φ and λ are respectively latitude and longitude. We adopted the normalized representation so that $\bar{P}_{lm}$

are normalized Legendre polynomials and $\bar{C}_{lm}$, $\bar{S}_{lm}$ are the normalized harmonic coefficients. The unnormalized coefficients C_{lm}, S_{lm} are obtained as follows:

$$\begin{pmatrix} C_{lm} \\ S_{lm} \end{pmatrix} = \sqrt{\frac{(l-m)!\,(2l+1)(2-\delta_{0m})}{(l+m)!}} \begin{pmatrix} \bar{C}_{lm} \\ \bar{S}_{lm} \end{pmatrix} = f_{nm} \begin{pmatrix} \bar{C}_{lm} \\ \bar{S}_{lm} \end{pmatrix} \tag{2.9}$$

where δ_{0m} is the *Kronicker delta*.

Generally the coefficients of the same degree *l* have the same order of magnitude, which decreases with *l*. This trend is best described by the mean:

$$C_l^2 = \frac{1}{2l+1} \sum_m \left(C_{lm}^2 + S_{lm}^2 \right) \tag{2.10}$$

analogous to the energy spectrum for a two-dimensional scalar field. It has been noticed that the empirical law (Kaula's rule):

$$C_l^2 = A_K \frac{10^{-10}}{l^4} \tag{2.11}$$

is followed fairly well for the Earth (with A_K=*0.7*) and for terrestrial planets (for *l*>>*1*).

The representation of gravitational potential in spherical harmonics allows defining an important reference surface, the geoid. The geodesy of a planet requires an accurate comparison between the gravity field and the modeling of the topography. The geoid is defined as an equipotential surface of an isolated planetary body. Any deviation of the topographic surface from the geoid contains important information about the crustal structure. The definition of this surface, which represents also the zero of the topographic altitude, is given by:

$$\frac{\delta r}{R_B} = \sum_{l=3}^{\infty} \sum_{m=0}^{l} \bar{P}_{lm}(sin\varphi)[\bar{C}_{lm} cos(m\lambda) + \bar{S}_{lm} sin(m\lambda)] + const \tag{2.12}$$

where δr is the correction to the axisymmetric ellipsoid (determined by C_{20} and C_{22} spherical harmonics, U_C and U_T that are respectively centrifugal and tidal potential) and *const* is the value of the arbitrary constant so that the average of radial correction over the ellipsoid is nil.

The reference ellipsoid and geoid are referenced to the frame defined by the rotational model. Planetary orientations models describe the orientation of the spin axis and prime meridian of the planets in inertial space as a function of time. The current orientation model for Mercury incorporates modern values of the spin orientation, including a formulation for longitude librations (Margot, 2009). The accurate definition

of these rotational parameters is crucial for the geophysics interpretation of Mercury interior structure.

In order to accurately model Mercury's interior structure the Love number k_2 is also determined. Love numbers quantify the deformation of the gravity field of a planet in response to an external perturbing body of mass M_S, which is the Sun for Mercury. The orbit of Mercury around the Sun with a semi-major axis a, causes a tide-raising potential:

$$U^f(r) = \sum_{l=2}^{\infty} U_l^f = \left(\frac{GM_S}{a}\right) \sum_{l=2}^{\infty} \left(\frac{r}{a}\right)^l P_l(\cos\theta) \tag{2.13}$$

where r is the radial coordinate of the point under consideration inside the planet, θ the angle between the planetary mass element at r and the center of mass of M at a, and P_l are Legendre polynomials. Due to the tidally induced mass shift the planet's potential changes by:

$$U_l = k_l \left(\frac{R}{r}\right)^{l+1} U_l^f(R) \tag{2.14}$$

where k_l is the Love number of degree l. Hence, the Love numbers contain important information about the interior structure of a planet. The main effect of the tides on Mercury is given by the Love number k_2. It determines a variation of the equipotential surface:

$$\frac{\delta r}{R} = k_2 \frac{M_S}{M} \left(\frac{R}{a}\right)^3 P_l(\cos\theta) \tag{2.15}$$

The Love number k_2 is a measure for the level of central condensation of an object: the more homogeneous the planet in mass distribution, the bigger the Love number k_2. Maximum homogeneity is represented by a planet of constant density, yielding the maximum value of k_2 of *1.5*. Planets with a core can have typically smaller Love number due to a stronger central condensation.

2.2 Orbit determination

The dedicated instrumentation of radio science experiments allows determining precisely the spacecraft trajectory during the mission. Range and range rate measurements are exploited to improve periodically the reconstruction of spacecraft position and velocity. Deep space probes are visible from Earth for several hours per day providing tracking data that are processed through orbit determination codes. In the general orbit determination problem, both dynamics and measurements models involve nonlinear relationships as follows:

$$\begin{aligned} \dot{\boldsymbol{X}} &= F(\boldsymbol{X}, t) & \boldsymbol{X}(t_k) &\equiv \boldsymbol{X}_k \\ \boldsymbol{Y}_i &= G(\boldsymbol{X}_i, t_i) + \boldsymbol{\varepsilon}_i & i &= 1, \dots, l \end{aligned} \tag{2.16}$$

where $\boldsymbol{X}_k$ is the unknown n-dimensional vector of solved-for parameters (spacecraft state vector components and free parameters of the dynamical model) at the time t_k, and Y_i for $i=1,\dots,l$ is a p-dimensional set of observations that are used to obtain the best estimate of the unknown vector $\boldsymbol{X}_k$, according to an optimum criterion. Orbit determination codes linearize these equations in terms of the state deviation and observation deviation vectors, obtained from a priori estimates of the state parameters:

$$\begin{aligned} \boldsymbol{x}(t) &= \boldsymbol{X}(t) - \boldsymbol{X}^*(t) \\ \boldsymbol{y}_i &= \boldsymbol{Y}_i - G(\boldsymbol{X}_i^*, t) \end{aligned} \tag{2.17}$$

where $()^*$ indicates the reference solution. Therefore, the linearized problem can be written as:

$$\begin{aligned} \dot{\boldsymbol{x}} &= A(t)\boldsymbol{x}(t) \\ \boldsymbol{y}_i &= \tilde{H}_i \boldsymbol{x}_i + \boldsymbol{\varepsilon}_i \qquad (i = 1, \dots, l) \end{aligned} \tag{2.18}$$

where:

$$A(t) = \left[\frac{\partial F(t)}{\partial \boldsymbol{X}(t)}\right]^* \qquad \tilde{H}_i(t) = \left[\frac{\partial G}{\partial \boldsymbol{X}}\right]_i^* \tag{2.19}$$

are the partial derivatives of dynamical and measurement models respect to the state. The orbit determination problem depends strongly on the dynamical models that govern the spacecraft motion. Non-accurate force models provide significant errors in the orbital reconstruction. Therefore, navigation codes aim to correct the large number of solve-for parameters satisfying a defined optimal criterion. Orbit determination methods are generally distinguished with two categories according to their estimation approach: sequential and batch processing.

2.2.1 Sequential processing

The sequential estimation method allows processing each tracking measurement immediately upon receipt to produce an update of a spacecraft's state vector and auxiliary state parameters. This fact makes it well suited for real-time or near-real-time operation. Sequential estimation is particularly well suited to the development of systems to perform orbit determination autonomously on the spacecraft's onboard computer. Spacecraft orbit determination during and just after a maneuver is a critical support function for which orbit determination is needed in near-real-time.

The algorithm was developed originally by Swerling (1959), but the treatment that received more popular acclaim is due to Kalman (1960). In fact, the sequential estimation algorithm is referred to as the *Kalman filter*. The filter is based on the statement that the estimate is to be the best linear, unbiased and minimum variance estimate. The consequences of each of these requirements are addressed in the following steps.

Assuming that an additional observation at epoch t_k is available:

$$y_k = \tilde{H}_k x_k + \epsilon_k \tag{2.20}$$

where $E[\varepsilon_k]=0$ and $E[\varepsilon_k \varepsilon_k^T]=R_k \delta_{kj}$, where δ_{kj} is the *Kronicker delta*, the aim of the filter is to process y_k in order to determine $\hat{x}_k$. The best estimate of x_k, which minimizes the a posteriori covariance matrix, is obtained as:

$$\hat{x}_k = \left(\tilde{H}_k^T R_k^{-1} \tilde{H}_k + \bar{P}_k^{-1}\right)^{-1} \left(\tilde{H}_k^T R_k^{-1} y_k + \bar{P}_k^{-1} \bar{x}_k\right) \tag{2.21}$$

where $\bar{x}_k$ and $\bar{P}_k$ are respectively the a priori state and covariance matrix, computed by means of the state transition matrix $\phi(t_k,t_{k-1})$ as follows:

$$\bar{x}_k = \phi(t_k, t_{k-1}) \hat{x}_{k-1} \qquad \bar{P}_k = \phi(t_k, t_{k-1})\ P_{k-1} \phi^T(t_k, t_{k-1}) \tag{2.22}$$

Defining the *Kalman gain* as:

$$K_k \equiv \bar{P}_k \tilde{H}_k^T \left[\tilde{H}_k \bar{P}_k \tilde{H}_k^T + R_k\right]^{-1} \tag{2.23}$$

then the covariance matrix can be expressed in the compact form:

$$P_k = \left[I - K_k \tilde{H}_k\right] \bar{P}_k \tag{2.24}$$

that satisfy the criterion of minimum variance.

The sequential form for computing $\hat{x}_k$ can be written as:

$$\hat{x}_k = \bar{x}_k + K_k \left[y_k + \tilde{H}_k \bar{x}_k\right] \tag{2.25}$$

that is the recursive correction to the reference trajectory:

$$\hat{X}_k = X_k^* + \hat{x}_k \tag{2.26}$$

The main disadvantage of the sequential algorithm is that the state estimation error covariance matrix may approach zero as the number of observations becomes large. The magnitude of the covariance matrix elements decreases depending on the density, information content, and accuracy of the observations. Examination of the estimation algorithm shows that as $P_k \rightarrow 0$ the gain approaches zero, and the estimation procedure

become insensitive to the observations. Consequently, the estimate diverges due to either errors introduced in the linearization procedure, computational errors, or errors due to an incomplete mathematical model. To overcome this problem, process noise often is added to the state propagation equations ($\bar{P}_k = \phi(t_k, t_{k-1})\, P_{k-1}\phi^T(t_k, t_{k-1}) + Q_k$).

Furthermore, if the true state and the reference state are not close together then the linearization assumption may not be valid and the estimation process may diverge. To minimize the effects of errors due to the neglect of higher order terms in the linearization procedure, the extended form of the sequential estimation algorithm is often used. This algorithm is referred to as the *Extended Kalman Filter* (*EKF*). The primary difference between the sequential and the extended sequential algorithm is that the reference trajectory for the extended sequential algorithm is updated after each observation to reflect the best estimate of the true trajectory. Therefore, after processing the k^{th} observation, the best estimate of the state vector at t_k is used to provide new initial conditions for the reference trajectory:

$$(X_k^*)_{new} = \hat{X}_k = X_k^* + \hat{x}_k \tag{2.27}$$

The advantage of the extended sequential algorithm is that convergence to the best estimate is more rapid because errors introduced in the linearization process are reduced. Nevertheless, batch algorithms are generally preferred in case of interplanetary orbit determination problem.

2.2.2 Batch least-squares processor

Most filters used for interplanetary orbit determination problem are based on a least-squares (LS) solution, which selects the best estimate of $\boldsymbol{x}$ by minimizing the sum of the squared residuals. Given a vector sequence of observations $\boldsymbol{y}_1, \boldsymbol{y}_2, \ldots, \boldsymbol{y}_l$ related through the state transition matrix to the state at some epoch time $\boldsymbol{x}_k$, and associated weighting matrix, w_i, for each of the observation vectors:

$$\begin{aligned} \boldsymbol{y}_1 &= H_1\boldsymbol{x}_k + \boldsymbol{\epsilon}_1; \quad w_1 \\ \boldsymbol{y}_2 &= H_2\boldsymbol{x}_k + \boldsymbol{\epsilon}_2; \quad w_2 \\ &\vdots \\ \boldsymbol{y}_l &= H_l\boldsymbol{x}_k + \boldsymbol{\epsilon}_l; \quad w_l \end{aligned} \tag{2.28}$$

where the matrix H_i is the product of the mapping matrix to the state transition matrix as follows:

$$H_i = \tilde{H}_i\phi(t_i, t_k) \tag{2.29}$$

Assuming the weighting matrices, w_i, to be the elements in the diagonal matrix W, each observation $\boldsymbol{y}_i$, a p-vector, allocated in the vector $\boldsymbol{y}$ satisfies the following expression:

$$\boldsymbol{y} = H\boldsymbol{x}_k + \boldsymbol{\varepsilon}; \quad W \tag{2.30}$$

Therefore, the well-known weighted LS solution with a priori information is:

$$\hat{\boldsymbol{x}}_k = (H^T W H + \bar{W}_k)^{-1}(H^T W \boldsymbol{y} + \bar{W}_k \bar{\boldsymbol{x}}_k) \tag{2.31}$$

where $\bar{W}_k$ represent the *a priori* covariance matrix of x_k and $(H^T W H + \bar{W}_k)$ is referred to as the *normal matrix*. The iteration of this process allows obtaining the best estimate of $\boldsymbol{x}$ in the case of planetary flybys or trajectories of few days.

The batch least-square method is often compared to the sequential methods to justify their use, as these are the two basic data processing procedures for tracking data used to estimate a spacecraft's orbit. A disadvantage of both methods is that if the true and reference state are not close together, the linearization assumptions are not valid and the estimation process will diverge (Tapley, 1989). The batch and sequential algorithms are both iterated until convergence. The LS processor obtain near convergence when the *residuals* $\boldsymbol{y}$ of the tracking data, which represent the differences between the observations and the *computed observations* using the reference values, are close to the root-mean-square (RMS) of the data noise.

Process noise in the batch processor complicates the solution of the normal equations, the dimension of the normal matrix increase from *n* (number of the solve-for parameters) to $m=p\times l$ (total number of observations). Without process noise, the sequential algorithm can be shown to be mathematically equivalent to the batch process. Given the same data set, both will produce the same estimates when mapped to the same times. However, process noise is added in the EKF and this algorithm is not equivalent to the batch processor, but has been shown to be very close (Tapley, 2004).

Batch processing allows for simultaneous use of multiple measurements, hence making it most useful for post-flight analysis of very large observation datasets. It provides an estimate of the state at some chosen epoch using an entire batch or set of data. Nevertheless, this solution could not be sufficient when the dynamics of the spacecraft is quite complicated and when there are a large number of solve-for parameters. In such case, the trajectory could be subdivided into small arcs (i.e. single day). It allows obtaining the continuously convergence of the single arc estimation and using the multi-arc approach that improves considerably the estimation of the common parameters.

2.2.3 Multi-arc approach

In several space geodesy experiments the number of parameters to be determined is quite large. This problem is in many cases severe, to the point that a single batch estimation becomes impractical. In addition, deterministic models are unable to reliably account for non-gravitational perturbations. In many cases a multi-arc (MA) method alleviates these problems, although the presence of disturbances may end up in a

divergence in the estimation process. In a MA approach the orbit of the spacecraft is fragmented into different arcs, corresponding to non-overlapping time intervals. Each arc is completely independent from the others, because the initial conditions of the state vector of the probe do not depend in any way on the orbital propagation of the preceding arcs. The estimated parameters are divided into two categories: the *local* parameters, pertaining to the single arc (i.e. state vector, maneuvers, etc.), and *global* parameters, independent of time and pertaining to all arcs (mass and gravitational harmonics of the central body, for example).

The main goal of this over-parameterization is to absorb the effects and errors caused by unmodelled dynamics, errors that accumulate with time. Therefore, the length of every arc should be chosen so as to maintain the errors in the dynamical model at a level compatible with the observation errors. The arc length must be chosen judiciously: if too long, the errors accumulate, if too short the solution becomes unstable.

In a classical MA estimation, the solution vector $x=[g;l]$ is split into the vectors g and l of respectively global and local parameters. The observations and the corresponding residuals are partitioned into n arcs, such a way that the observable vector is given by $y=[y_1; y_2;\ldots; y_n]$. The vector l is further split into vectors l_i, one for each arc. Each sub-vector l_i is associated to the arc with the same index i, in such a way that the residuals from one arc do not depend upon the local parameters of another arc:

$$H_g^{(j)} = \frac{\partial y_j}{\partial g} \qquad H_{l_i}^{(j)} = \frac{\partial y_j}{\partial l_i} = 0 \qquad \text{for i} \neq \text{j} \tag{2.32}$$

The mapping matrix H is structured as follows:

$$H = \begin{pmatrix} H_{l_1}^1 & 0 & \cdots & 0 & H_g^1 \\ 0 & \ddots & & \vdots & \vdots \\ \vdots & & H_{l_{n-1}}^{n-1} & 0 & H_g^{n-1} \\ 0 & \cdots & 0 & H_{l_n}^n & H_g^n \end{pmatrix} \tag{2.33}$$

Therefore, the observables of each arc depend only on the local parameters of the same arc and on the global parameters. The contributions of each arc to the overall normal equation are:

$$\begin{aligned} \Lambda_{l_i l_j} &= \left(H_{l_i}^{(i)}\right)^T H_{l_i}^{(j)} = \Lambda_{l_i l_j}^T = 0 \qquad \text{for i} \neq \text{j} \\ \Lambda_{g l_i} &= \left(H_g^{(i)}\right)^T W_i H_{l_i}^{(i)} = \Lambda_{l_i g}^T \\ \Lambda_{gg} &= \sum_{i=1}^{n} \left(H_g^{(i)}\right)^T W_i H_g^{(i)} = \Lambda_{gg}^T \end{aligned} \tag{2.34}$$

where W_i is the weighting matrix of the observables in the arc i.

These matrices are generally diagonal and each element is chosen to be the inverse of the squared RMS of the considered observable. The normal matrix Λ has an arrow-like structure as follows:

$$\Lambda = \begin{pmatrix} \bar{\Lambda}_{gg} & \Lambda_{gl_1} & \Lambda_{gl_2} & \cdots & \Lambda_{gl_n} \\ \Lambda_{l_1 g} & \bar{\Lambda}_{l_1 l_1} & 0 & \cdots & 0 \\ \Lambda_{l_2 g} & 0 & \bar{\Lambda}_{l_1 l_1} & & \vdots \\ \vdots & \vdots & & \ddots & 0 \\ \Lambda_{l_n g} & 0 & \cdots & 0 & \bar{\Lambda}_{l_1 l_1} \end{pmatrix} \tag{2.35}$$

where:

$$\begin{aligned} \bar{\Lambda}_{gg} &= \left(\Lambda_{gg} + \bar{W}_g^{-1}\right) \\ \bar{\Lambda}_{l_i l_i} &= \left(\Lambda_{l_i l_i} + \bar{W}_{l_i}^{-1}\right) \quad \text{for } i = 1, \dots, n \end{aligned} \tag{2.36}$$

with $\bar{W}_g$ and $\bar{W}_l$ are the a priori covariance matrix respectively for global and local parameters. The contributions to the right hand side $D=[D_g;D_l]$ of the normal equation are:

$$\begin{aligned} D_g &= \sum_{i=1}^{n} \left(H_g^{(i)}\right)^T W_i y_i \\ D_{l_i} &= \left(H_{l_i}^{(i)}\right)^T W_i y_i \qquad \text{for } i = 1, \dots, n \end{aligned} \tag{2.37}$$

Then the normal equation is a system of two vector equations (Milani, 2008):

$$\begin{cases} \bar{\Lambda}_{gg} \Delta g + \Lambda_{gl} \Delta l = D_g \\ \Lambda_{lg} \Delta g + \bar{\Lambda}_{ll} \Delta l = D_l \end{cases} \tag{2.38}$$

given by minimization of the least-squares cost function. By solving for Δl in the second equation: the matrix $\bar{\Lambda}_{ll}$ is block diagonal, thus it is possible to invert each diagonal block $\bar{\Lambda}_{l_i l_i}$ separately:

$$\Delta l_i = \bar{\Lambda}_{l_i l_i}^{-1} \left[D_{l_i} - \Lambda_{l_i g} \Delta \mathrm{g}\right] \tag{2.39}$$

implying that the corrections to the local parameters l_i are not the same that would be obtained by neglecting the interaction with the global parameters, expressed by the sub-matrix $\Lambda_{l_i g}$ (Milani, 2008). These expressions for Δl_i can be substituted into the first equation, giving the solution for the global parameters:

$$\Delta g = \Gamma_{gg}\left[D_g - \sum_{i=1}^{n} \Lambda_{gl_i}\overline{\Lambda}_{l_i l_i}^{-1} D_{l_i}\right] \tag{2.40}$$

where $\Gamma_{gg} = \left(\bar{\Lambda}_{gg} - \sum_{i=1}^{n} \Lambda_{gl_i}\overline{\Lambda}_{l_i l_i}^{-1}\Lambda_{l_i g}\right)^{-1}$ is the covariance of the global parameters. The corrections and the covariance of the global are in general not the same as in a separate global-only correction. The corrections to the local parameters are found by substituting Δg into the previous equation:

$$\Delta l_i = \overline{\Lambda}_{l_i l_i}^{-1}\left[D_{l_i} - \Lambda_{l_i g}\Gamma_{gg} D_g + \Lambda_{l_i g}\Gamma_{gg}\sum_{i=1}^{n} \Lambda_{gl_i}\overline{\Lambda}_{l_i l_i}^{-1} D_{l_i}\right] \tag{2.41}$$

Their covariance can be deduced by comparing with the formula giving the correction by means of the full covariance matrix:

$$\Delta l_i = \Gamma_{l_i l_i} D_{l_i} + \Gamma_{l_i g} D_g \sum_{j \neq i} \Gamma_{l_i l_j} D_{l_j} \tag{2.42}$$

thus the covariance matrix of the local parameters l_i is:

$$\Gamma_{l_i l_i} = \overline{\Lambda}_{l_i l_i}^{-1} + \overline{\Lambda}_{l_i l_i}^{-1}\Lambda_{l_i g}\Gamma_{gg}\Lambda_{g l_i}\overline{\Lambda}_{l_i l_i}^{-1} \tag{2.43}$$

The main advantage of the multi-arc decomposition is that the normal matrix has large portions zero, thus it is not necessary to store the full matrix during the computation. However, the covariance matrix is full and the limit of the normal-equations formulation is therefore represented by the difficulty of inverting the normal matrix. The Square-Root (SR) form, which represents the current formulation adopted in our software, overcomes this critical issue. The parameter estimate are therefore obtained by the inversion of a triangular matrix ($R=H^T W^{1/2}$) whose condition number is the square root of the condition number of the normal matrix, reducing drastically the numerical errors.

One of the most serious problems of the multi-arc approach is the stability of the solution. Attaining convergence can prove very difficult when, the number of parameters is large, as in the case of radio science experiments at Mercury. The nominal spacecraft trajectory represents a critical issue in the initialization of the multi arc estimation. If the true and reference spacecraft state vectors in each arc are not close together, the estimation process may diverge. In classical batch processing the reference trajectory, given by the navigation team, may prove not accurate enough for multi-arc analysis. Convergence and orbital solutions improve considerably by using a preliminary single arc trajectory reconstruction with sequential updates of the global parameters (batch-

sequential processing). The dynamical model is sequentially updated and improved, as additional data batches are included in the solution.

2.3 Batch-sequential processing

The orbit determination software of deep space missions uses generally as statistical estimation method a Square Root Information Filter (SRIF), which is mathematically exactly equivalent to weighted least squares, but it is numerically superior. The SRIF relies on a so-called epoch-state formulation; indeed, the components of the spacecraft state vector are estimated at a fixed epoch. The spacecraft state can be augmented by other parameters that are treated as solve-for-parameters. The Orbit Determination Program (ODP) of the Jet Propulsion Laboratory (JPL) is based exactly on these properties and it is the software that has been used for the navigation of NASA interplanetary missions. Thanks to the agreement between the JPL and the Italian Space Agency, we have the opportunity to use the ODP for our scientific research.

The general approach for orbit determination of deep space probes requires the partition of the mission into different arcs, whose length relies on the tracking pass. Each *arc* is therefore processed in the SRIF in order to carry out the estimation of the state vector at a certain epoch. The errors in the dynamical model are generally compensated with solve-for-parameters of the dynamical model and/or stochastic accelerations that absorb the unmodeled effects. The navigation team of interplanetary missions, which provide reconstructed trajectory of the spacecraft in kernels, generally applies this estimation strategy, referred to as *single-arc-estimation*.

The complexity of interplanetary mission scenarios, as MESSENGER and BepiColombo, suggests that single-arc-estimation is not sufficient to achieve an extremely accurate orbit determination. The reconstructed trajectory, as a priori of the state vectors in the multi-arc approach, leads to divergence in the estimation of the common parameters (i.e. gravity field). Therefore, we have considered worthwhile the adoption of an estimation process able to reduce the risk of parameter aliasing from mismodeled non-conservative forces. To this end, we have adopted a batch-sequential estimation scheme that we have developed as a paramount structure of routines about the ODP. This estimator is tailored to the need to provide a reconstruction of the spacecraft orbit and the gravity field of Mercury with increasing fidelity as additional data are received and processed. The incoming data are processed in batches of selectable length starting from a solution and information matrix obtained from data collected previously. The updated solution and covariance matrix for the spacecraft state vector and gravity field is then used in the processing of the next batch. Our data processing procedure is based on a preliminary reconstruction of the spacecraft trajectory that represents the initial guess for a final global fit to determine the gravity field harmonic coefficients. The main advantage of this estimation process is the sequential analysis of new data during

the mission. The orbit reconstruction is therefore continuously updated since additional data are collected.

2.3.1 Preliminary orbit reconstruction

The main motivation of the batch-sequential processing is to improve the preliminary orbit reconstruction of the spacecraft. The mission is partitioned in different arcs and each arc is processed in the SRIF in order to estimate the state vector at the start epoch of the arc. We propagate the state vector and its associate covariance matrix forward to the start epoch of the consecutive arc. This procedure determines that the a priori of the state vector is given by the sequential update from the previous arc (Figure 2.1). After a certain number of arcs, these arcs are collected in a *batch* and combined in an intermediate global fit (multi-arc approach). Sequential updates of the dynamical model, including the gravity field coefficients, are obtained at the end of each batch (Figure 2.2). Both updates of the state vector and the dynamical parameter approach the estimated state to the real state reducing considerably the time for convergence and the instability in a final global fit of the mission.

The choice of the batch length is particularly important for a fast convergence and a good accuracy of the final orbital solutions. Its length is a trade off between the estimation accuracy of global and local parameters. If too long, the state vector errors accumulate because of unmodeled effects, if too short the solve-for parameters of the dynamical model are not accurately estimated. For instance, in the case of an orbiter around Mercury an appropriate length of a batch is about *27* days (half Hermean day). This period represents a good time span to obtain an accurate estimation of the Hermean gravity field because the spacecraft covers about half surface of the planet.

A single batch is processed following three essential steps:

- *single-arc-estimation* of a limited number of arcs, with the propagation of state vector and its associated uncertainties;

- *multi-arc estimation* with initial conditions and a priori uncertainties respectively equal to the estimated values (weighted mean for the global parameters, with formal uncertainties as weights) and the a priori uncertainties of the single arc estimation;

- update of the dynamical model with the estimated parameters for the next batches.

With this procedure the processing of the following arcs benefits from an improved dynamical model, thus allowing a better estimate of the state vector. In addition, this sequential updating leads also to improved estimates of the global parameters, which attain convergence after a limited number of batches. However, the results from this first

iteration may still be improved, both for the state vector and global parameters estimation. The initial batch processing is only the starting point of a two-step estimation process. The first step just described has two important tasks, namely to prepare the initial conditions of each single arc and improve the knowledge of the dynamical model. The second step uses the improved dynamical model to initialize the global multi-arc estimation. The batch-sequential estimation provides therefore the nominal values and the a priori uncertainties for a final global fit.

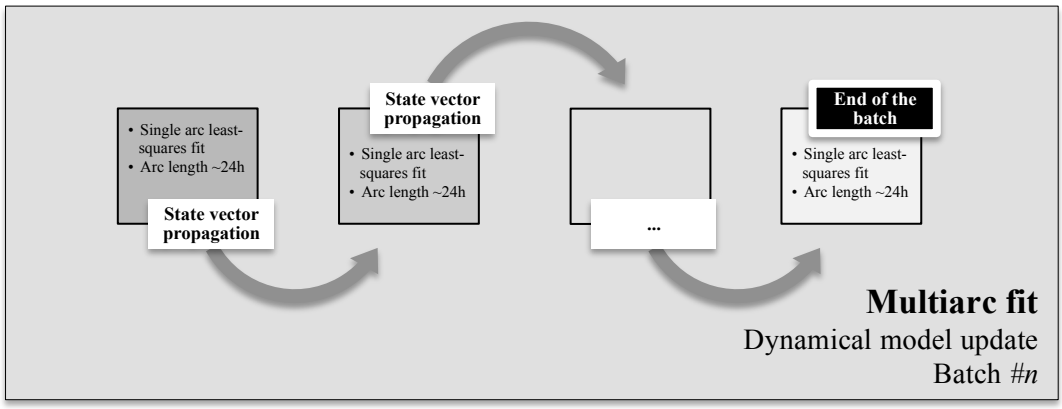

Figure 2.1 Single batch estimation process

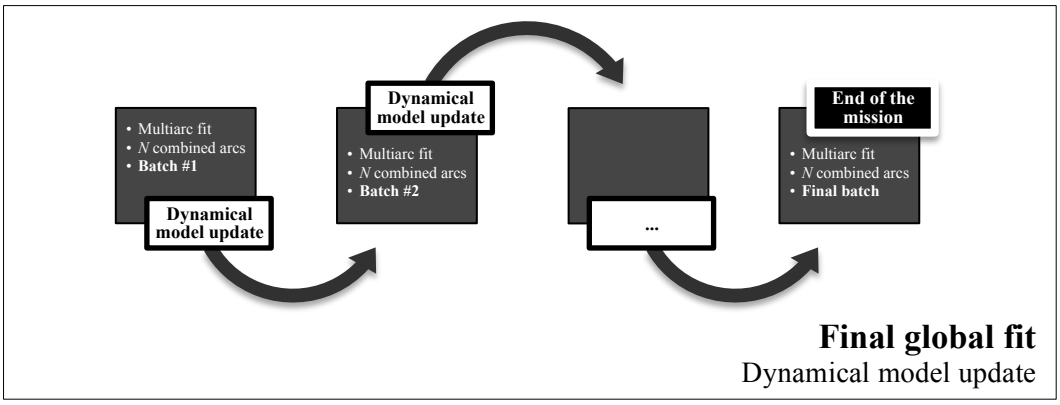

Figure 2.2 Combined solution of all batches

2.3.2 Combined estimation

The preliminary orbit reconstruction provides a rough estimate of the spacecraft state vector during the mission. Although the trajectory is not yet accurately determined, the state vectors of each single arc are used as initial conditions in a final global fit. The

batch-sequential processing allows recovering a more precise spacecraft orbit compared with a classical batch single arc estimation process. The sequential updates reduce drastically the errors on both position and velocity vectors of the spacecraft as showed in the numerical simulations of BepiColombo radio science experiment in *Section 4.3.2*. The reference trajectory is therefore close enough to the true trajectory allowing a combined estimation of all arcs.

The multi-arc analysis preserves the partition of the mission in N arcs so that the total amount of solve-for parameters is given by the sum of the *global* and *N*local*. In the case of orbiter around Mercury the local parameters are generally the state vector, residual ΔV or accelerometer noise (bias and drift). Whereas the global parameters are the gravity field harmonic coefficients, whose number grows with the considered degree (the coefficients up to degree *20* is *438*, for example) and spacecraft surface reflectivity that determines solar and planetary radiation pressure contribution.

The batch-sequential estimation provides the nominal values and the a priori uncertainties for global multi-arc setup. The global parameters may be initialized either with the estimation of the last batch or with the initial nominal values. The combined estimation may hence provide an improved estimate of the global parameters. Once the dynamical model is recovered to the required accuracy, the orbit reconstruction may be obtained by means of final single-arc-estimation.

Chapter 3

MESSENGER

Outline. The Mercury Surface, Space Environment, GEochemestry, and Ranging (MESSENGER) spacecraft, launched on August 3, 2004, is orbiting the planet Mercury. The mission, spacecraft and payload are designed to answer fundamental questions regarding the innermost planet. The orbital phase, began on March 18, 2011, is a near-polar-orbital observational campaign that addresses all mission goals. The instruments on board the spacecraft allow in particular completing global imaging, yielding detailed surface compositional and topographic data over the northern hemisphere and the recovery of Mercury's gravity field from ranging and Doppler measurements. Since September 2011, the radio tracking data of the first six months of the mission were published[1] with paramount ancillary information necessary for the MESSENGER orbit determination. The desire of testing the batch-sequential estimation strategy, developed in the context of BepiColombo numerical simulations, and the necessity of determining the lower degree of Mercury's gravity field led us to analyse the first 110 days MESSENGER radio tracking data. We provide a model of Mercury's gravity field (20×20) and ephemeris showing the results carried out by means of the batch-sequential estimation process.

3.1 Mission overview

MESSENGER as part of the Discovery Program of NASA has been orbiting Mercury for about two Earth years after the endorsement of the extended mission. The spacecraft completed three flybys of Mercury following two flybys of Venus and one of Earth (Figure 3.1). The Mercury flybys returned significant new data early in the mission, while the orbital phase, guided by the flight data, enable a focused scientific investigation of the innermost planet. Answers to key questions about Mercury's high density, crustal composition and structure, volcanic history, core structure magnetic field generation,

[1] http://pds.nasa.gov/

polar deposits, atmosphere, overall volatile inventory, and magnetosphere are provided by an optimized set of seven miniaturized scientific instruments (Solomon et al., 2007).

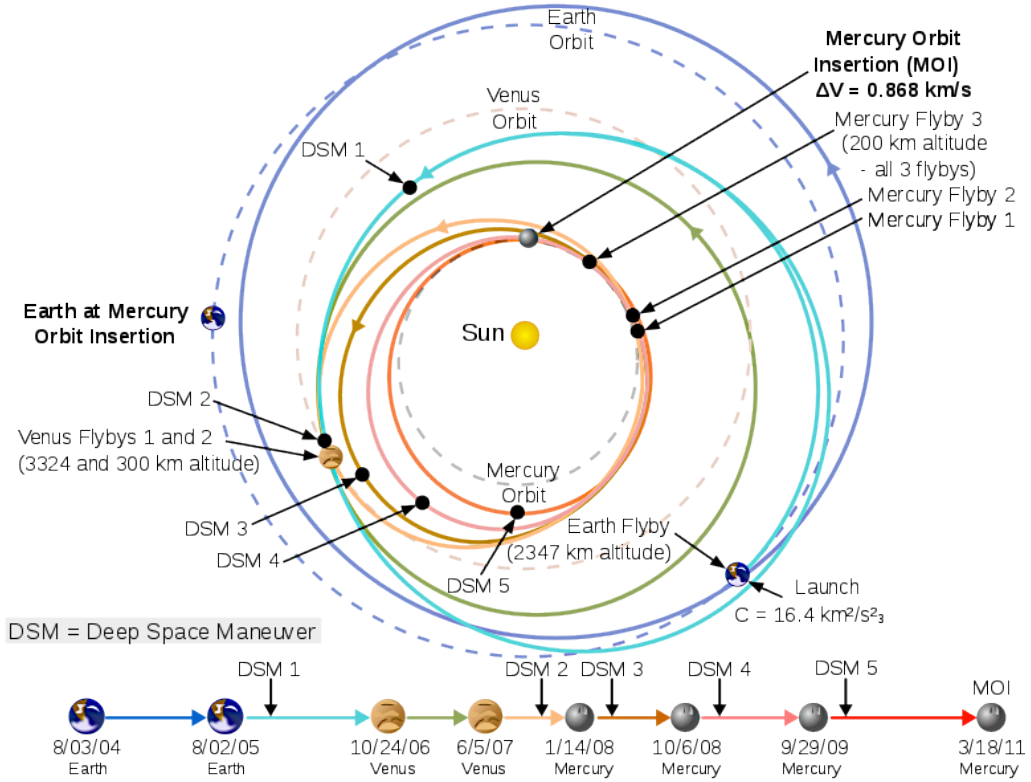

Figure 3.1 MESSENGER interplanetary orbit (McAdams et al., 2007)

On March 18, 2011, the MESSENGER spacecraft was inserted into a *~12-hour*, near-polar orbit around Mercury, with an initial pericenter altitude of *200 km*, initial pericenter latitude of *60°N*, and apoapsis at *~15200 km* altitude in the southern hemisphere (Figure 3.2). As a result of solar torques, the pericenter latitude drifts northward and the minimum altitude progressively increases.

Once per *88-day* Mercury year the spacecraft execute Orbit Correction Maneuvers (OCM) to return the minimum altitude to *200 km* (McAdams et al., 2007). Otherwise propulsive events are minimized to permit the recovery of Mercury's gravity field from ranging and Doppler velocity measurements (Srinivasan et al., 2007). The orbital phase of the mission was scheduled for one Earth year, or slightly longer than two Mercury solar days. At the end of the nominal mission the pericenter latitude was *72°N*. However, MESSENGER entered an extended mission scheduled to last until March 2013 changing significantly the nominal orbit with the eccentricity decrement.

While in Mercury orbit, observations are staged by altitude and time of day so as to maximize scientific return among all scientific instruments, subject to restrictions on

spacecraft attitude set by the need to maintain sunshade pointing within small angular deviations in yaw and pitch of the sunward direction (Leary et al., 2007). The Mercury Dual Imaging System (MDIS) built on the flyby imaging to create global color and monochrome image mosaics during the first six months of the orbital phase; a global monochrome base mosaic was obtained at *250-m*/pixel or better average spatial sampling, low emission angle, and moderate incidence angle, and a global color mosaic was obtained at a resolution of *2 km*/pixel or better. Emphasis during the second six months shifted to targeted, high-resolution imaging (up to *~20 m*/pixel resolution) with the Narrow-Angle Camera (NAC) and repeated mapping at a different viewing geometry to carry out global stereogrammetry (Hawkins et al., 2007). The Gamma-Ray and Neutron Spectrometer (GRNS) and the X-Ray Spectrometer (XRS) built up observations that yield global maps of elemental composition at resolutions that vary with latitude, species, and (for XRS) the intensity of the solar X-ray flux (Goldsten et al., 2007; Schlemm II et al., 2007). The MAGnetometer (MAG) measured the vector magnetic field over six Mercury sidereal days (each *58.65* Earth days) under a range of solar distances and conditions, which should permit separation of internal and external fields sufficient to resolve Mercury's quadrupole magnetic moment (Korth et al., 2004) and shorter-wavelength features near pericenter latitudes (Anderson et al., 2007).

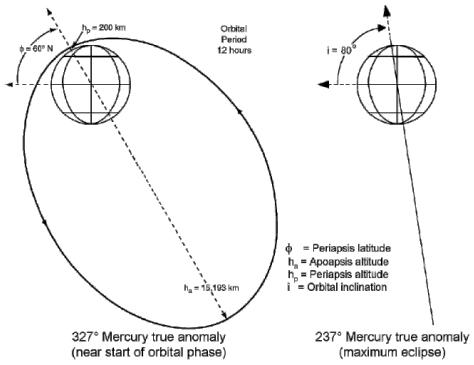

Figure 3.2 MESSENGER's nominal orbit about Mercury (Solomon et al., 2007)

The Mercury Laser Altimeter (MLA) measured the topography of the northern hemisphere over eight Mercury years (Cavanaugh et al., 2007). The radio science extended topographic information to the southern hemisphere by occultation measurements of planet radius, and the planet's obliquity and the amplitude of the physical libration may be determined independently from the topography and gravity field (Srinivasan et al., 2007). The radio tracking data lead especially to recover the Mercury's gravity field and the planetary ephemeris. The Visible-Infrared Spectrograph (VIRS) component of the Mercury Atmospheric and Surface Composition Spectrometer (MASCS) instrument produced global maps of surface reflectance from which

mineralogy and its variation with geological unit can be inferred, and the UltraViolet-Visible-Spectrometer (UVVS) component of the MASCS instrument produced global maps of exospheric species abundances versus altitude and their temporal variations over eight Mercury years and a range of solar activity (McClintock and Lankton, 2007). The Energetic Particle and Plasma Spectrometer (EPPS) sampled the plasma and energetic particle population in the solar wind, at major magnetospheric boundaries, and throughout the environment of Mercury at a range of solar distances and levels of solar activity (Andrews et al., 2007).

Instrument	Measurements
Mercury Dual Imaging System (**MDIS**)	Global mapping of landforms, track variations in surface spectra
Gamma-Ray and Neutron Spectrometer (**GRNS**)	Abundances of different surface elements (possible ice at poles)
X-Ray Spectrometer (**XRS**)	Abundances of various elements in the materials of Mercury's crust
MAGnetometer **MAG**)	Mapping Mercury's magnetic field and regions of magnetized rocks
Mercury Laser Altimeter (**MLA**)	High accurate descriptions of Mercury's topography
Mercury Atmospheric and Surface Composition Spectrometer (**MASCS**)	Abundances of atmospheric gases and minerals on the surface
Energetic Particle and Plasma Spectrometer (**EPPS**)	Composition, distribution, and energy of charged particles in Mercury's magnetosphere
Radio Science (**RS**)	Mercury's mass distribution, including variations in crust thickness

Table 3.1 MESSENGER scientific payload

An additional important constraint on payload observing sequences was imposed by a rate of data downlink from the spacecraft to the DSN that varies strongly with time during the mission orbital phase. The strategy to deal with such a variable data return was to store most data on the spacecraft solid-state recorder during periods when Mercury is far from Earth and to downlink combinations of stored data and newly acquired data during periods when Mercury is closest to Earth. A data prioritization scheme assisted in managing the downlink process. A total of more than *100 Gb* of data were returned during the nominal mission orbital phase, downlinking to DSN stations for on average *6.5 hours* per mission day.

The orbital observation strategy was based on a combination of position along the orbit and a balance between available downlink and solid-state recorder resources. The exploratory nature of this mission requires built-in flexibility in the planning strategy in order to take maximum advantage of what is learned during the flybys and the early part

of the orbital phase. Many of the instruments operate in conjunction with each other in observational campaigns that are defined by science objectives but are constrained by limits on data volumes. Margin and multiple opportunities for high-priority observations were therefore incorporated into the strategy where possible.

3.2 Radio science

The MESSENGER Radio science experiment relies strictly on the Radio Frequency (RF) Telecommunications Subsystem on board the spacecraft. The aims of this subsystem consist in sending commands to the spacecraft, transmitting information on the state of the spacecraft and scientific observations, and assisting in navigating the spacecraft to and in orbit about Mercury by providing precise observations of the spacecraft's Doppler velocity and range in the line of sight to Earth. The RF signal is transmitted and received at X-band frequencies (7.2 GHz uplink, 8.4 GHz downlink) by the NASA Deep Space Network. The tracking data from MESSENGER contribute significantly to achieving the mission's geophysics objectives. The RF subsystem, as the radio science instrument, help determine Mercury's gravitational field and, in conjunction with the Mercury Laser Altimeter instrument, help determine the topography of the planet. Further analysis of the data may improve the knowledge of the planet's orbital ephemeris and rotation state.

3.2.1 Radio Frequency Telecommunications Subsystem

The MESSENGER RF Telecommunications Subsystem operates at X-Band: 7.2 GHz for uplink from ground stations and 8.4 GHz for downlink from the spacecraft. Communications are accomplished via the 34-m and 70-m antennas of NASA's Deep Space Network (DSN) stations in Goldstone, California, USA; Madrid, Spain; and Canberra, Australia. Because of the inner-planet trajectory of MESSENGER, the Earth can be in any direction with respect to the spacecraft. This geometric constraint presents a significant RF design requirement in that high-gain coverage must be achievable in all directions. The antenna configuration shown in Fig. 3.3 accomplishes this requirement. Two diametrically opposite-facing Phased-Array Antennas (PAAs) provide the high-gain downlink signal. Each PAA is capable of electronically steering $\pm 60°$ in the XY-plane of the spacecraft from the directions indicated in Fig. 3.3. Spacecraft rotation about the Y-axis in conjunction with the electronic scanning of the antenna beam provides the omnidirectional high-gain coverage. Two fanbeam antennas provide medium-gain uplink and downlink capabilities, and four low-gain antennas (LGAs) complete the antenna suite of MESSENGER.

Redundant X-Band Small Deep Space Transponders (SDSTs), provided by General Dynamics, are responsible for receiving and demodulating the RF uplink signal, generating and modulating the RF downlink signal, and turning around uplinked ranging

and Doppler components. Each SDST's downlink signal (only one is active at any given time) is routed via a passive hybrid coupler to both solid-state power amplifiers (SSPAs). Each SSPA can be in one of four modes: "distributed front", "distributed back", "lumped", and "off." The "distributed" modes of the SSPAs feed the RF downlink signal to either the front or the back PAA; the "lumped" mode of the SSPA feeds the RF downlink signal, via the two RF switch assemblies, to the fanbeam antenna or the LGAs. In the "distributed" mode, the RF signal is split eight ways and routed to eight "stick amplifiers". Each stick amplifier consists of a four-bit phase shifter (that controls the steering of the phased-array antenna beam), a small-signal amplifier, a driver amplifier, a power amplifier, and an isolator. The output power of each stick amplifier is approximately *34 dBm*; in a distributed mode, a total of four sticks are operational per SSPA, yielding an output power of approximately *40 dBm*. The "lumped" mode of the amplifier offers a *40-dBm*-power output or the fanbeam and low-gain antennas (Srinivasan et al., 2007).

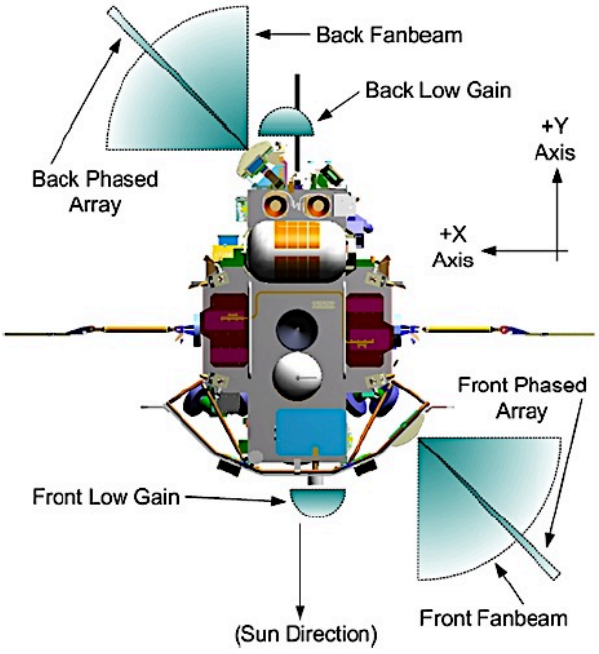

Figure 3.3 The MESSENGER spacecraft antenna suite (Srinivasan et al., 2007)

3.2.2 Tracking operations

MESSENGER's X-band tracking provides the line-of-sight velocity of the spacecraft and the distance of the spacecraft from Earth. The specified accuracy of the velocity measurement for the RF subsystem is to within *±0.1 mm/s* over a *60-s* integration period. The Doppler (Earth line-of-sight velocity) measurements are derived from the change in

the carrier frequency, taking into account the frequency translation in the on board transponder. Through the first *400 days* of cruise, the average typical *1-σ* Doppler residual is on the order of *0.03 mm/s*. This measurement, provided by the navigation team, includes the contributions from all the non-RF sources (e.g., Earth tropospheric and ionospheric effects) and confirms that the RF subsystem was performing well within its specifications. The ranging measurements are made via standard sequential tone ranging. These data assist in fitting the Doppler data to a precise orbit. The DSN transmits a series of ranging tones; the onboard transponder receives these tones and retransmits them back to Earth. The difference between the time of transmission of the ranging tones and the time of reception of the tones, along with knowledge of the transmission delay within the spacecraft, yields the spacecraft range. Measurements of the internal spacecraft delay taken during ground testing ranged from *1356.89 ns* to *1383.74 ns* depending on the RF configuration (transponder, SSPA, and antenna configuration). A more precise delay time is used for science operations at Mercury; however, even a *20-ns* error in this estimate would lead to a range error of only *3 m* (Srinivasan et al., 2007).

In the Mercury orbit phase, MESSENGER completes two revolutions per Earth day, and it is planned to acquire tracking data during each DSN contact pass. The baseline is to have *12* eight-hour tracks per week. From these data the spacecraft position and velocity is derived and used to predict the future position of MESSENGER to enable the targeting of the instruments. In addition, these same data is used in the analysis of the instrument data by providing precise positions at which the previous observations were made.

In Mercury orbit, the RF configuration route the uplink through the most favorable fanbeam antenna and the downlink via a phased array for high-rate data-transmission passes. During these passes, the RF signal levels are sufficiently high to acquire good tracking (Doppler and range) data. However, during the passage in proximity to the periherm, the spacecraft is oriented such that the main suite of instruments is nadir-pointed. This pointing constraint, coupled with the sunshade-to-Sun pointing constraint, forces the spacecraft-to-Earth vector to lie outside of the fanbeam and phased-array antenna patterns. Therefore, during these periods, any tracking and RS data must be gathered through the use of the more omni-directional LGAs. This configuration significantly lowers the signal-to-noise ratio for tracking measurements. Two large sources of error on the Doppler tracking measurements include the solar plasma effect and the thermal noise effect. In order for the Doppler tracking data to be useful for Mercury gravitational field mapping, the instrumental accuracy of the Doppler measurements is generally required to be better than *0.1 mm/s* over the integration time of the measurement, which effectively vary from *10 s* to several minutes. The raw Doppler measurements are recorded at the DSN's Central Data Recorder (CDR) at *10* samples per second. During post-processing, the integration time is selected. The longer the integration time, the more accurate the measurement; however, with longer integration times, the measurement has less spatial precision (e.g., during measurements taken at

periherm, the spacecraft can move approximately *200 km* during a *60-s* integration). For operations at Mercury, it is desirable to sustain integration times of no more than *30 s*.

The path delay due to interplanetary plasma has a twofold nature: a slowly varying contribution due to the average electron density in the solar wind and the solar corona, which varies essentially with the Sun-Earth-Probe (SEP) angle, and a fluctuating part due to plasma turbulence. The average contribution can be computed from a density model of the solar corona and interplanetary plasma. Several formulas have been proposed, but all of them agree outside the acceleration region of the solar wind. An accurate evaluation of interplanetary plasma noise was carried out by means of the end-to-end error with the observed accuracy of both Rosetta and Cassini Doppler residuals (Iess et al., 2012). The plasma noise is modeled as:

$$y \cong 1.8 \cdot 10^{-14} / \sin^2(SEP) + 6.3 \cdot 10^{-14} \tag{3.1}$$

when $0° \leq SEP \leq 90°$ and data integration time of *60 s*. The above equation has been derived from a fit of Cassini data, at heliocentric distances between *6* and *9* AU. Due to the mid dependence of the Doppler noise on the distance from the Sun, the equations can be applied to missions to the outer solar system, except when the Earth range is small (< 1 AU). For missions to the inner solar system (e.g. MESSENGER), the SEP angle must be replaced by the Sun-Probe-Earth (SPE) angle as follows:

$$\sin(SEP) = \sin(SPE) \cdot D \tag{3.2}$$

where D (measured in AU) is the heliocentric distance of the spacecraft. The error caused by the solar plasma exceeds the *0.1 mm/s* when MESSENGER has SPE angles higher than *40°*, with integration time of 30-60 s (Figure 3.4). This result indicates that the highest-resolution gravity data are obtained when the spacecraft is on the near side of the Sun. The accurate estimation of Mercury's gravity field by means of MESSENGER radio tracking data is feasible when the spacecraft SPE angle is higher than *40°*.

The total noise budget requires, furthermore, the contribution of thermal effect. Srinivasan (2007) showed that, when MESSENGER is on the near side of the Sun, Doppler observations with less than *0.1 mm/s* error are possible on the LGAs for significant portions of time. This result is important because it implies that the gravity field can be mapped even when the spacecraft is in the orientation required by the remote sensing instruments, when the PAAs are unusable. The main source of the signal level change is the orientation of the spacecraft; depending on where the Earth lies in the LGA pattern, the signal power level changes. Data download to ground via the PAA is performed at every orbit, when the spacecraft is far from Mercury.

Because of these constraints, tracking data with reasonable noise when the spacecraft is close to periherm are available only when Mercury is on the near side of the Sun, and only through the LGA. The operation plan called for additional DSN support when the tracking geometry is likely to provide better data quality.

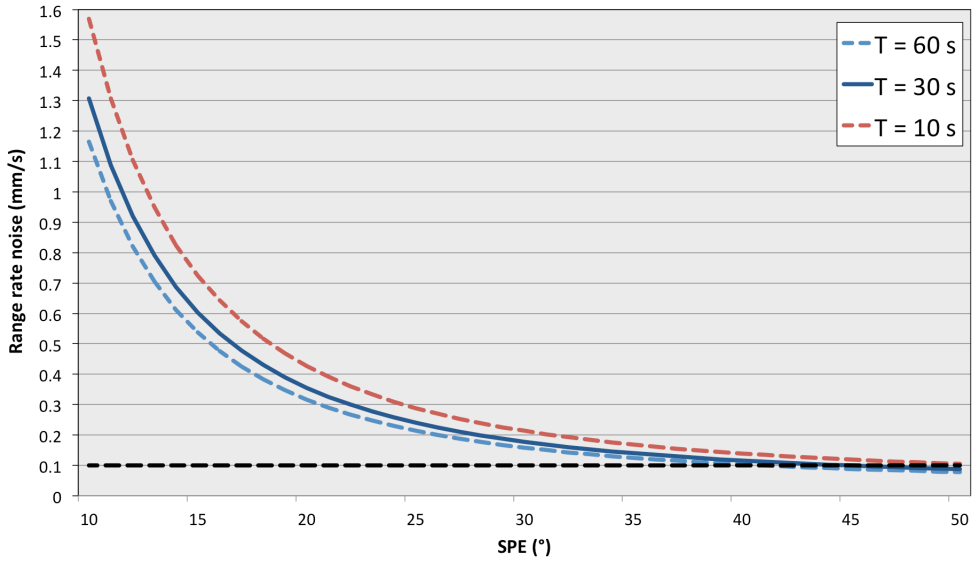

Figure 3.4 Range rate noise due to solar plasma, as a function of the Sun-Probe-Earth angle (Eq. 3.1)

When Mercury is on the far side of the sun (*SPE < 90 deg*) the gravity investigation requires tracking through the fanbeam and PAA during one periherm pass every four days (eight MESSENGER orbits about Mercury). During the first few weeks after orbit insertion, MESSENGER was tracked extensively (*~16h* per day). After this initial period of nearly continuous tracking, the typical coverage (Figure 3.5) was less frequent, limiting the number of direct pericenter passages that were observed (*~8h* per day).

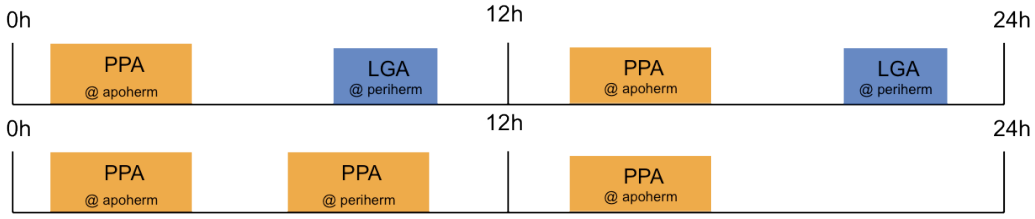

Figure 3.5 A. Tracking passage on the near side of the Sun **B.** Tracking passage on the far side of the Sun

3.2.3 Scientific investigations

The attainable accuracy of MESSENGER state vector depends significantly on the tracking data and the orbital perturbations (which influence the motion of the spacecraft),

among which the Mercury's gravity field and the solar, albedo and infrared radiation pressure are the main sources of error.

The X-band transponder provides range rate and range data between the spacecraft and a DSN ground station and is used in a matrix of observation equations for the spacecraft state that can be solved. To extract the accelerations due to Mercury's gravity, the other forces must be modeled. The quality of the resulting higher order gravity-field coefficients depends directly on the accuracy of the models of these other forces. For Mercury, with little atmosphere and strong solar effects, the most important forces are the solar pressure, the planet reflectance pressure, and the planet's thermal pressure. All these forces rely on the accuracy of the spacecraft surface model, and the planet-based forces further depend on accurate knowledge of Mercury's surface properties.

The spacecraft is modeled as a series of panels, each with area, angle, emission, and absorption properties that must be accurate to better than a few percent. The final spacecraft surface model is calibrated during the gravity-solution process by extensive iterations with the gravity solution.

The altitude of the spacecraft above the surface generally limits the resolution of the gravity field. For MESSENGER, in a *12*-hour eccentric orbit with an inclination of approximately *80°* and minimum pericenter altitude of *200 km* at *60°N* latitude, the resolution varies between about *100 km* to more than *1000 km*. Figure 3.6 shows how that resolution varies with latitude for MESSENGER. The horizontal axis is the Mercury latitude, and the vertical axis is the resolution in degree and order (*l,m*). The approximate block size represented by the degree and order is shown for *l = 75*, *60*, and *30*. The closed-loop appearance of the chart, indicating two resolutions for given latitude, is due to the eccentricity of the orbit and results from the different altitudes of the spacecraft on the ascending and descending parts of the orbit. However, as the planet rotates on its axis, the effective resolution at all longitudes is anticipated to be closer to the higher resolutions. Further, since the closest approach to the planet is in the northern hemisphere, the resolution in the north is at an average block size of about *200 km*, significantly better than that of the south, where the resolution is on the order of *1000 km*. Unfortunately, this limitation restrict the ability to interpret some of the geological features in the south compared with the north.

An orbiting spacecraft is sensitive to the long-wavelength power in the gravitational field, so the low-degree terms in the spherical harmonic expansion of the gravitational potential are well constrained (Kaula, 1966). Of particular interest are degree-two terms, the gravitational flattening C_{20} and the equatorial ellipticity C_{22}. The coefficient C_{22} defines the long-wavelength gravitational shape of the equator and provides a strong constraint on the planetary rotation rate and obliquity. The other phenomenon of interest is the libration, which is a variation in the planetary rotation rate and is manifest as an oscillation of the equatorial shape. The combination of the gravitational flattening, equatorial ellipticity, obliquity, and libration magnitude provide a constraint on Mercury's core state (Peale et al., 2002).

Before MESSENGER's arrival at Mercury, the knowledge of C_{20} and C_{22}, and the mass of Mercury, was based on historical observations of combined data sets from radio tracking of Mariner 10 (Anderson et al., 1987). The first observations of the Mercury's gravity field by MESSENGER were collected during the three Mercury flybys that occurred in January 2008, October 2008, and September 2009. Nevertheless, these flybys provided only brief and low-resolution observations compared with the orbital phase because these data were not able to carry out a reliable solution of Mercury's gravity field lower degrees.

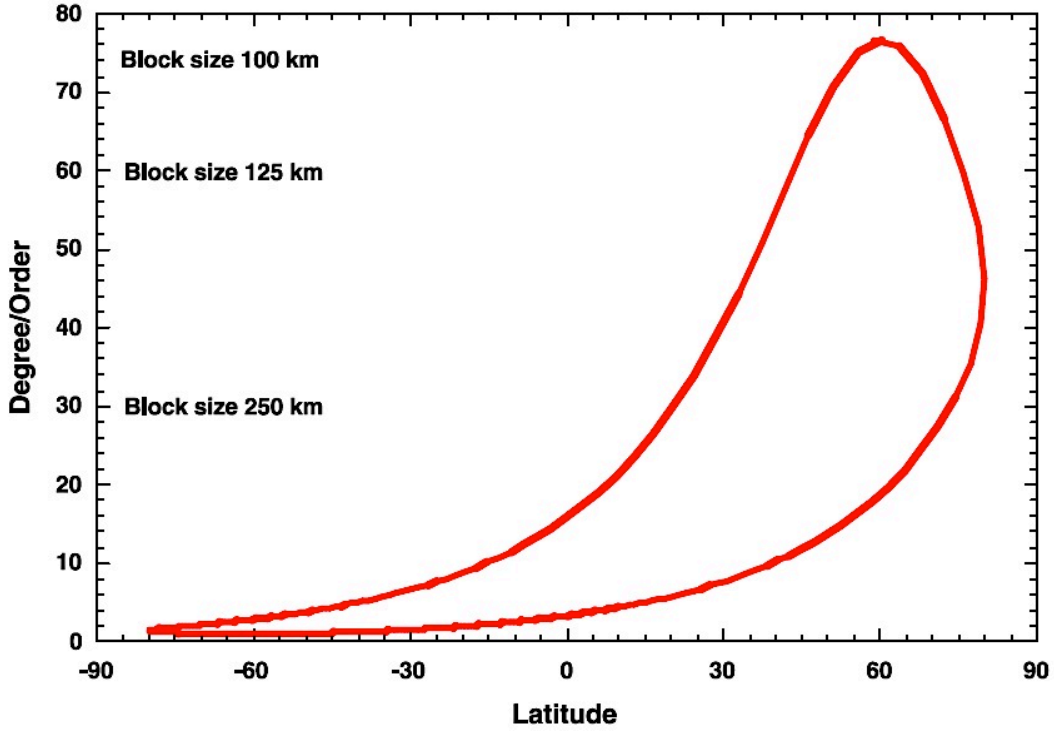

Figure 3.6 Approximate resolution of the Mercury gravity field from the MESSENGER mission (Srinivasan et al., 2007)

During the orbital phase, the spacecraft is occulted from Earth twice on the majority of orbits. If the spacecraft is tracked into occultation or acquired as it emerges from occultation, the time of the occultation can be used to estimate the radius of the planet. DSN open-loop radio science assets are necessary to acquire the RF signal on the egress occultations, as locking to the signal with the normal block-V receiver is not possible for this measurement since there is not an ultra-stable oscillator onboard the spacecraft. Since the spacecraft position can be determined to within 10 m through the precision orbit determination process, it is possible to derive occultation radii to a similar level. Particularly important are occultations that occur in the southern hemisphere where altimeter coverage are lacking. These periods occur several times during the mission

when the spacecraft orbit and Earth are nearly coplanar. These observations are important in constraining the global shape of Mercury and significantly improve knowledge of the planet's offset between center of figure and center of mass (Zuber et al., 2012).

Combining gravity and topography measurements allows an improved estimate of the planet's bulk density. Removing the gravitational attraction of surface topography yield a Bouguer gravity map that shows subsurface density anomalies that can interpreted in terms of crustal thickness, which is indicative of extent of past melting and impact redistribution of crust. Also to be determined are transfer function relationships between gravity and topography, which yields information on crustal thickness that, is indicative of thermal state at the time of surface and subsurface loading. Thus the determination of crustal and lithospheric thickness permits insight into the thermal and geological evolution. Mapping of crustal and lithosphere thickness variations are possible only in the northern hemisphere where high-resolution gravity and topography are obtained (Zuber et al., 2012).

3.3 Radio tracking data analysis

The radio tracking instrumentation provides range and range rate measurements at X-band (7.2-8.4 GHz) necessary for the orbit determination. The data and the paramount information about the spacecraft (attitude quaternions, troposphere and plasma calibration, etc.) had been published in September 2011 for the first six months of the mission[2]. Therefore, we had collected all the tools necessary for the MESSENGER orbit determination that allowed us to set up a realistic mission scenario.

The batch-sequential strategy was developed by means of the Orbit Determination Program (ODP) of the Jet Propulsion Laboratory (JPL) that was used for the radio science experiment on board the Cassini mission. We built a paramount structure of routines around the NASA software obtaining the reported results about the Mercury's gravity field.

The initial guess of these coefficients was set to zero in order to do not influence the solution of the gravity field. The reconstructed model of Mercury's gravity field provides the shape of the geoid that is required for geophysical interpretations. This surface is referenced to the frame defined by the rotational model (Margot, 2009). The center of this reference frame is the barycenter of Mercury that follows the eccentric orbit around the Sun stored in the latest JPL ephemerides DE422[3]. The range observables and ephemeris linear-update allow estimating the Mercury's state vector at the reference epoch (J2000) improving the MESSENGER orbit reconstruction and subsequently the determination of Mercury's gravity field up to degree *20*.

The accuracy of the harmonic coefficients reconstruction depends strongly on the different perturbations that act on the spacecraft, as solar, planetary albedo and infrared

[2] http://pds.nasa.gov/
[3] http://ssd.jpl.nasa.gov/?planet_eph_export

radiation pressures. These important effects are strictly related to the model of the spacecraft. The modeling included a box-wings representation of the MESSENGER probe that approximates the spacecraft as a series of flat plates with specific cross-sectional area and specular and diffusive reflectivity. The plates are oriented in space by means of the spacecraft attitude data (quaternions). The total number of selected components is ten and each plate is characterized by specular and diffusive reflectivity for solar, planetary albedo and infrared radiation pressure. These coefficients are set as solve-for-parameters in order to distinguish the effects of each perturbation. The spacecraft bus is modeled by means of fixed flat plates, which follow the spacecraft attitude, reproducing the real shape of the sunshade and the backside (Figure 3.7). The solar panels are moveable flat plates that vary their orientation maintaining continuously the Sun pointing. The attitude kernels provide the dynamical rotation of the solar panels during the mission. These components have only one degree of freedom, the rotation along X-axis, that we updated continuously in our estimation process to assess their real orientation (Table 3.2).

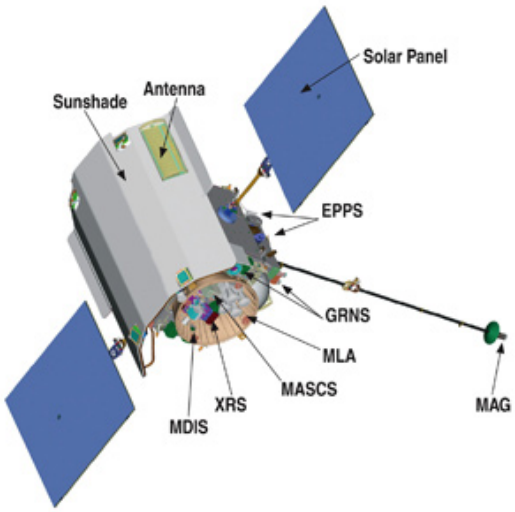

Figure 3.7 MESSENGER spacecraft components (Solomon et al., 2007)

The complexity of this mission scenario leads to adopt an estimation process that allows reducing the modeling errors from the non-conservative forces, which grow quadratically with time. The batch-sequential process fulfills completely these necessities. The main idea of our process is based on a preliminary reconstruction of the spacecraft trajectory that represents the initial guess for a final global fit to determine the gravity field harmonic coefficients. We have processed data, range rate and range, from March 21 through September 2, 2011 excluding an intermediate data gap from June 3 through July 28, 2011 in order to do not consider data with a Sun-Probe-Earth (SPE) angle lower than *40*° and to restart the analysis at about the same longitude on the planet (Figure 3.8). Therefore, the scope of our work was to process a tracking period that spans

two Mercury sidereal days achieving a uniform coverage in longitude. The time span was divided in *12 h* arcs that basically allowed us to analyze each orbit separately.

Component	Area (m^2)	Attitude	Specular reflectivity (S-A-I)	Diffusive reflectivity (S-A-I)
Sun shade right side	2.121	37.2 ° from -Y toward -X	0.04-0.07-0.07	0.24-0.26-0.26
Sun shade central part	1.668	-Y	0.04-0.07-0.07	0.24-0.26-0.26
Sun shade left side	2.121	37.2 ° from -Y toward -X	0.04-0.07-0.07	0.24-0.26-0.26
X side	5.0	+X	0.04-0.07-0.07	0.24-0.26-0.26
Z side	2.2	+Z	0.04-0.07-0.07	0.24-0.26-0.26
Back side	5.046	+Y	0.04-0.07-0.07	0.24-0.26-0.26
Front side of 1st solar panel	2.695	C-kernels[4]	0.28-0.21-0.21	0.06-0.066-0.066
Front side of 2nd solar panel	2.695		0.28-0.21-0.21	0.06-0.066-0.066
Back side of 1st solar panel	2.695		0.04-0.07-0.07	0.24-0.26-0.26
Back side of 2nd solar panel	2.695		0.04-0.07-0.07	0.24-0.26-0.26

Table 3.2 MESSENGER spacecraft model and Solar (S), Albedo (A) and Infrared (I) radiation pressure reflectivities (Vaughan et al., 2002)

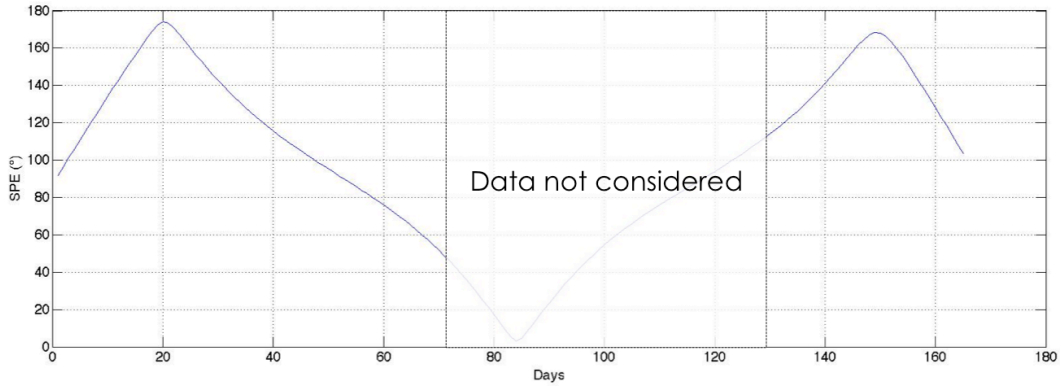

Figure 3.8 MESSENGER Sun-Probe-Angle from March 18, 2011

[4] Attitude kernels (http://naif.jpl.nasa.gov/naif/)

3.3.1 Orbit Determination

The NAVigation (NAV) team at JPL publishes periodically the MESSENGER reconstructed trajectory in the NASA Planetary Data System (PDS)[5] repository. Spacecraft and planetary kernels provide continuously the MESSENGER state vector to the scientific teams of the mission. In September 2011, we downloaded SPICE kernels of the first six months of the mission in order to apply a *single-arc-estimation* process. We partitioned the mission time span in *12 h* arcs considering the reconstructed state vectors in each arc as the reference values. We initialized the dynamical model considering Mercury's *GM* and ephemeris stored in DE422, gravity field harmonic coefficients estimated by Mariner 10 (Anderson et al., 1987) for degree *l=2* and zeros for higher degrees. Non-gravitational forces are solar, albedo and infrared radiation pressures scale factors and spacecraft components reflectivity reported in Table 3.2. The pass through of the first *64* arcs Doppler data shows important signatures in the residuals (Figure 3.9) that reach levels of *800 Hz* in the last arcs.

The trend of range rate residuals, considering the reconstructed trajectory of the navigation team as a priori, highlights how the modeling errors from non-conservative forces lead to important discrepancies in the spacecraft orbit determination. The dynamical model perturbations accumulate significant errors in the spacecraft trajectory reconstruction during the mission. The navigation team avoids the uncontrolled growth of these errors by means of stochastic accelerations that aim to absorb the dynamical perturbations. Nevertheless, the bias in the spacecraft orbit solution increases significantly with time because of non-compensated perturbations. The NAV reconstructed trajectory turns out to be not accurate enough for a combined estimation process. The true and reference state are not close together, therefore, the linearization assumptions are not valid and the multi-arc analysis lead either to poor results or diverge.

Switching to batch-sequential processing, we aimed, therefore, to improve this preliminary trajectory reconstruction with range and range rate measurements. The sequential updates of the dynamical model allow determining the gravitational and non-conservative perturbations. In the case of spacecraft that orbits about Mercury, the strong radiation pressure must be taken into account in order to determine accurately the spacecraft state vector. The solve-for-parameters in each arc are not only the spacecraft position and velocity vectors but also the Mercury's gravity field coefficients up to degree *20*, the solar radiation, planetary albedo and infrared pressure scale factors, and diffusive and specular reflectivity for each spacecraft component. Additional solve-for-parameters are the residual ΔV due to possible orbit control or reaction wheel desaturation maneuvers. In the partial multi-arc fit we estimated therefore these overall for-solve-parameters to improve widely planetary and spacecraft dynamical models. The combined sequential updating of both local and global parameters allows propagating accurately the spacecraft trajectory.

[5] http://pds.nasa.gov/

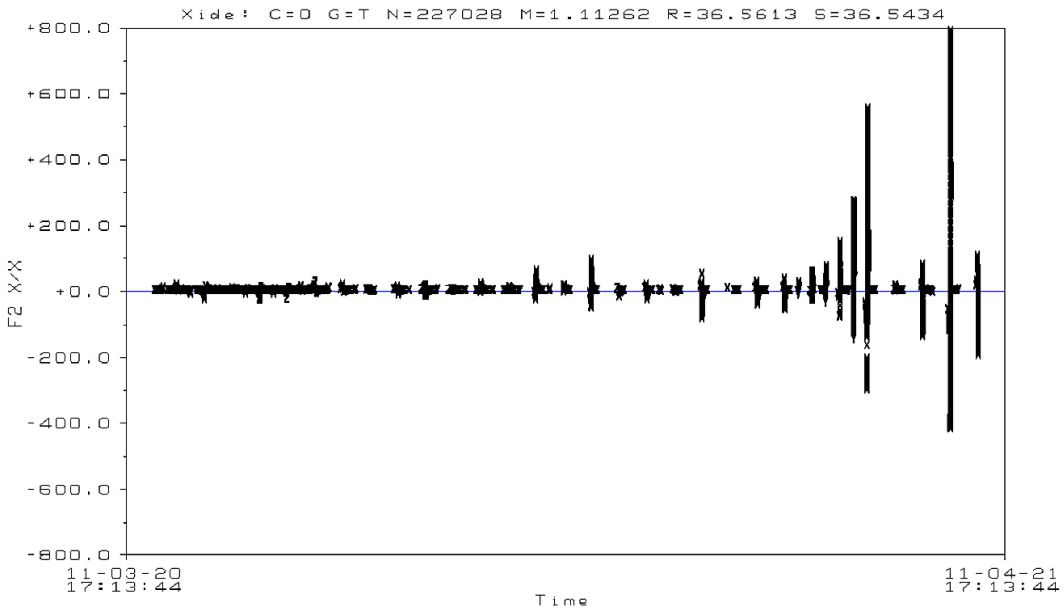

Figure 3.9 Pass-through of Doppler residuals (first 64 arcs) by means of NAV team initial conditions

We introduced four batches of *55* arcs so that each batch spans over half Mercury's sidereal day. In the first arc, the MESSENGER state vector is given by the Spacecraft and Planetary kernel and propagated with its covariance matrix in the following arcs. Sequential updates of the dynamical model, including the gravity field coefficients and the surfaces reflectivity, were obtained at the end of each batch. With this procedure the spacecraft orbit determination for the following arcs is considerably improved.

Figure 3.10 shows the batch-sequential estimation strategy developed for a preliminary reconstruction of the MESSENGER orbit. As the common sequential processing, this filter tends to become insensitive to the observations. To overcome this problem, we multiply the covariance matrix of updated and propagated state to a specific factor (nine considering *3-σ*). The benefits of this recursive process are well-rendered after the first update of Mercury's gravity field coefficients and non-gravitational perturbations in the second batch.

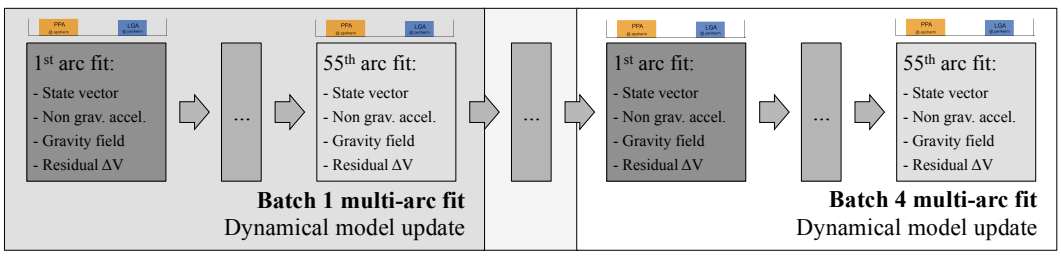

Figure 3.10 Batch-sequential estimation of MESSENGER mission

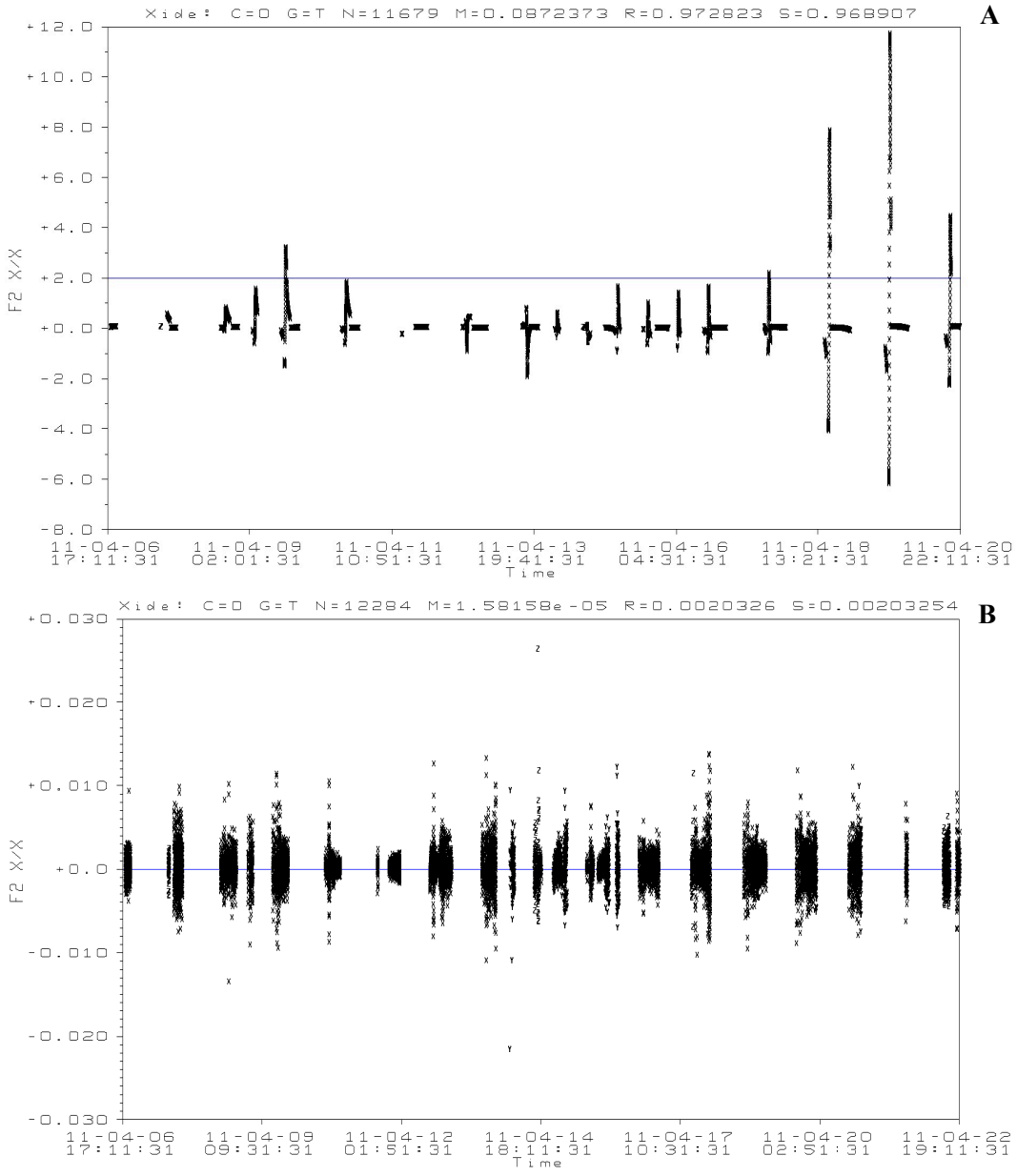

Figure 3.11 A. Pass-through Doppler residuals of the second batch **B.** Multi-arc fit of the second batch

In Figure 3.11-A we reported on the pass-through of the Doppler residuals of the second batch. The time span corresponds to the second part of the data showed in Fig. 3.9, where the NAV reconstructed trajectory defines the initial conditions of the state vector. The batch-sequential filter highlights significant improvements in the spacecraft orbit determination showing range rate residuals reduced of a factor *80*. Moreover, these data are processed in a partial multi-arc fit (Figure 3.11-B) so that Mercury's gravity field

and non–gravitational perturbations are updated in the following arcs. The recursive process applied to all four batches leads to a consistent reconstruction of the trajectory that represents the initial guess in a final global fit needed to carry out a combined solution of the global parameters. The sequential updates of the dynamical model give important information about the perturbations that act on the spacecraft but not provide unique solution of Mercury's gravity field and spacecraft model.

The batch-sequential processing provides the reconstructed spacecraft orbit that is statistically consistent with that available on the Planetary Data System repository. The differences of the position vector components between the two reconstructions (expressed in the orbital frame) are plotted in Fig. 3.12. In our solution, the position uncertainty in the $\boldsymbol{H}\times\boldsymbol{R}$ component on day *66*, when the discrepancy is maximum, is about *600 m*. The difference is therefore about *3-σ*. Not surprisingly, the radial component is much better determined.

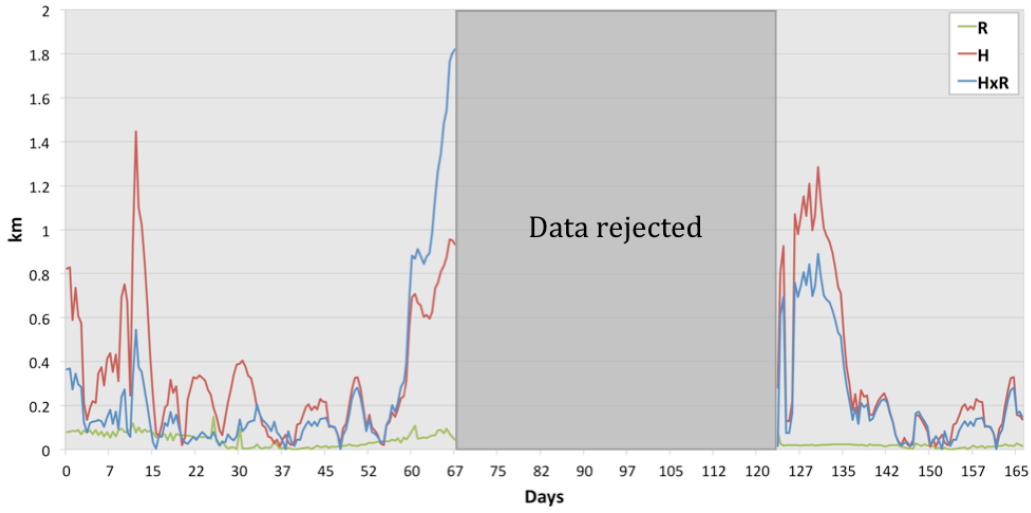

Figure 3.12 Differences between navigation and our orbit reconstruction in the three orbital components: radial $\boldsymbol{R}$ (green), out of plane $\boldsymbol{H}$ (red) and $\boldsymbol{H}\times\boldsymbol{R}$ (blue).

The preliminary reconstructed trajectory initialized a final global fit that allowed us to carry out a combined solution of the dynamical model. Although the initial conditions of the spacecraft state vector are the estimated values of the batch-sequential estimation process, the global parameters are redefined in order to not constraint the solution. We set therefore the spacecraft model as in Table 3.2, Mercury's *GM* and trajectory as in the JPL ephemerides DE422 and Mercury's gravity field coefficients equal to zero. Moreover, we did not use any a priori uncertainty for these solve-for-parameters expect that higher gravity field harmonic degrees than $l=7$ and spacecraft components reflectivity.

The final global fit led us to good results of Mercury's gravity field coefficients and planetary trajectory. The update of Mercury's ephemeris required range data provided by

different DSN stations. We considered the range bias as local solve-for-parameters taking into account possible errors in the range measurements that rely on different tracking pass. Figure 3.13 shows the trend of range bias with different DSN stations during the mission period analyzed in our process. These parameters are fully consistent with the range error budget providing the maximum value of about *30 m* and a periodic trend during the mission data analysis.

Multi-arc analysis	
Local parameters: • Spacecraft position • Spacecraft velocity • Residual ΔV (DSM - OCM) • Range bias	*Global* parameters: • *GM* and gravity field up to degree 20 • Solar, albedo and infrared radiation pressure scale factors • Mercury position and velocity

Table 3.3 Solve-for-parameters of the final multi-arc estimation

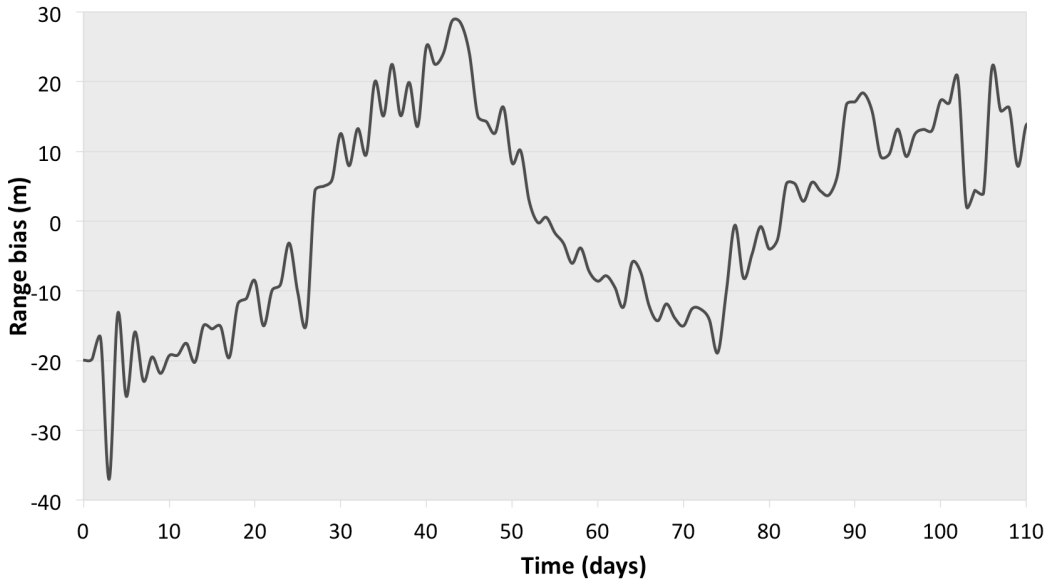

Figure 3.13 Range bias trend during the mission

The iterated process reached a stable solution that provided us a model of Mercury's gravity field and ephemeris. The residuals of range and range rate data (Figure 3.14) at the end of the final global fit show a good level of noise respectively at about *1.9 m* and *3.6 mHz* (*~0.1 mm/s*). The Doppler data processed in the filter have an integration time of *30 s* because of the intrinsic numerical noise of the ODP. The data residuals highlight the

consistency of our solution. The noise shows distinctly the dependence from the SPE angle in particular for range data, with low noise in the inferior solar conjunction.

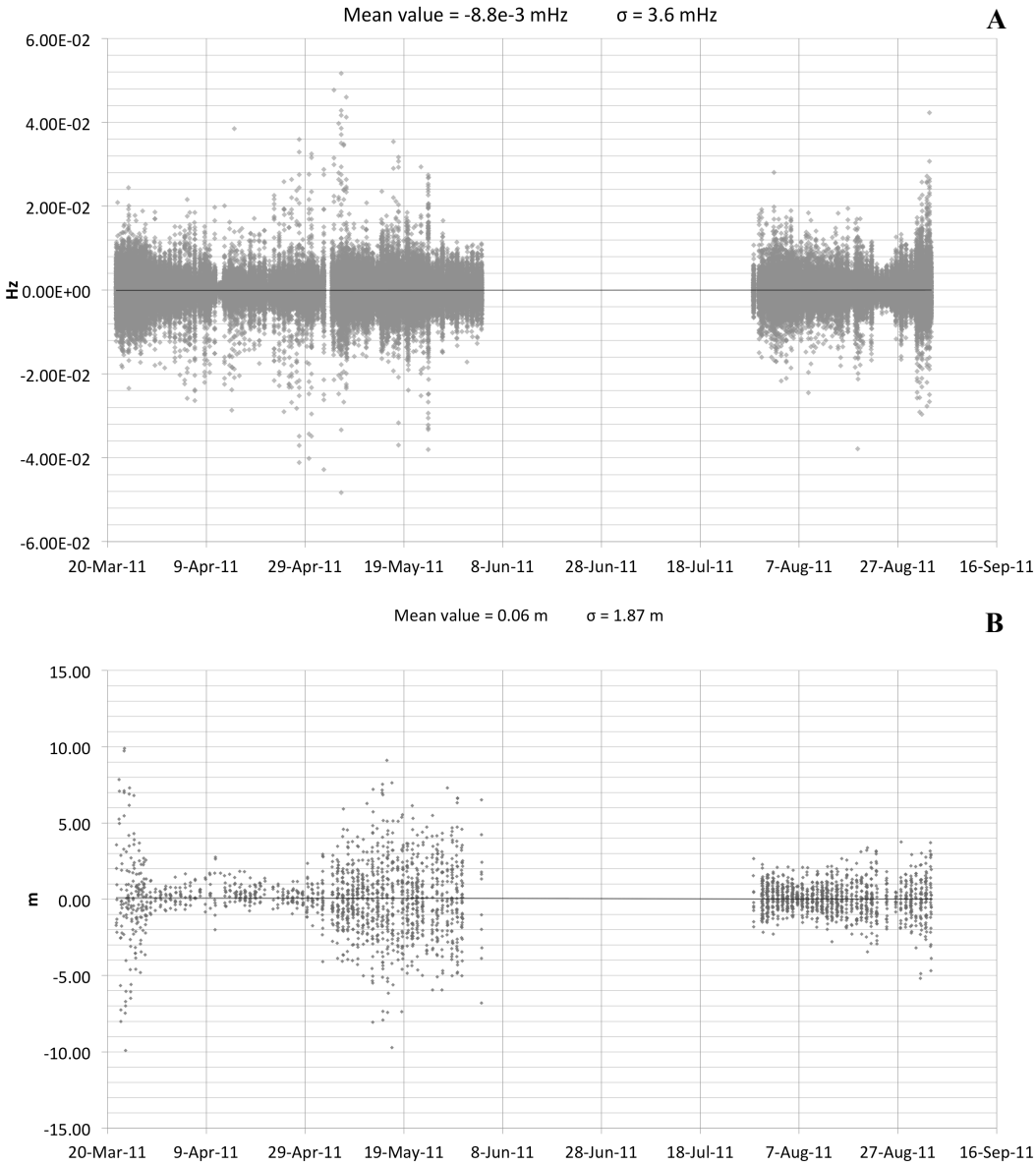

Figure 3.14 A. Doppler residuals of final global fit **B.** Range residuals of final global fit

3.3.2 Mercury's gravity field

The analysis of the MESSENGER radio tracking data provided us a model of Mercury's gravity field. The combined estimation of *110* days of the mission allowed us

to recover the Mercury's gravity field coefficients focusing on the zonal harmonics. One of the main motivations of our work was the need to assess BepiColombo MPO orbit evolution, as it is known that zonal harmonics cause large secular effects on the Keplerian elements. We have therefore propagated the MPO orbit and the associated state covariance matrix (presented in *Section 5.3*) using the gravity field and the associated covariance matrix obtained from the analysis of MESSENGER data.

An unbiased propagation of the spacecraft state and state covariance requires that the estimate of the gravity field coefficients is carried out with only a minimum set of a priori constraints. This is especially important for the low degree zonal harmonics, which are causing most of the change in the orbital parameters. On the other hand, given the geometry of the orbit, the available data set and the large number of the parameters that may need to be estimated, some constraints need to be imposed in order to avoid a runaway of the solution. In a widely used approach for terrestrial planets and the Moon, the a priori covariance of the gravity harmonics is inferred from a Kaula's rule. However, a covariance analysis shows that the estimate of the harmonic coefficients up to $l=7$ can be carried out without the need of a priori information. Therefore, in the combined arcs solution only the $l>7$ harmonics were constrained using a Kaula power law, while no constraints were used in the estimate of the low degree harmonics.

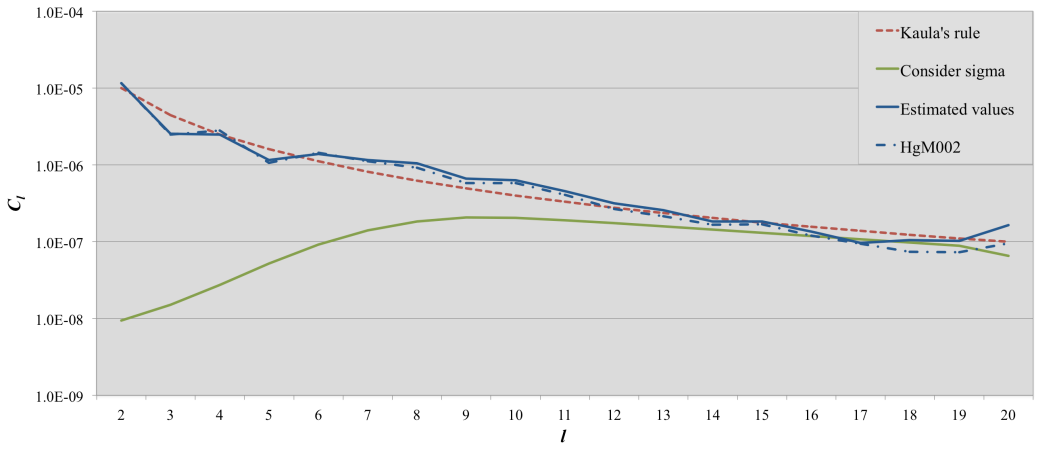

Figure 3.15 RMS power in harmonics of degree l, as estimated from the batch-sequential filter applied to the first 110 days of MESSENGER data, and in HgM002

The batch-sequential estimation filter has estimated the Hermean gravity field reported in Fig. 3.15. The power in the gravitational field, expressed as root mean square (RMS) power given by:

$$C_l^2 = \frac{1}{(2l+1)} \sum_{m=0}^{l} \left(C_{lm}^2 + S_{lm}^2\right) \tag{3.3}$$

shows the consistency between the HgM002 and our solution. Although we did not constraint the field up to $l=7$, the two gravity models essentially agree. To limit the power of the high-degree coefficients because of noise in areas that lack low-altitude coverage, a priori uncertainties were applied to coefficients for spherical harmonic coefficients of degree $l>7$. The a priori uncertainty of each coefficient of the same degree has been set by the Kaula's rule $4\times10^{-5}/l^2$. The graph shows the proximity of the formal uncertainties (green line) to the estimated values (blue line) for degree greater than $l=11$. The lower degree harmonics are determined with a small relative uncertainty.

Parameter	Value	Uncertainties*	Comments
GM (km^3s^{-2})	22032.0840	0.1021	No significant change from Mercury's ephemeris in DE422
$C_{20} \times 10^{-6}$	-22.5757	0.0889	
$C_{21} \times 10^{-6}$	-0.0662	0.0769	
$C_{22} \times 10^{-6}$	12.5184	0.1037	Consistent with HgM002 solution
$S_{21} \times 10^{-6}$	-0.1064	0.0963	
$S_{22} \times 10^{-6}$	-0.0001	0.1032	
$C_{30} \times 10^{-6}$	-4.8107	0.1554	
$C_{40} \times 10^{-6}$	-5.6584	0.3456	Good correlation between zonal harmonics entails different possible consistent solutions
$C_{50} \times 10^{-6}$	0.0561	0.7238	
$C_{60} \times 10^{-6}$	1.9517	1.3287	
$C_{70} \times 10^{-6}$	-0.8239	2.0453	

* Formal uncertainties (10-σ) of the global fit

Table 3.4 Normalized gravity field coefficients[6]

In Table 3.4 we reported on all gravity field coefficients for degree $l=2$ and the zonal harmonics for degree up to $l=7$. The harmonic coefficients C_{20} and C_{22} are estimated with relative uncertainties of about 0.1%, showing remarkable consistency with the HgM002 solution (Smith et al., 2012). The other coefficients of degree 2 are so small that the formal uncertainties justify the alignment of the angular momentum with the adopted rotation axis and the alignment of the equatorial major axis of the gravity field with Mercury's "hot-pole" longitudes, which correspond to subsolar points when Mercury is at the perihelion.

The degree 2 harmonic coefficients are used to determine the reference ellipsoid, which represents the equipotential surface of an isolated planetary body under the action of three different fields: gravity quadrupole terms, rotational (centrifugal) field and tidal

[6] The remaining coefficients of Mercury's gravity field 20 x 20 are provided in http://radioscience.dima.uniroma1.it/material.php?id=66

field from the Sun. Figure 3.16 shows the reference ellipsoid polar and maximum equatorial axes respectively of about *2439.58* and *2439.82 km*.

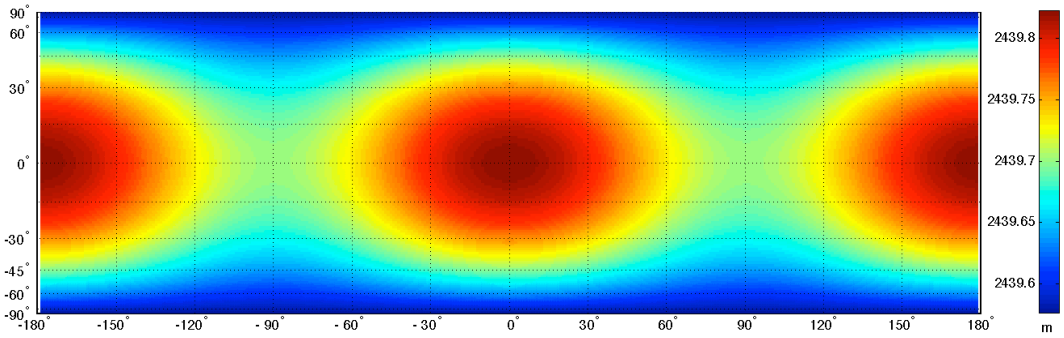

Figure 3.16 Mercury's reference ellipsoid

The difference between the zonal harmonics of degree *3* and *4* of our solution and HgM002 is within the best estimate uncertainty reported in (Smith et al., 2012). The two analyses lead to consistent results highlighting, however, the need to give adequate latitude to the uncertainties of the zonal harmonic coefficients of degree *l>2*. Although the differences in the C_{30} and C_{40} in the two solutions do not affect the interpretation of the gravity anomalies in the northern hemisphere (*Section 5.1*), the combined estimation of these two parameters is in demand for accurate MPO orbit prediction (*Section 5.3*).

3.3.3 Mercury's ephemeris update

The inclusion of range data in the global fit allowed us to update Mercury's ephemeris. In Table 3.5 we reported on the ephemeris correction with respect to the DE422 where the orbital parameters are referred to the reference epoch J2000.

Δa (m)	Δe	Δi (°)	ΔΩ (°)	Δω (°)
-13	-1×10^{-9}	-1×10^{-6}	1×10^{-5}	-1×10^{-5}

Table 3.5 Ephemeris correction respect to DE422

The corrections are very small, with changes in the semi-major axis and the eccentricity respectively of *13 m* and 1×10^{-9}. The latest ephemerides DE422 also include Mercury's mass, corresponding to $GM = 22032.09\ km^3/s^2$ (the first guess value in our estimation process). Although no constraint was applied to Mercury's *GM*, surprisingly the estimated value shows a correction of just $1 \times 10^{-2}\ km^3/s^2$ over DE422.

Chapter 4

BepiColombo

Outline. BepiColombo is a joint mission of the European Space Agency (ESA) and the Japan Aerospace and eXploration Agency (JAXA) to the planet Mercury, due to launch in 2015. The mission is still in the planning stages and involves two separate orbiters: the Mercury Planetary Orbiter (MPO) with eleven instruments for planet remote sensing and the Mercury Magnetospheric Orbiter (MMO) with five instruments for magnetosphere investigations. One of the eleven sophisticated instrumentations on board the MPO is dedicated to radio science allowing highly stable, multi-frequency radio links in X and Ka band. Precise range and range rate measurements will be attainable with accuracies of about respectively *20 cm* and *0.003 mm/s*. The high performances of the tracking system lead to challenging requirements on the spacecraft orbit reconstruction to a level of meters. Precise trajectory reconstruction allows estimating Mercury's gravity field with high accuracy up to degree *25*, providing crucial information on the interior structure of the planet.
A full numerical simulation of the Radio Science Experiment has been carried out, taking into account the development in the new spacecraft design, the mission profile and the tracking system. The results of these numerical simulations aim at a realistic assessment of the attainable accuracies in the determination of Mercury's gravity field.

4.1 Mission overview

Mercury plays a fundamental role in constraining and testing the competing theories explaining dynamical and compositional aspects of the formation and evolution of the terrestrial planets. In addition to its paramount importance for planetary science, Mercury has since long ago raised the interest of the fundamental physics community. Indeed, Mercury's proximity to the Sun entails significant relativistic effects, providing therefore unique possibilities for testing Einstein's theory of general relativity and alternative theories of gravity. Nevertheless, this proximity to the Sun has always entailed numerous

difficulties in the mission design for the exploration of the planet Mercury. The solar flux at Mercury, about $1.69 \times 10^7\ erg\ cm^{-2}\ s^{-1}$ (Lewis, 2004), determines unfavorable thermal environment for spacecraft dedicated to the investigation of the planet. BepiColombo was designed to endure temperatures in excess of $350°\ C$ and gather data during its *1* year nominal mission, with a possible *1*-year extension. The main objective of the mission is a comprehensive investigation of Mercury, which has always represented a demanding target to be reached by a spacecraft. BepiColombo will be the first European mission to Mercury. The design foresees two separate spacecraft: the Mercury Planetary Orbiter (MPO) equipped by eleven instruments devoted to the remote sensing of the planet's surface and the investigation of its interior structure, and the Mercury Magnetospheric Orbiter (MMO), led by the Japan Aerospace eXploration Agency (JAXA), dedicated to a comprehensive study of the planet's exosphere and magnetosphere, and their interaction processes with the solar wind and the planet (Schulz and Benkhoff, 2006).

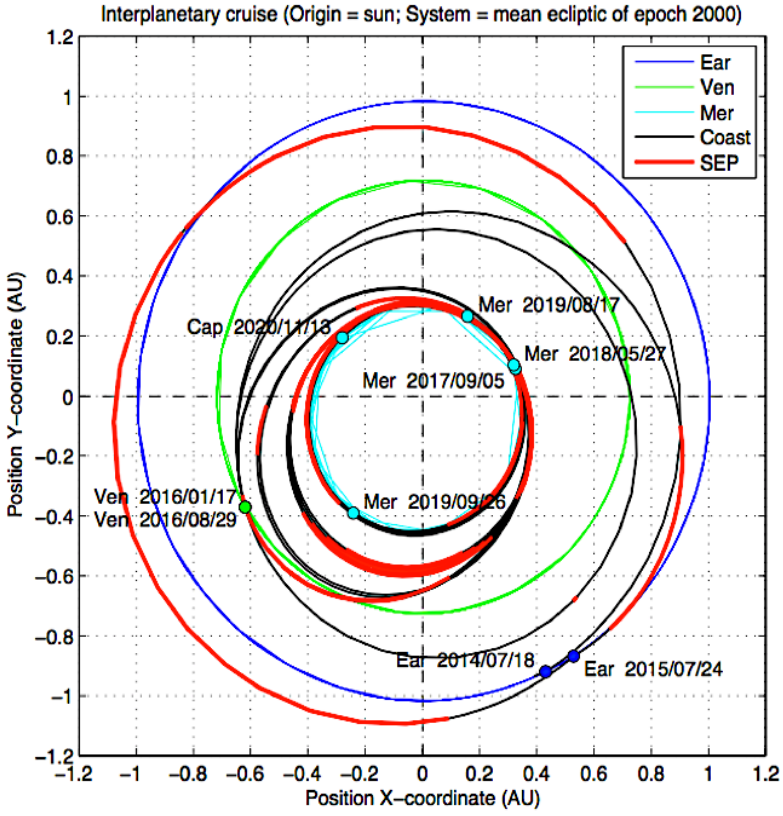

Figure 4.1 BepiColombo interplanetary transfer orbit (Garcia et al., 2010)

BepiColombo is endowed with a solar electric propulsion (SEP) system. The interplanetary cruise phase exploits a combination of low-thrust arcs and flybys at Earth, Venus and Mercury itself to reach the planet with low relative velocity (Figure 4.1). The

mission scenario entails launch by an Ariane 5 (nominally on August 2015) of a spacecraft composite. The lift off mass will be 4.2 metric tons (including a launch vehicle adapter), of which a large fraction (about *32%*) is propellant. The duration of the cruise phase will be about seven years for a planned arrival at Mercury in the beginning of 2022.

For launch and the journey to Mercury, the MPO and the MMO will be carried as part of the Mercury Composite Spacecraft (MCS). The MCS comprises, in addition to the two orbiters, the Mercury Transfer Module (MTM), which provides solar-electric propulsion and all services not required in Mercury orbit and the MMO Sunshield and Interface Structure (MOSIF), which provides thermal protection and the mechanical and electrical interfaces for the MMO (Figure 4.2).

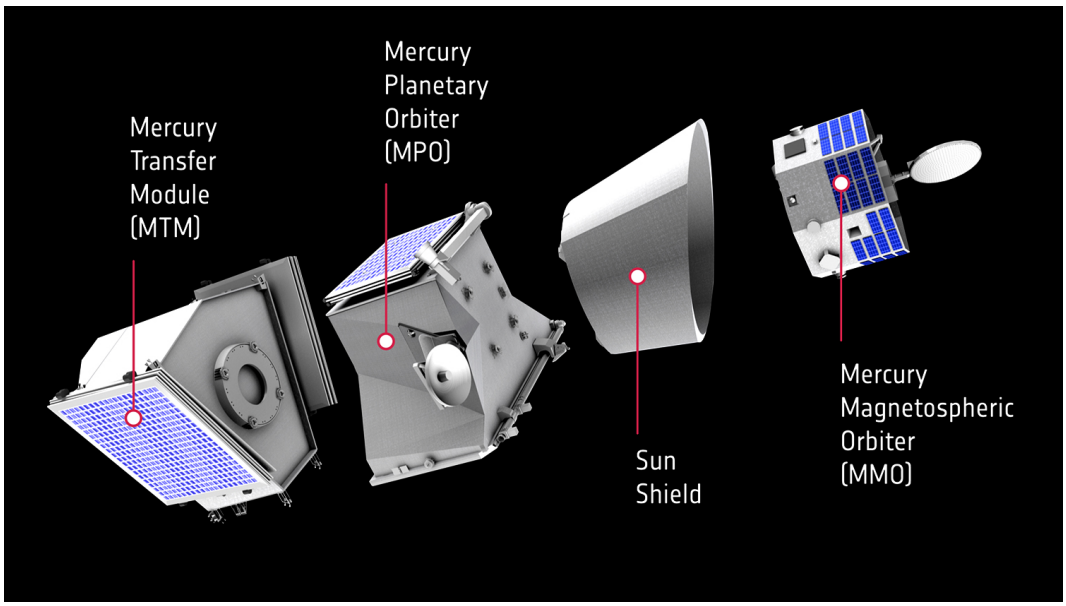

Figure 4.2 Elements of Mercury Composite Spacecraft[1]

The heliocentric low-thrust arcs reduce the approach velocity at Mercury arrival to low values such that, when the spacecraft passes the Sun-Mercury Lagrange L_1 and L_2, it is weakly captured in a highly eccentric orbit around Mercury. After the approach through a weak stability boundary of the planet, the spacecraft requires only a small velocity change for a firm capture. An additional thrust phase will insert the MMO into its operational orbit and the MPO into its lower orbit (Figure 4.3). The spacecraft orbits are polar with different eccentricities and same pericenter altitudes (Table 4.1).

The BepiColombo mission will provide a rare opportunity to collect multi-point measurements in a planetary environment. The current orbits tend to provide a *1:4* synchronization in orbital periods and then the two spacecraft will have a few close encounters (a few *100 km* or less) during the first month of the mission in orbit after

[1] http://sci.esa.int/

which the shortest encounter will increase up to several *1000 km*. Therefore, it is foreseen to avoid an exact *1:4* synchronization of the MPO and MMO orbit to allow close encounters of the two spacecraft throughout the mission. Such intervals are very important for the inter-calibration of similar instruments on the two spacecraft. They also provide very scientifically valuable intervals to collect multi-point measurements in an environment where both spatial and temporal scales can be very short (Benkhoff et al., 2010).

	h_a (km)	a (km)	e	i (°)	Ω (°)	ω (°)	T (h)
MPO	400	3394	0.163229	90.0	67.7	16.0	2.325
MMO	400	8552	0.667914	90.0	67.7	-2.0	9.3

Table 4.1 Initial orbital elements of MPO and MMO in the Mercury equatorial system (Garcia et al., 2010)

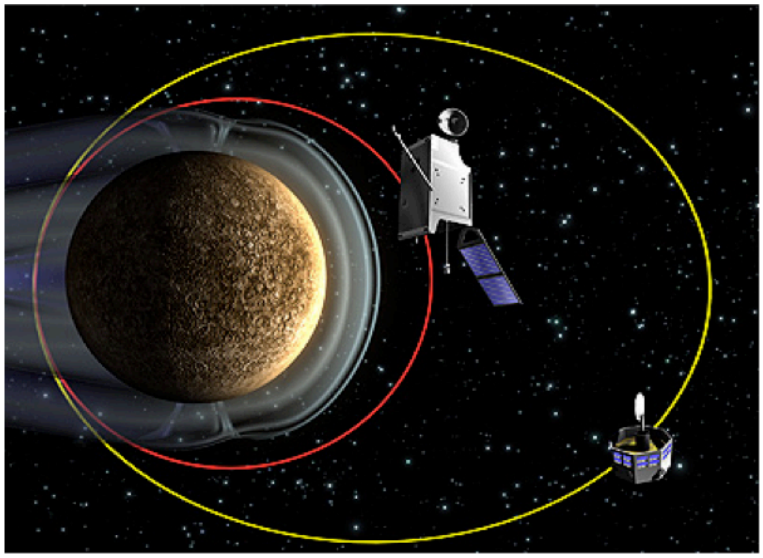

Figure 4.3 Mercury Planetary Orbiter and Mercury Magnetospheric Orbiter orbital configuration[2]

4.1.1 Mercury Planetary Orbiter

The Mercury Planetary Orbiter is a three-axis-stabilized and nadir-pointing spacecraft focused on a full coverage remote sensing. The low-eccentricity polar orbit allows excellent spatial resolution over the entire planet surface entailing, however, substantial thermal loads on the spacecraft during the orbital phase. The spacecraft structure uses a double-H configuration with a single radiator plane. Heat coming from the Sun and

[2] http://sci.esa.int/

Mercury and generated by spacecraft subsystems and payload components is carried to the radiator by panel-embedded heat pipes. The structural design provides free access to all equipment and instruments during the Assembly, Integration and Test (AIT) program. The design is mass efficient, with the primary structure serving as the mounting surface for all equipment; it will remain permanently assembled during AIT, avoiding the need for connector brackets and preventing alignment disturbances. MPO has four-point bolted interfaces to both the MTM and the MOSIF.

The configuration and thermal design provide a classical thermal environment for internally mounted instrument equipment while employing dedicated high temperature technologies for external items such as antennas, the solar array, the sun sensors and Multi-Layer Insulation (MLI), which are exposed to the harsh thermal environment around Mercury.

The solar array is a single-sided design, which uses Optical Solar Reflectors (OSRs) for temperature control. The solar array requires continuous rotation keeping the Sun at a low incidence angle in order to generate adequate power while at the same time limiting the temperature. The three-panel array has its rotation axis in an optimized direction minimizing the occurrences, during the Mercury year, of alignment between the Sun vector and the rotational axis of the solar array. During the full science operations phases, the solar array will provide up to *1000 W* of the electrical power. The MPO is also equipped with the battery that will supply electrical energy to the spacecraft allowing the scientific operations during both the natural and artificial eclipses.

The principal Attitude and Orbit Control Subsystem (AOCS) on the MPO consists of:

- three Star Trackers (STRs), each comprising a star tracker unit housing the optics and electronics, a shutter – which can be closed in the event of a major attitude control anomaly – and a baffle;

- two Inertial Measurement Units (IMU), including four high-accuracy rate-integrating gyros and four accelerometers in a tetrahedral configuration, together with the processing electronics;

- two redundant sets of two Fine Sun sensors;

- four reaction wheel assemblies, controlled by two sets of wheel drive electronics;

- two redundant sets of four *22-Newton* hydrazine MON-3 (Mixed Oxides of Nitrogen, a mixture of nitrogen tetroxide and *3%* of nitric oxide) thrusters to provide the change in velocity (ΔV) needed for orbit capture and orbit lowering to the MMO and MPO operational orbits;

- two redundant sets of four *10-Newton* monopropellant (hydrazine) thrusters for attitude control and reaction wheel momentum off-loading.

The reaction wheels are mounted in a tetrahedral configuration; attitude control can be achieved with four wheels operating simultaneously (the nominal operational scenario) or any combination of three wheels.

During science operations, at least two STRs will be used in combination. In the event of major system anomaly on the spacecraft and consequent loss of attitude control, dedicated shutters will protect the STR optical paths to prevent damage due to accidental Sun pointing.

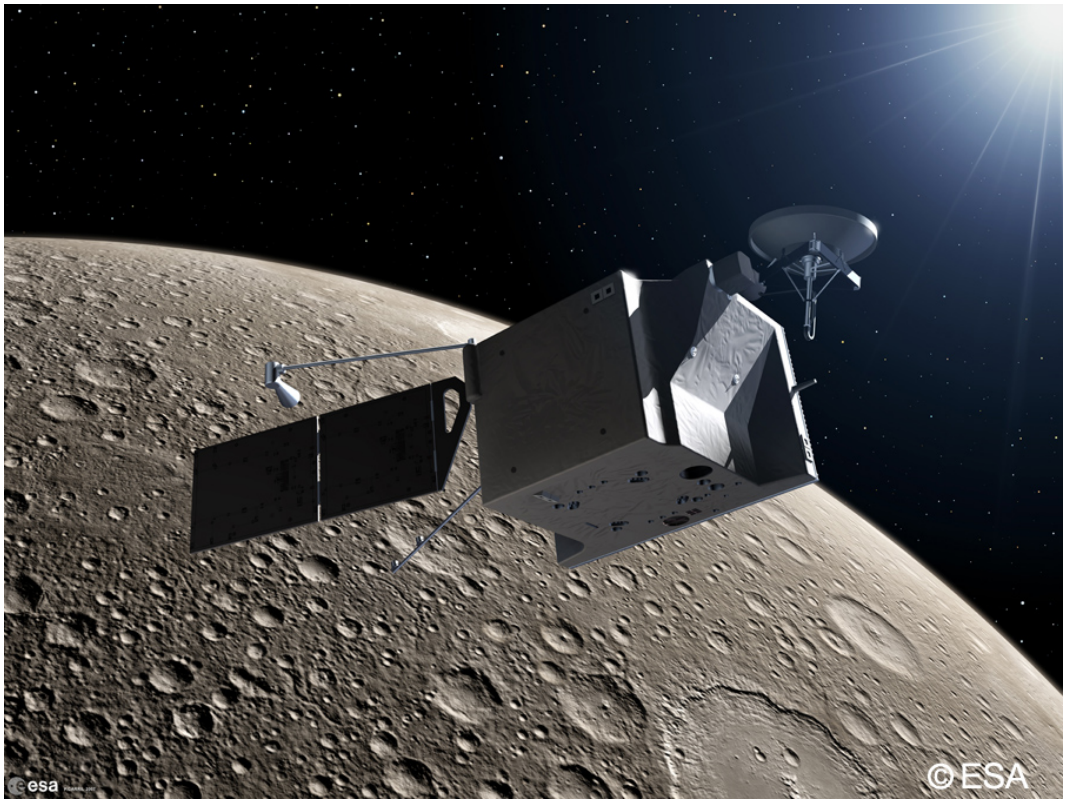

Figure 4.4 Mercury Planetary Orbiter[3]

This sophisticated orbit control system was designed taking into account the requirements of the scientific instruments on board the spacecraft. In November 2004, the ESA Science Programme Committee has officially approved the selection of the MPO scientific payload. The instruments on board the spacecraft are *16* combined in several cases to instrument packages (Table 4.2) sharing common subsystem. The MPO is focused on the investigation of Mercury's interior, surface and exosphere and support the MMO in the detailed characterization of the magnetosphere and its relation to the exosphere and the planet.

[3] http://sci.esa.int/

Instrument	Measurements
BEpiColombo Laser Altimeter **(BELA)**	Topographic mapping
Italian Spring Accelerometer **(ISA)**	Non-gravitational accelerations of the spacecraft
Magnetic Field Investigation **(MERMAG)**	Detailed description of planetary magnetic field, its source and interaction with the solar wind
Mercury Thermal Imaging Spectrometer **(MERTIS-TIS)**	Global mineralogical mapping (*7–14 μm*), surface temperatures and thermal inertia
Mercury Gamma-ray and Neutron Spectrometer **(MGNS)**	Elemental surface and sub-surface composition, volatile deposits on polar areas
Mercury Imaging X-ray Spectrometer **(MIXS)**	Elemental surface composition, global mapping and composition of surface features
Mercury Orbiter Radio science Experiment **(MORE)**	Core and mantle structure, Mercury orbit, fundamental science, gravity field
Probing of Hermean Exosphere by Ultraviolet Spectroscopy **(PHEBUS)**	UV spectral mapping of the exosphere
Search for Exospheric Refilling and Emitted Natural Abundances **(SERENA)**	In situ study of composition, vertical structure and source and sink processes of the exosphere
Solar Intensity X-ray and particle Spectrometer **(SYXS)**	Monitor solar X-ray intensity and solar particles in support of MIXS
Spectrometers and Imagers for MPO BepiColombo Integrated Observatory System **(SIMBIO-SYS)**	Optical high resolution and stereo imaging, Near-IR (*<2.0 μm*) imaging spectroscopy for global mineralogical mapping

Table 4.2 MPO scientific payload (Schulz and Benkhoff, 2006)

The two cameras of the Spectrometers and Imagers for MPO BepiColombo Integrated Observatory System (SIMBIO-SYS) will provide a global mapping of the surface morphology with a spatial scale of *100 m*, with possible spatial resolutions up to *5 m* for specific areas of interest. The near- and thermal infrared spectrometers will determine the global mineralogical surface composition with a spatial resolution of *500 m*, comparable to the regolith mixing length.

Furthermore, the Mercury Imaging X-rays Spectrometer (MIXS) will carry out a global mapping of the elemental surface composition at a scale of about *50 km*, reaching high spatial resolution up to *500 m* during higher solar activity. The combined analysis of these measurements will lead to morphological and compositional characterization of individual surface features, identifying whether specific landmarks have been produced by endogenic (volcanism) or exogenic processes (impacting objects). Knowledge of Mercury's surface composition will provide important results about competing models for the formation and evolution of Mercury. Additional measurements, provided by the Mercury Gamma-ray and Neutron Spectrometer (MGNS), will also detect the sub-surface elemental composition and the origin of radar-bright spots, observed in the polar region (Schulz and Benkhoff, 2006).

Mercury's interior structure represents the main issue of the Mercury Radio science Experiment (MORE) in cooperation with the Italian Spring Accelerometer (ISA), the BEpiColombo Laser Altimeter (BELA) and the high-resolution camera. The radio tracking data, supported by the accelerometer readings, will allow determining accurately not only the Mercury's gravity field but also its rotation state (obliquity of the pole and amplitude of physical librations), which will be also provided by the pattern matching of the high-resolution images. The reconstructed gravity and rotational model will lead to determine whether or not Mercury has a molten core. Moreover, the laser-altimeter data combined with the gravity anomalies will provide important information about the structure of Mercury's mantle.

4.1.2 Mercury Magnetospheric Orbiter

The Mercury Magnetospheric Orbiter is an electromagnetically very clean spin-stabilized spacecraft focusing on the investigation of fields, waves and particles in the environment of Mercury. The spin axis of the spacecraft is nearly perpendicular to the equator. The MMO will be placed into an elliptical polar orbit of high eccentricity with the major axis in the equatorial plane. This will render a global exploration of the magnetosphere up to a distance of nearly *6* planetary radii from the planet's center (Yamakawa et al., 2004).

The main scientific goal of the MMO is the determination of the structure and dynamics of Mercury's magnetosphere. The scientific payload, selected to investigate the Mercury's magnetic environment, consists of *3* instruments and *2* instrument packages (Table 4.3). The observations will provide necessary information to characterize the structure and dynamics, as well as the physical processes of the magnetosphere and its interaction with the solar wind. The Mercury Plasma Particle Experiment has the capability to measure charged particles in a wide energy range as well as energetic neutral atoms. The Plasma Wave Investigation package will determine key parameters of the magnetospheric plasma, such as density, temperature, boundary layers, transport processes and wave propagation and coupling with the solar wind and the exosphere. The magnetometer will provide a complete description of the magnetic field and its spatial

and temporal variations. In combination with the magnetometer on the MPO, it will enable the separation of the contributions from the magnetosphere and the planetary magnetic field. The measurement of energetic neutral atoms will also result in information about Mercury's exosphere. In addition, the Sodium Atmosphere Spectral Imager will provide insight into the regolith–exosphere–magnetosphere coupling of exospheric sodium and the Mercury Dust Monitor will measure the interplanetary dust environment around Mercury (Schulz and Benkhoff, 2006).

The instruments are allocated in the MMO primary structure, an octagonal prism with 1.8 meters between opposing faces and an overall height of *0.9 meters*. The total mass of the spacecraft is estimated to be around *275 kg*, which include *45 kg* of instruments. A circular central core carries the separation interface at one end and supports the pylon for the high-gain antenna at the other. The 'top' and 'bottom' panels are recessed within the octagonal outer body; instruments and spacecraft subsystems mounted on the exterior of the top and bottom panels are shielded from the Sun by the walls of the octagon. Each of the eight side panels is fitted with solar cells; the aggregate power generation capacity will be about *350 W*. The area of the panels not covered by solar cells has a mirror finish to reflect solar radiation (Yamakawa et al., 2004).

Instrument	**Measurements**
Mercury Magnetometer **(MERMAG-M/MGF)**	Detailed description of the magnetosphere and relation and interaction with solar wind and planetary magnetic field
Mercury Plasma Particle Experiment **(MPPE)**	Study of low and high energetic particles in the magnetosphere
Plasma Wave Instrument **(PWI)**	Detailed analysis of the structure and dynamics of magnetosphere
Mercury Sodium Atmospheric Spectral Imager **(MSASI)**	Abundance, distribution and dynamics of sodium in the exosphere
Mercury Dust Monitor **(MDM)**	Distribution of interplanetary dust in Mercury orbit

Table 4.3 MMO scientific payload (Schulz and Benkhoff, 2006)

The MMO will be spin stabilized, with a rotation rate of *15 RPM* and a spin axis almost perpendicular to the orbital plane of Mercury around the Sun. This choice of spin axis ensures that the top and bottom of the spacecraft are never Sun-pointed, and enables Earth-pointing of the high-gain antenna with only one degree of freedom mechanism. The centrifugal effect of the spin will enable the deployment of four *15-meter-long* wire antennas for electric field and radio wave measurements. The orbiter will also be

equipped with two five-meter-long masts to provide a suitable environment for magnetic field measurements, clear of the influence of the spacecraft structure and electrical equipment.

4.2 Mercury Orbiter Radio science Experiment

The Radio Science experiments are a series of measurements and scientific goals that are foreseen during the mission BepiColombo. The acronym MORE synthetizes the complexity of these activities that, however, are not neatly distinguishable in independent experiments because each one of them depends to some extent upon the intermediate and final results of the others. Nevertheless, the fields of interest allow discerning a *gravimetry experiment*, with the goal of determining the gravity field of Mercury; a *rotation experiment*, with the goal of determining the rotation state of Mercury and a *relativity experiment*, with the goal of determining the post-Newtonian parameters and other quantities of interest in the very accurate dynamic modeling of the solar system, such as the mass and the dynamic oblateness of the Sun (Milani et al., 2001).

The Mercury Planetary Orbiter will be tracked from ground antennas with an ultra-stable multiple frequency radio links. Range and range rate will be thus measured with great accuracy (the expected RMS are a few tens of cm and a few tens of micron/s).

The sophisticated radio tracking data will allow an extremely accurate orbit determination that will carry out three separate data products:

- the initial conditions of the mercurycentric orbit of the spacecraft, for each short arc corresponding to an observing session from the ground antenna;
- the update of Mercury's ephemeris;
- the parameters appearing in the equations of motion of the spacecraft, including the harmonic coefficients of the planet's gravity field and the non-gravitational perturbations.

The non-gravitational perturbations, particularly strong in the intense radiation environment of Mercury, can be removed from the list of unknowns by replacing them with the readings of the on-board accelerometer. Therefore, the orbit of the spacecraft and the ephemeris of the central body are better determined, and especially the gravitational anomalies are well isolated by any other perturbations, which can act with similar effects.

Since the pericenter of the MPO will be at an altitude of *400 km*, its orbit will be mainly sensitive to gravity anomalies with a scale equal or larger than about *400 km*. The tracking data, especially the range rate, taken during the low portion of the orbit will be most sensitive to the gravity anomalies of degree up to *20*. The tracking data taken during

the high portion of the orbit will be more sensitive to the low degree harmonics, and to the Love number k_2 and the rotation parameters.

The initial conditions of the mercurycentric orbit of the MPO, available for every short observed arc, can be propagated to estimate the position of the spacecraft even outside of the tracking periods. The accuracy is of course degraded but the MPO will still be an extremely stable platform realizing accurately an absolute, inertial reference system (thanks to the dedicated on board accelerometer). From this platform a high-resolution camera (used especially for mapping the planet) will repeatedly look at a number of patches on the surface.

The pointing direction of the camera will be well known, therefore, correlating continuously images of surface features, the rotation of the planet in the inertial frame defined by the MPO and the stars will be estimated with extremely high accuracy. Further, the gravity analysis will carry out a more accurate estimate of both obliquity and longitudinal librations that, together with the quadrupole harmonic coefficients, provide to solve for both C/MR^2 and C_m/C.

4.2.1 Scientific goals

The Mercury Orbiter Radio science Experiment aims at different scientific fields that range from planetology to general relativity. The varied goals allow distinguishing three specific areas:

- *gravimetry*: reconstruction of the planet's gravity field, the coefficients of the spherical harmonics expansion up to degree and order *25*, and the Love number k_2. The expected accuracies range from signal to noise ratio of 10^4 for degree *2*, to SNR of *10* for degree *20*;

- *rotation state*: estimation of the rotational state of Mercury by means of obliquity and amplitude of the physical librations in longitude (< 2 *arcsec* ≈ 25 *m* on the surface with optical landmarks tracking, and $\approx$ *1 arcsec* with gravity). These measurements, carried out in cooperation with the camera team, provide the moments of inertia of the whole planet and its mantle;

- *relativity*: determination of the post-Newtonian parameters, the mass and the oblateness of the Sun, and the upper limits to the temporal variation of the gravitational constant *G* (relativity experiment).

The challenging objectives addressed to the radio science experiment depend strictly on the synergy of the different measurements. The radio tracking data provide the basis of a precise orbit determination that is essential to produce accurate observables with laser altimeter and high-resolution camera. The MPO orbit reconstruction represents, hence, the main goal of the radio science experiment. Accuracies of *0.1-1 m* in the radial

position and of *1-5 m* in the other direction are required to satisfy the demand of the other instruments. The position of the MPO in the Hermean frame (whose origin is defined by zeroing the dipole terms in the harmonic expansion of the gravitational potential) will be used for the appropriate referencing of the laser altimetric measurements and the images from the high-resolution camera. The combination of altimetric and gravity measurements will provide the topographic heights, a crucial information to determine the structure of Mercury's crust and outer mantle.

The along- and across-track position of the spacecraft is crucial for the rotation experiment, aiming to determine the rotation state of the planet by means of optical landmark tracking. The pole position and physical librations in longitude will be obtained from a precise georeferencing of high-resolution images (*5 m* pixel size at pericenter). The final accuracy of this experiment rests not only upon an accurate knowledge of the spacecraft position, but also on the quality of the attitude reconstruction. The onboard star trackers and gyroscopes should allow an accuracy of *1-2 arcsec*. In addition, the spacecraft design ensures a high stability of the optical alignment between the star trackers and the camera.

4.2.2 On board instrumentation

The MPO is equipped with two fixed Low-Gain Antennas (LGAs), a steerable Medium-Gain Antenna (MGA) and a steerable one-meter-diameter High-Gain Antenna (HGA). The two X-band LGAs will provide omnidirectional coverage at small distances from Earth and can also be used for emergency commanding at any distance. The X-Band MGA will be used primarily during the interplanetary cruise phase and in safe and survival modes. The HGA will provide X-band uplink and downlink and Ka-band downlink communications for spacecraft and science operations. The HGA will also be used during the cruise phase to enhance communications and data dump capabilities whenever needed.

ESA's Cebreros *35-meters* ground station is planned to be the primary ground facility for communications during all mission phases. The ground stations at Kourou (LEOP), New Norcia (critical phases during cruise and Mercury capture), Perth (LEOP), Usuda (backup) and Uchinoura (backup) will be available for backup during critical flight phases and/or for use during special campaigns. An additional station that will be probably the DSS 25, a *34 m* antenna of NASA's Deep Space Network located in Goldstone (California) will provide the tracking in Ka band of the radio science experiment.

The crucial onboard elements of the MORE experiments are the TLC/TCM deep space transponder (DST) and the Ka/Ka transponder (KaT), provided by the Italian Space Agency. The KaT and the DST are particularly important because they enable a multi-frequency radio link at X (*7.2 GHz* uplink/*8.4 GHz* downlink) and Ka band (*34/32.5 GHz*), a configuration already exploited by the Cassini mission (Bertotti, et al. 2003;

Tortora, et al. 2004). Thanks to this configuration, range rate measurements will attain accuracies of *3 μm/s* (at *1000 s* integration time) at nearly all solar elongation angles. In the geometric optics limit, the use of multiple frequencies allows a complete cancellation of plasma noise, the dominant noise source in S and X band radio links (Bertotti et al., 1993). A novel wideband ranging system (WBRS), based upon a pseudo-noise modulation scheme at *24 Mcps*, will provide observables accurate to *20 cm* (two-way) (Iess and Boscagli, 2001).

The effects of non-gravitational accelerations on the spacecraft dynamics (quite large in the harsh Hermean environment) will be removed to a large extent thanks to the ISA accelerometer. These instrument readouts will be sent to ground in the telemetry stream and referenced to the phase center of the high gain antenna. The orbit determination code will then use a smoothed version of the accelerometer measurements to integrate the equation of motion, effectively realizing a software version of a drag-free system.

Although MORE will make use of laser altimetric and optical images to stabilize the global orbital solution, the crucial observable quantities are range and range rate. These quantities are generated at the ground station after establishing a two-way coherent link. The core element of the tracking system is the reference oscillator, a H-maser with a frequency stability of one part in 10^{15} over time scales of *1000 s*. The orbital solution is obtained from the observable quantities by means of a least squares fit, where the state vector of the spacecraft and the parameters of the dynamical model are jointly derived.

4.2.3 Dynamical perturbations

The intense radiation environment of Mercury generates strong non-gravitational perturbations on the spacecraft. The on-board Italian Spring Accelerometer will allow measuring continuously the magnitude of these perturbations and, hence, decoupling the gravity signals in the tracking data. Although the dynamical noise from non-gravitational accelerations (mainly solar radiation pressure, planetary albedo and infrared emission) will be removed to a large extent by means of the on-board accelerometer, the intrinsic noise of the instrument leads to instabilities in the spacecraft orbit determination. The calibration of ISA is therefore a thorny issue because of its implications for the radio science experiment. The calibration formula for ISA is as follows:

$$a = k_x x + k_T T + b + n_{NL} \tag{4.1}$$

where x is the accelerometer reading, a is the absolute acceleration, k_x is a scale calibration factor, which is calibrated in flight to an accuracy sufficient for the purpose of this experiment and T is the instrument temperature. The n_{NL} are the nonlinear effects and short period noise, which are known (from the ground tests) to be smaller than the required accuracy. The thermal sensitivity $k_T = 5 \times 10^{-4}$ *cm/s*^{2} *K* is well known from ground measurements, but the absolute value of the temperature and the absolute calibration b are not easy to measure with the necessary accuracy. Nevertheless, the

instrument will be maintained at specific design temperatures with an uncertainty of about *1 K* that limits accelerometer bias and drift.

The physical noise model (Iafolla and Nozzoli, 2001) that justifies the results of the long-term ground tests of ISA is reported in Figure 4.5. The numerical simulations of the radio science experiment have taken into account this noise that is correlated over time scales of the order of the orbital period simulating thermally driven changes to the calibration. These systematic components of the acceleration noise are an important cause of the systematic errors in the results of the gravity field reconstruction.

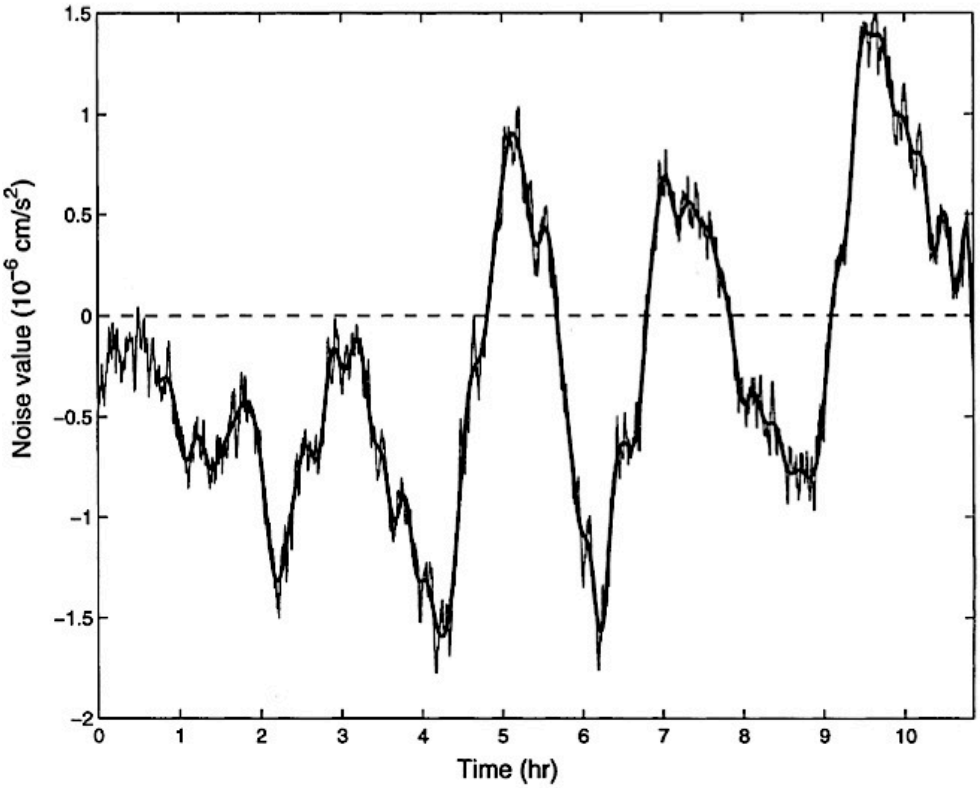

Figure 4.5 Accelerometer noise model (Milani et al., 2001)

Unfortunately, the accelerometer intrinsic noise does not represent the unique perturbation of the radio science experiment during the MPO orbit. Residual ΔV due to unbalanced thrusters for momentum dumping maneuvers will penalize further the spacecraft orbit determination.

The large solar, planetary albedo and infrared fluxes apply significant torques on the spacecraft because of the offset between the center of mass and center of pressure. During the orbit, the MPO attitude will be controlled by means of the reaction wheels. The tight mass and volume constraints limit the wheels dimension and therefore the angular momentum stored on board. According to current estimates, momentum-dumping

maneuvers may occur as frequently as *12 hours*, rather than once a day, as initially required. The MORE team has requested that the maneuvers take place outside tracking passes from the primary ground station of the experiment. The sequence of maneuvers and tracking passes (approximately *8 h* long) is shown in Figure 4.6. The Ka-band/multifrequency tracking period is followed by the unobservable arc (*~16 hours*), during which the wheels off loading maneuvers (DSM1 and DSM2) will occur.

Two complementary sets of thrusters will carry out the desaturation maneuvers of the MPO. Unfortunately the thrusters are unbalanced, so that the torque is associated to a quite significant thrust. The ensuing, large velocity variations (nearly *6-8 cm/s* for total momentum discharge respectively of *40-84 Nms*) degrade the knowledge of the spacecraft state and adversely affect the estimation of the gravity field. The knowledge of the ΔV associated to desaturation maneuvers is expected to be about *1-2 mm/s*, a value sufficiently large to cause substantial errors in the state propagation. These uncertainties are due to possible thrusters misalignments of about *1°-2°* leading to ΔV accuracies of *2%* and *5%* respectively with maximum and minimum momentum discharge.

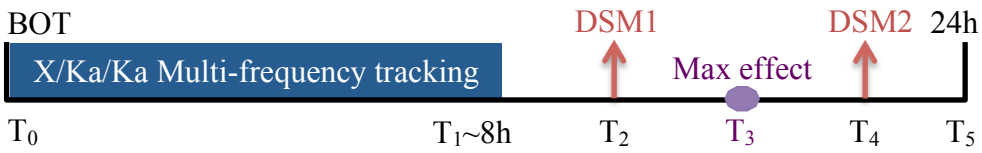

Figure 4.6 Tracking period and wheel desaturation maneuvers (DSM)

Preliminary simulations of the radio science experiment (Milani et al., 2001) indicated that the spacecraft position with respect to Mercury's barycenter shall be known with an accuracy of *10-30 m* at the beginning of the tracking pass, where the integration is typically restarted. Meeting this condition in the presence of desaturation events every *~12 hours* is not straightforward, especially if the knowledge of the actual ΔV is poor. The BepiColombo project and the prime contractor European Aeronautic Defence and Space Company (EADS) Astrium estimate that each maneuver will result in different possible configurations that vary in a range between the best and worst case (Table 4.4).

	Best case	**Worst case**
$\Delta V_x \pm \sigma_{\Delta Vx}$	0±0.5	0±0.5
$\Delta V_y \pm \sigma_{\Delta Vy}$	17±0.8	40±0.8
$\Delta V_z \pm \sigma_{\Delta Vz}$	42±2.1	69±2.1

Table 4.4 ΔV (*mm/s*) best and worst cases distribution. The x, y and z directions are respectively along track, radial cross track and out of plane (Schulte, 2009)

The maximum effect in the propagation of the uncertainties occurs in the middle of the unobserved arc (Figure 4.6). As a first approximation, the displacement in the three directions can be computed using perturbative equations. A ΔV event changes the mean motion n by an amount:

$$\Delta n = -\frac{3}{a\sqrt{1-e^2}}\left(-e\Delta V_y sinf + (1-ecosf)\Delta V_x\right) \tag{4.2}$$

so that, considering ΔV_x nominally zero, the along-track displacement is:

$$\Delta x = a\Delta\lambda = a(T_3 - T_2)\Delta n \cong 3e\Delta V_y(T_3 - T_2) \tag{4.3}$$

where e is the orbit eccentricity, f is the true anomaly, T_2 and T_3 are the epochs of the first maneuver and the maximum effect. The along track displacement that corresponds to the best and worst cases are respectively about *176 m* and *414 m*. The change in eccentricity:

$$\Delta e = -\frac{\sqrt{1-e^2}}{na}\left(-\Delta V_y sinf + (cosE + cosf)\Delta V_x\right) \cong \frac{\sqrt{1-e^2}}{na}\Delta V_y sinf \tag{4.4}$$

produces variations in the along-track and radial directions, by an amount:

$$\begin{aligned} \Delta x &\cong 2a\Delta e \\ \Delta y = a\Delta e &\cong a\frac{\Delta V_y}{V} \end{aligned} \tag{4.5}$$

where $V \approx na = 2.55\ km/s$. In the best case the along and cross track displacements are *46 m* and *23 m*, whereas they correspond to *106 m* and *53 m* in the worst case. Each event changes also the inclination and longitude of the ascending node:

$$\begin{aligned} \Delta i &= \frac{1}{na\sqrt{1-e^2}}\frac{r}{a}\Delta V_z cos(f+\omega) \cong \frac{1-ecosM}{na}\Delta V_z cos(f+\omega) \\ \Delta\Omega &= \frac{1}{na\sqrt{1-e^2}}\frac{r}{a}\Delta V_z\frac{sin(f+\omega)}{sini} \cong \frac{1-ecosM}{na}\Delta V_z cos(f+\omega) \\ \Delta i &\approx \Delta\Omega \approx \frac{\Delta V_z}{V} \end{aligned} \tag{4.6}$$

The resulting out of plane displacement is:

$$\Delta z \cong a\Delta i \cong a\Delta\Omega \tag{4.7}$$

that is ~*55 m* in the best case and ~*91 m* in the worst case.

Assuming the accuracy of the ΔV cross track and out of plane provided by EADS Astrium, the uncertainties associated to the displacement is about *11 m* in radial direction, *1 m* along y-axis and *2 m* out of plane. Although these estimates seem to confirm that the orbital perturbations are still within acceptable limits, the uncertainty of ΔV_x determines the strong effect in the accuracy of the along track displacement:

$$\sigma_{\Delta x} \cong 3\sigma_{\Delta V_x}(T_3 - T_2) = 32m \tag{4.8}$$

Better results may be obtained using the ISA accelerometer. Indeed, preliminary estimates indicate that ISA may improve the knowledge of the velocity increments to a level of *0.15 mm/s* in the along track direction (Schulte, 2009). This capability requires a new operational mode that changes the dynamical range of the instrument. Furthermore, the residual ΔV may be estimated as local solve-for-parameters in the orbit determination process. The attainable accuracy that can be reached by means of radio tracking data is ~ *3 μm/s* if the maneuver is during the telemetry tracking pass in X band. Nevertheless, when the maneuver is completely in the dark the possible accuracy is three or four orders of magnitude higher at worst.

Both perturbations, accelerometer intrinsic noise and residual ΔV of the momentum dumping maneuvers, destroy therefore the dynamical coherence of the trajectory and lead to a degraded estimation of the gravity field with pure batch estimation. In order to cope with these problems, the batch-sequential approach appears adequate to the processing of the large amount of data generated by MORE, and capable of providing the required accuracies both in the determination of the gravity field coefficients and the spacecraft orbit.

4.3 Numerical simulations of the radio science experiment

The complexity of the MPO orbit determination led us to design an estimation strategy that allows fulfilling the challenging scientific goals despite the presence of dynamical perturbations. The classical batch estimation showed evident difficulties in the spacecraft orbit reconstruction entailing poor results in a combined estimation of the dynamical model. Therefore, we have developed the batch sequential filter to access gravity and orbit attainable accuracies with the Mercury Orbiter Radio science Experiment.

The filter was devised in order to cope with the uncertainties in the dynamical models (associated to wheel off-loading maneuvers, accelerometer bias and drift, etc.). The accumulation of the errors due to unmodelled effects leads to a divergence in the trajectory reconstruction, making the multi-arc method ineffective.

With the batch-sequential method the dynamical model is updated and improved as additional, short data batches included in the solution. The sequential processing of short

batches improves the estimation of the state vector as the mission goes on. The choice of the batch duration is particularly important for a fast convergence and a good accuracy of the final orbital solutions. Its length is a trade off between the estimation accuracy of the global and local parameters. A single batch (Figure 4.7) is processed following three essential steps:

- Single-arc-estimation of twenty-two arcs (*~24 h*);
- Multi-arc estimation with initial conditions and a priori uncertainties respectively equal to the estimated values (weighted mean for the global parameters, with formal uncertainties as weights) and a priori uncertainties of the single arc estimation;
- Update of the dynamical model with the estimated parameters for the next batches.

With this procedure the processing of the following arcs benefits from an improved dynamical model, thus allowing a better estimate of the state vector. Furthermore, this sequential update carries out improved estimates of the global parameters, which attain convergence after a limited number of batches. However, the results from this first iteration may still be improved, both for the state vector and global parameters estimation.

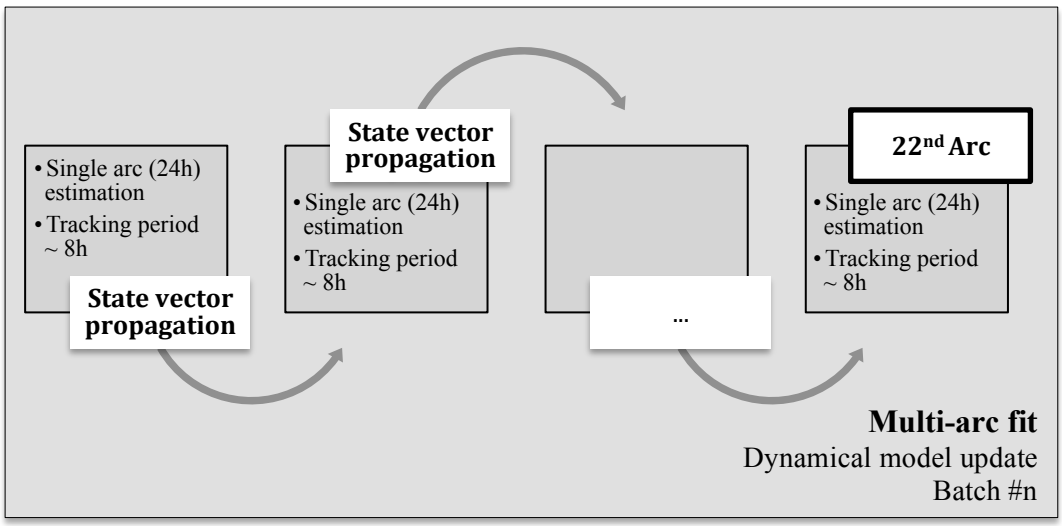

Figure 4.7 Single batch of BepiColombo numerical simulations

The initial batch processing is only the preliminary reconstruction of the spacecraft trajectory that provides the nominal values and the a-priori uncertainties for global multi-arc setup (Figure 4.8). Whereas the global parameters are initialized with the estimation of the last batch, the initial values of local parameters are obtained from the single arc estimation. This second step can hence provide an improved estimate of the global parameters. Once the dynamical model is recovered to the required accuracy, the orbit reconstruction can be obtained by means of final single-arc-estimation.

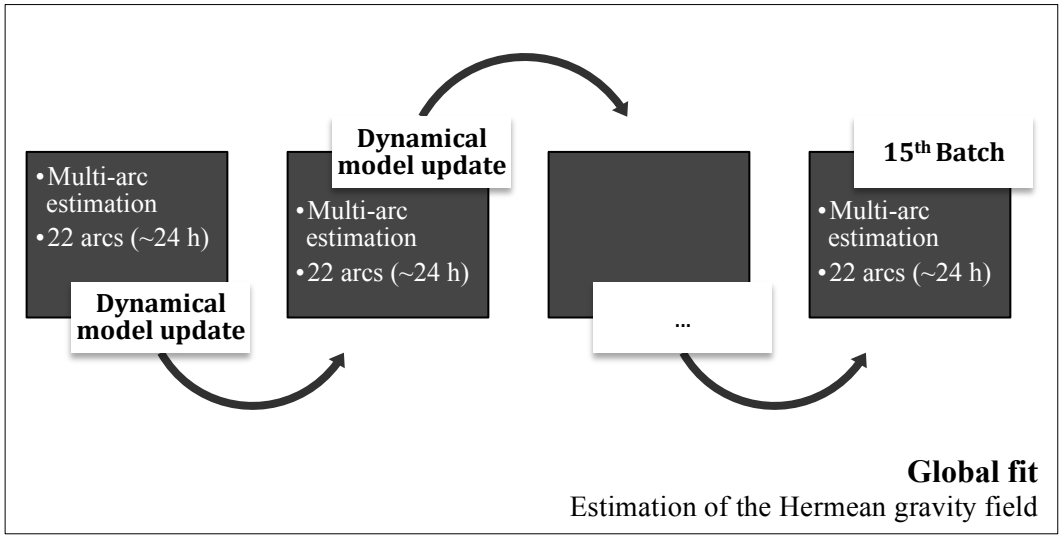

Figure 4.8 Batch-sequential estimation of BepiColombo numerical simulations

4.3.1 Simulation setup

The initial MPO orbit about Mercury is polar with pericenter and apocenter altitudes respectively at *400 km* and *1500 km*. The simulation covers a full terrestrial year, i.e. the duration of the nominal mission. Support from ground has been limited to only one station, with Ka-band uplink and multi-link capabilities. A daily tracking period of approximately *8* hours has been assumed. Loss of the radio link due to occultations and antenna blockages have also been accounted for.

Non-gravitational accelerations, such as direct solar radiation and thermal emission from the planet, are considered completely compensated because of the accelerometer measurements. In the orbit determination process the accelerometer transforms de facto the real spacecraft in a virtual, drag-free test particle (Iafolla and Nozzoli, 2001). However, residual accelerometer biases and drifts, mostly due to changes in the thermal environment, have been simulated through an acceleration noise correlated over time scales of the orbital period (Figure 4.5). The ΔV of the desaturation maneuvers, twice a

day, are also taken into account modeling the thrusters' fires as impulsive considering that are outside the tracking period. The residual velocity increments and the amplitude of the accelerometer noise are also solve-for parameters of the estimation process.

The purpose of these numerical simulations is the assessment of the scientific goals in a realistic scenario. Therefore, the local and global parameters differ between the simulation and estimation dynamical models in order to reproduce the conditions that the radio science team will cope with in the beginning of the experiment.

4.3.2 MPO preliminary trajectory reconstruction

The batch-sequential filter was basically built as a paramount structure around the Orbit Determination Program (ODP) of the Jet Propulsion Laboratory (JPL). The ODP is generally used to process the radio tracking data in a classical batch mode. The mission period is partitioned in different arcs that are processed separately reconstructing the trajectory of the spacecraft. Therefore, a combined estimate of these arcs leads to refine the solution of the global parameters. The purpose of this over-parameterization is to absorb the unmodeled perturbations, which accumulate with time and would make impossible to solve for a purely deterministic orbit over much longer arcs (Milani et al., 2001). The arc length represents a crucial parameter in this process and it should be chosen in order to contain a single tracking window during the pass. The numerical simulations reported in this work foresee an arc extension of one earth day providing only a single station with a triple link radio tracking period on average of *8* hours. Nevertheless, the classical batch estimation strategy carries out instable solutions because of the state vector errors propagated during the mission reach *1 km* in position and *1 m/s* in velocity.

The complexity of this mission scenario led us to think about an estimation process that allows reducing the modeling errors from the non-conservative forces, which grow quadratically with time (Genova et al., 2012). The main idea of the batch-sequential strategy is to exploit a certain number of arcs (*batch*) in a combined solution so that the dynamical model improves continuously. Therefore, the estimated global parameters are sequentially updated in the following arcs and the benefits on the orbit reconstruction are highlighted since the errors of the state vector approach respectively orders of *1 m* and few *mm/s* (Figure 4.9). The number of the arcs processed in a batch depends essentially on the orbit configurations of the spacecraft and the central body. In the case of BepiColombo, we used a batch length of *22 arcs*, which practically correspond to less than half Mercury's rotation period and about *220* orbits of the MPO.

The choice of the arcs number into a batch depends basically on the trade-off of two conflicting needs. The determination of the spacecraft trajectory requires frequent updates of the dynamical model in order to reduce the propagation errors. Nevertheless, the recovery of the global parameters improves considerably as more data are processed in the combined solution.

At the end of the preliminary processing, the reconstructed trajectory is used as initial guess in a final multi-arc estimation that provides an overall solution of the dynamical model (Mercury's gravity field coefficients). The improved model is therefore exploited to recover an accurate trajectory of the spacecraft that may be used from the teams of high-resolution camera and laser altimeter.

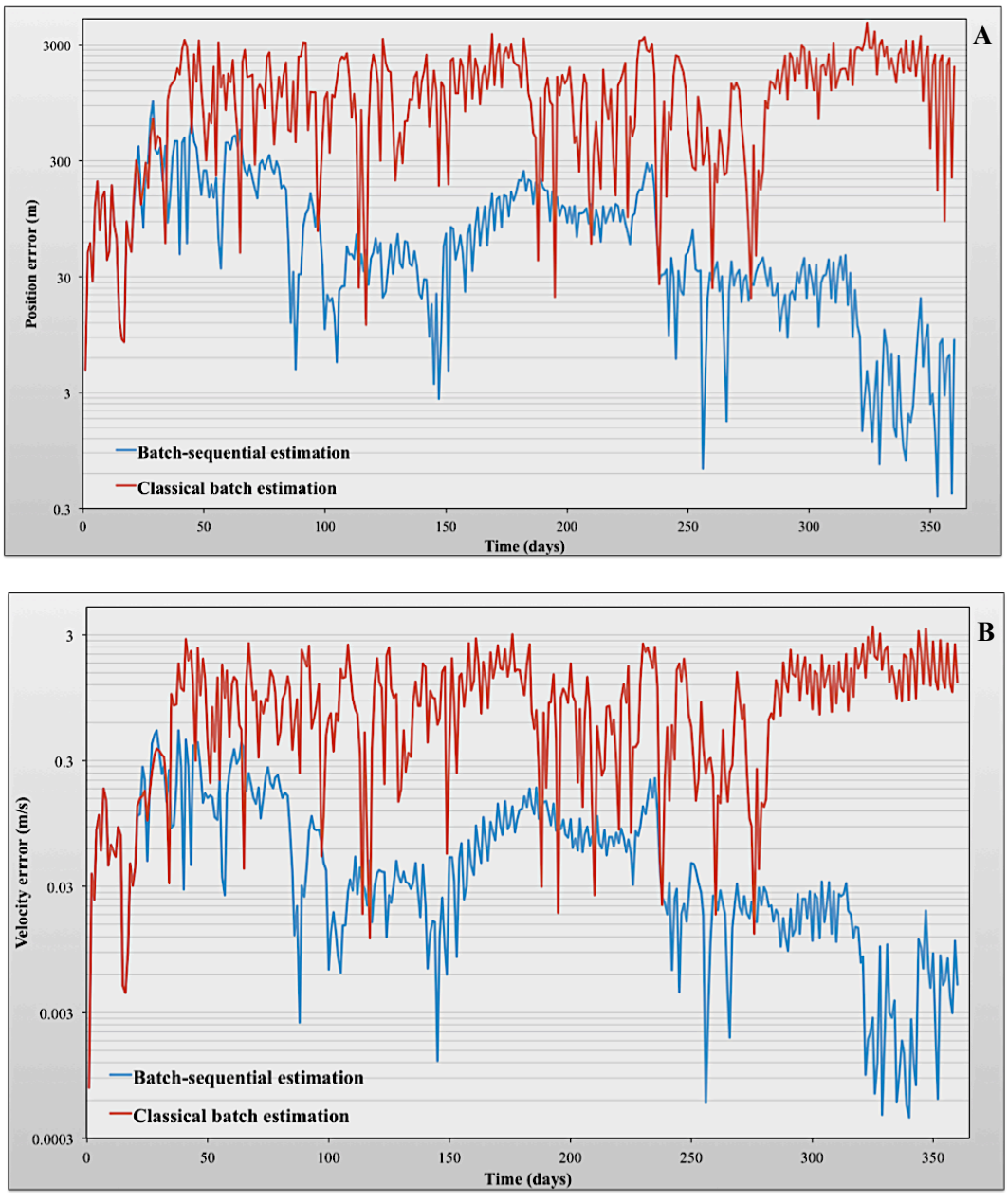

Figure 4.9 A. MPO position and **B.** velocity errors with classical batch and batch-sequential estimations

4.3.3 Recovery of Mercury's gravity field

The numerical simulations of the MORE experiment have been an excellent test bench for the batch-sequential filter. The classical batch estimation is insufficient to satisfy the goals in the orbit reconstruction and gravity field determination. Much better results have been found with the batch-sequential method. The sequential updates of the dynamical model drastically drop the MPO orbit reconstruction errors. The recovered trajectory is set as initial guess in a global multi-arc estimation that carries out the Mercury's gravity field coefficients (Figure 4.10).

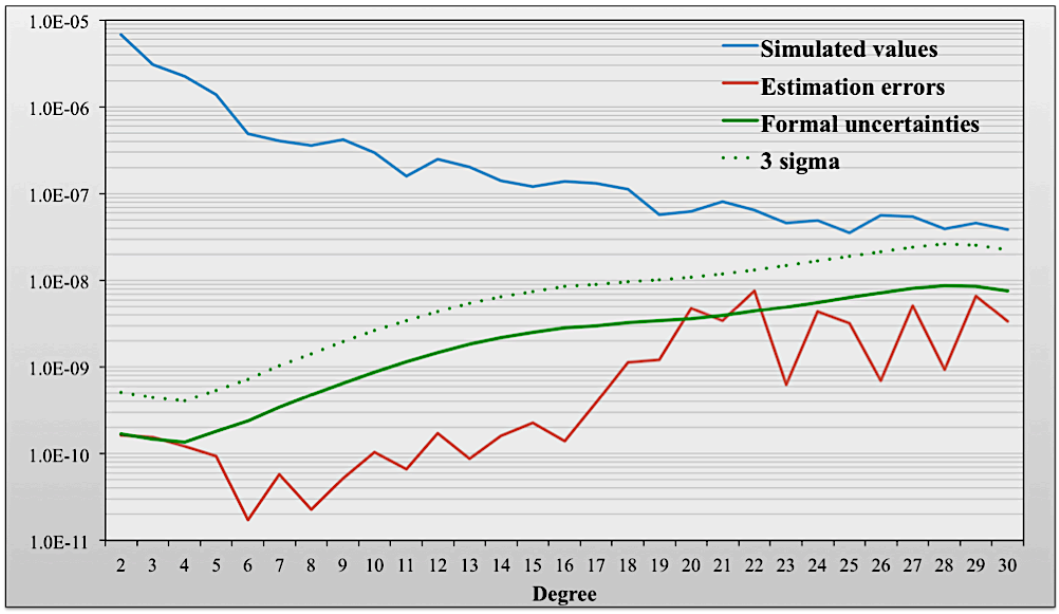

Figure 4.10 Mercury's gravity field coefficients

The mission goals for the relative accuracy of the harmonic coefficients are fully met and the estimation is statistically coherent. Since the degree 20, the estimation error increases, but still remains in a range between one and three sigma and can therefore be considered as statistically acceptable. So we reported on the errors of the gravity field coefficients on the geoid, which is defined as an equipotential surface of an isolated planetary body. Figure 4.11 plots the difference between the geoid heights of the simulated and estimated values at the end of the final global fit. The scientific requirement of the determination of the geoid heights with accuracy of *20 cm* in spatial scales of *300 km* is fully fulfilled. The mean error of the geoid heights is about *1-10 cm*

and structures due to tesseral harmonic of degrees *20* and *22* are easily distinguishable because of their higher errors.

The Love number k_2 is also well determined showing an estimation error of about 1.0×10^{-3} consistent with the formal uncertainty of 3.0×10^{-3}. The requirement on the measurement of the Mercury's tides is so completely fulfilled highlighting a relative accuracy of *1%*.

The improved gravity model, maneuvers and periodic accelerations are finally exploited in a final single arc estimation that leads to optimize the orbit reconstruction (Figure 4.12).

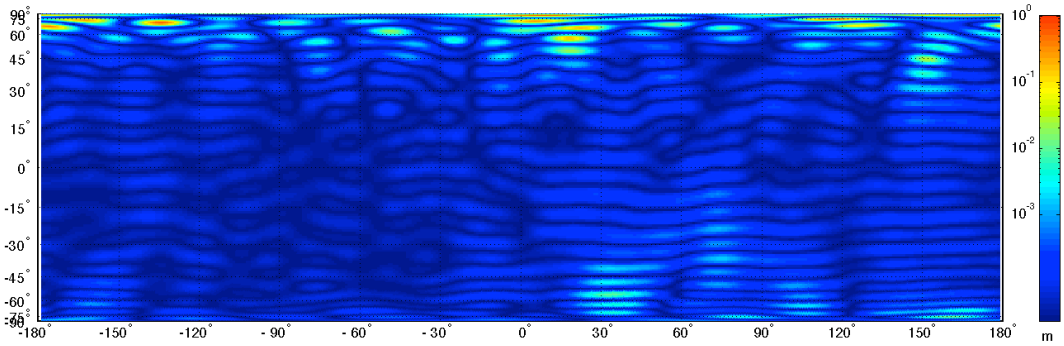

Figure 4.11 Errors on the geoid heights

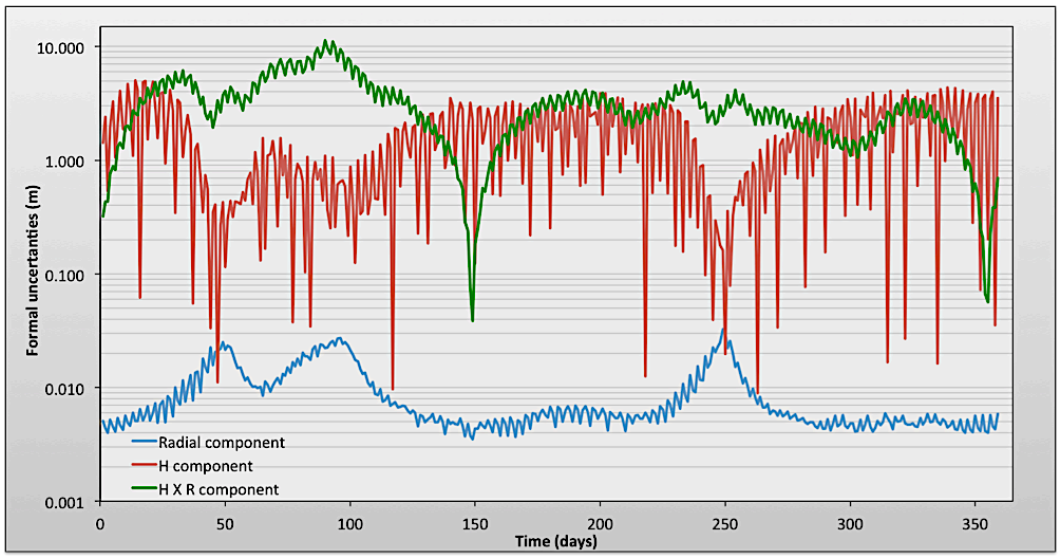

Figure 4.12 Uncertainties in position after final orbit reconstruction (in the orbital frame)

The state vector uncertainties, at the end of the process, fully satisfy the requirement of the laser altimeter on the radial direction. Since the instrument accuracy is about *1 m*,

the radio science experiment provides a maximum uncertainty of *20 cm*. Concerning the rotation experiment, the $H \times R$ direction, which represents around the along track direction because of the low eccentricity of the orbit, shows an average uncertainty of about *3 m*, perfectly compatible with the scientific goals. However, during the evolution of the orbit the $H \times R$ direction becomes periodically the weak direction entailing the increment of its formal uncertainty. The inclusion of optical observables, as the pattern matching of high-resolution images, or laser altimeter crossovers in the estimation process could improve the orbit determination since the radio tracking data generate this weakness.

4.4 Conclusions

Numerical simulations of the BepiColombo radio science experiment (MORE) show that a batch-sequential estimation is fully adequate to reach the mission requirements in orbit determination and gravity field reconstruction. The batch-sequential filter provides the advantages of a batch method (i.e. a-posteriori data processing and superior stability), while adding sequential updates of the dynamical model. In our approach, observation data are processed in three steps: batch-sequential estimation (initialization of local and global parameters), multi-arc estimation (improvement of the global parameters) and single arc estimation (trajectory reconstruction).

Position errors are consistently found below *10 m* in the along and across track components, while much better accuracies are obtained for the radial component. The orbital reconstruction is therefore fully adequate to support the laser altimetric observations (accurate to 1 m in the nadir direction). In the remaining two components (along- and across-track) the orbit determination accuracies are significantly larger, but still compatible with the requirements of optical landmarks tracking.

Better results are expected if additional observations become available. In the current planning, BepiColombo's MPO will be tracked by two stations, namely ESA's *34 m* antenna in Cebreros, supporting mission operations, and NASA's Deep Space Network antenna DSS 25 in Goldstone (California) for the radio science experiment. X-band Doppler data acquired at the Cebreros antenna may prove valuable for the estimation of the ΔV associated to desaturation maneuvers.

Unfortunately, the spacecraft orbit configuration reported on this chapter probably will not reflect effectively the future mission scenario. Our estimation of Mercury's gravity field with radio tracking data of MESSENGER, consistently with the NASA team, highlights higher values of the zonal harmonics rather than the expectations (Garcia et al., 2010). In *Chapter 5* we show the implications of the updated Mercury's gravity field on the MPO orbit assessing all possible scenarios that spacecraft may cope with. The European Space Agency had called many meetings about this critical issue aiming to analyze the results carried out by MESSENGER and MORE team. Although this topic is still under investigation, in *Section 5.3.3* we present possible alternatives that may work it out fulfilling mission scientific goals and spacecraft thermal resistance.

Chapter 5

Results

Outline. The radio tracking data analysis of the NASA mission MESSENGER led us to estimate the Mercury's gravity field. The quadrupole coefficients provide important constraints on the interior structure of Mercury because they are directly relatable to the radial distribution of density. The low-degree gravity field, combined with planetary spin parameters, yields the dimensionless polar moment of inertia $C/MR^2 = 0.354 \pm 0.017$, where M and R are Mercury's mass and radius, and a ratio of the moment of inertia of Mercury's solid outer shell to that of the planet $C_m/C = 0.450 \pm 0.035$, confirming the possible presence of liquid portion of the core. The knowledge of the Hermean gravity field allows us not only to determine the geodesy of the planet but also to foresee the spacecraft orbit evolution of the ESA mission BepiColombo. The zonal harmonics cause drastically the increase of the MPO orbit eccentricity that determines the decrease of the pericenter altitude from *400 km* to *200-150 km* after two years of the mission.

5.1 Mercury's gravity mapping

The internal structure of planets preserves substantial information regarding processes that have influenced thermal and tectonic evolution, and measuring a planet's gravity field provides fundamental information for understanding that body's internal mass distribution. Further, comparing gravity anomalies and topographic altimetry leads to determine planet's crust thickness and density distribution.

We present here Mercury's gravity anomalies and gravitational potential (geoid) (Figure 5.1A-B) comparing our results with the topography carried out by the MESSENGER team of the Mercury Laser Altimeter (MLA). Figure 5.1-B shows broad gravity low in the northern lowlands, *~2 km* lower in elevation than surrounding terrain and approximately centered over the north pole (Zuber et al., 2012). At mid-latitudes, a west-southwest-east-north-east-trending, discontinuous upland that extends for nearly half the circumference of Mercury is marked by weakly positive anomalies and thus must be largely balanced at depth by thicker-than average crust or lower-than average

densities. The gravity field in the northern hemisphere shows several regional anomalies that exceed *100 milli-Galileo* (mgal) in amplitude. One such anomaly coincides with Mercury's northern rise, a locally elevated region (centered at *68°N*, *33°E*) within the northern lowlands and north polar gravity low. Another is associated with the Caloris impact basin (*31°N*, *160°E*), where some of the anomalous mass correlates with and can be attributed to regions of high topography on the basin floor. A third positive anomaly is near the Sobkou impact basin (*36°N*, *226°E*). Other positive gravity anomalies are not obviously associated with mapped impact basins at the current resolution of the gravity field.

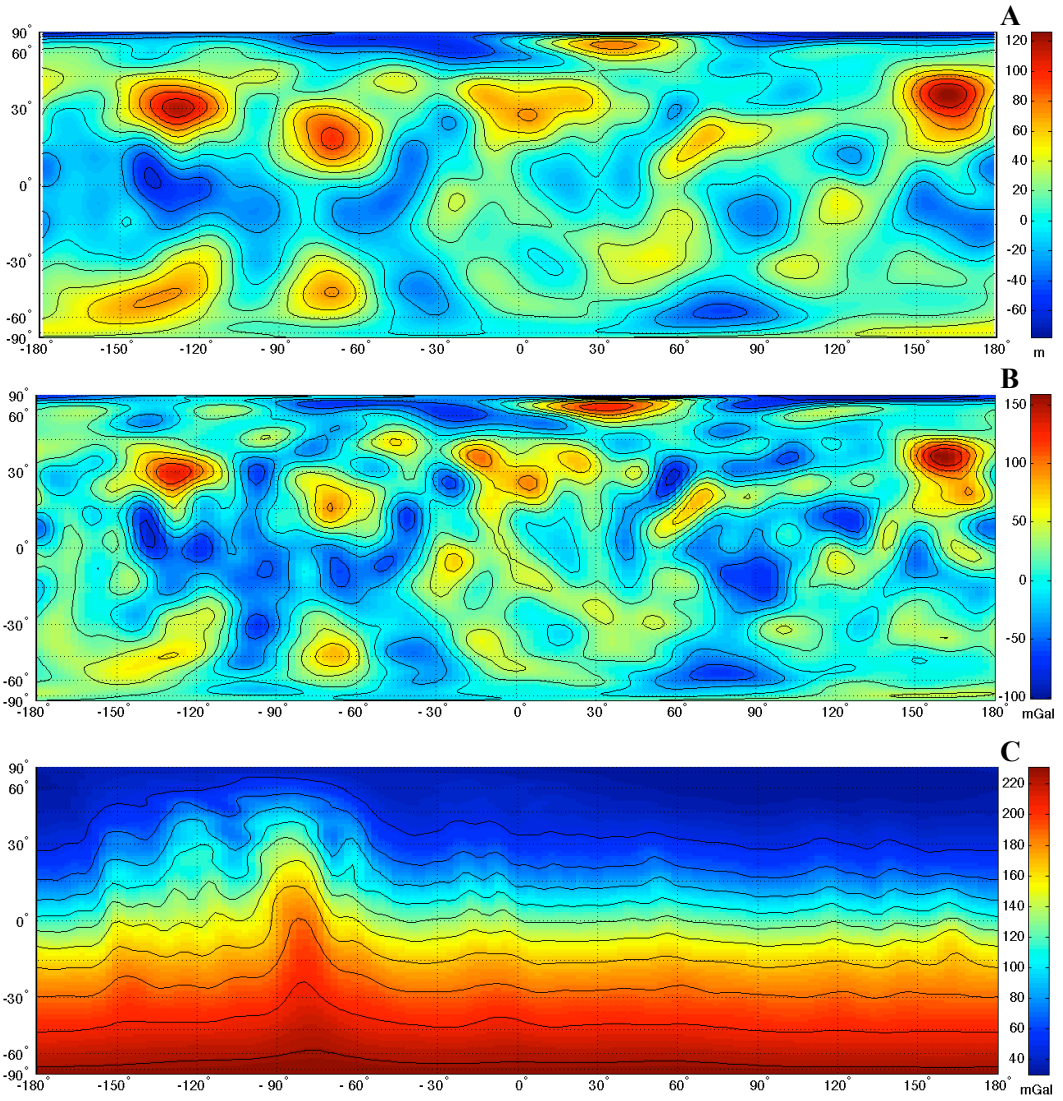

Figure 5.1 A. Geoid Heights **B.** Surface gravity anomalies **C.** Surface gravity uncertainties (*10-σ*)

The surface that represents Mercury's reference equipotential, or geoid (Figure 5.1-A), has a dynamic range of *200 m*, and its largest anomaly is centered at Caloris. Because the spacecraft altitude over the southern hemisphere is much higher than in the northern hemisphere, the geoid error, projected from the full covariance of our solution, is less than *5 m* north of the equator but reaches *20-30 m* (*1-σ*) in regions of mid- to high latitudes in the southern hemisphere. The highly eccentric orbit of the MESSENGER spacecraft permits the mapping of regional gravitational structure in the northern hemisphere at the maximum resolution of a spherical harmonic model but limits the recoverability of the gravity field to long wavelengths at southern hemisphere. The lower sensitivity in the southern hemisphere is shown in Fig. 5.1-C that represents the surface gravity uncertainties (*10-σ*). The gravity anomalies uncertainties reach *220 mGal* in the south pole because the mean spacecraft altitude in the southern hemisphere is about *15200 km*. The uncertainties in the northern hemisphere are lower than *20 mGal* highlighting that the initial pericenter latitude and altitude are respectively *60°N* and *200 km*. The high resolution of the northern hemisphere is enforced comparing the geoid determined with the HgM002 and our solution. Figure 5.2 reports on the differences between the geoid heights carried out by MESSENGER team (Smith et al., 2012) and our estimation process.

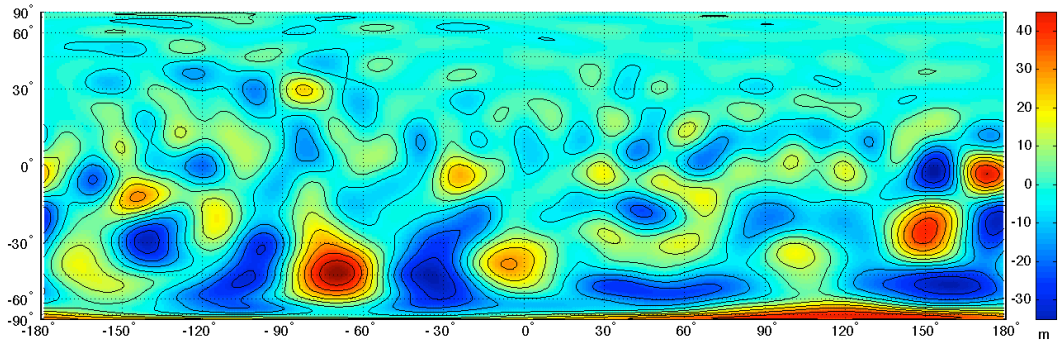

Figure 5.2 Differences of the geoid heights between the HgM002 and our solutions

The gravitational maps of the northern hemisphere strongly agree showing differences of the order of few meters for latitudes higher than *30°N*. Nevertheless, we detected higher differences of about *10 m* between longitudes *60°W-120°W*. In that regions the surface gravity in Fig. 5.1-C shows higher uncertainties due to the evolution of the spacecraft orbit. The Sun-third body effect tends to decrease the orbit eccentricity that entails much higher pericenter altitude reaching *~500 km* after three months. The spacecraft covered part of Mercury's longitudes (*60°W-120°W*) with pericenter altitude higher than *200 km* justifying the lower accuracies in the gravitational mapping.

The differences between the HgM002 and our solutions in the southern hemisphere are much higher but fully consistent with the uncertainties carried out by the estimation

process. The error range reaches *30 m* in the south pole enforcing the skepticism in the gravity representation of the southern hemisphere. The presence or absence of large geoid features in the south therefore cannot be confirmed with the present data.

5.2 Determination of Mercury's interior structure

The discovery of an intrinsic magnetic field for Mercury by the Mariner 10 flyby (Ness et al., 1974) and the preference for an internal dynamo as the source (Ness et al.. 1975) are the primary motivations for believing that Mercury has a molten core that is currently molten. However, modelers of the thermal history of the planet are not unanumous in their predictions of the current state of the core. Whether or not a given model with differentiation has a molten core that persists to the present depends criticaly on assumptions about initial conditions (the time of core formation), the time varying distribution of radioactive elements within the planet, thermal conductivities, the efficiency of convective heat transport, and perhaps most importantly, the amount of a lighter element such a sulfur that is mixed with the iron.

Since theoretical predictions about the nature of Mercury's core must remain inconclusive, empirical determination of core properties is needed to constrain and focus the theories. Whether or not the core is found to be molten, the result has profound effects on inferences about Mercury's rotational history, on theories of planetary magnetic field generation, and on theories of the thermal history (Peale et al., 2002).

The precise measurement of the second-degree gravitational harmonic coefficients (C_{20} and C_{22}), the obliquity (i_c) and the amplitude of the libration in longitude (ϕ_0) for Mercury are sufficient to determine whether or not Mercury has a molten core (Peale, 1976). The conditions for detecting the signature of the molten core are that such a core not follow the *88-day* physical libration of the mantle induced by periodic solar torque, but that it does follow the *~300 000-year* precession of the spin axis that tracks the orbit precession within a Cassini spin state. These conditions are easily satisfied if the coupling between the liquid core and solid mantle is viscous in nature.

5.2.1 Dimensionless polar moment of inertia

In determining Mercury's core structure from its rotational properties, the value of the normalized moment of inertia, C/MR^2, from the location of Cassini state 1 is crucial. If Mercury's spin axis occupies Cassini state 1, its position defines the location of the state, where the axis is fixed in the frame precessing with the orbit. Although tidal and core-mantle dissipation drive the spin to the Cassini state with a time scale $O(10^5)$ *years*, the spin might still be displaced from the Cassini state if the variations in the orbital elements induced by planetary perturbations, which change the position of the Cassini state, cause the spin to lag behind as it attempts to follow the state. After being brought to the state by dissipative processes, the spin axis is expected to follow the Cassini state for

orbit variations with time scales long compared to the *1000-year* precession period of the spin about the Cassini state because the solid angle swept out by the spin axis as it precesses is an adiabatic invariant. Short period variations in the orbital elements of small amplitude should cause displacements that are commensurate with the amplitudes of the short period terms. The exception would be if there are forcing terms in the perturbations that are nearly resonant with the *1000-year* precession period (Peale, 1988).

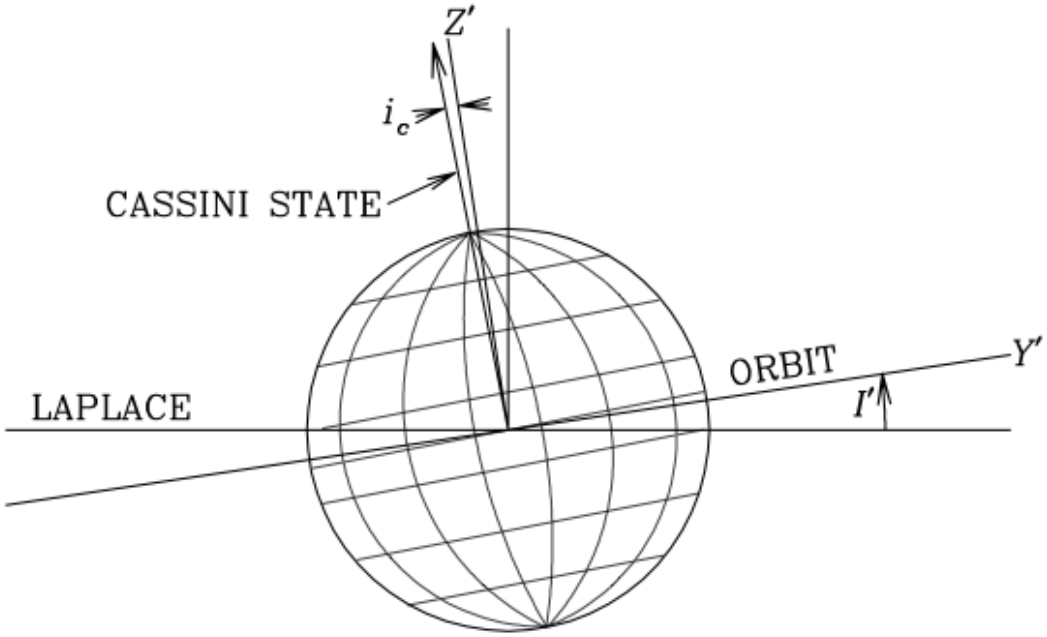

Figure 5.3 Geometry of Cassini state 1 (Peale, 2005)

Figure 5.3 shows the geometry of Cassini state 1 for Mercury, where Mercury's obliquity i_c with the ascending nodes of the equator plane on the orbit plane and of the orbit plane in the Laplace plane remaining coincident as the spin and orbit normal precess around the normal to the Laplace plane. The Laplace plane is determined mainly by Venus, Earth and Jupiter, as is the precession of Mercury's orbit. Because of the orbit precession, the spin precesses around the Cassini state and tends toward that state from dissipative effects rather than toward the orbital normal.

Earth-based radar measurements of Mercury's pole position confirm that the planet occupies a Cassini state in which the axis of rotation remains coplanar with the orbit normal and the normal to the Laplace plane as the spin vector and the orbit normal precess together about the latter with an *~300 000-year* period (Margot et al., 2007).

The equilibrium obliquity in the Cassini state allows computing the Mercury's dimensionless polar moment of inertia (Peale et al., 2002) as follows:

$$\frac{C}{MR^2} = \frac{n}{\mu}\frac{\sin i_c\left[(1+\cos i_c)\left(\frac{7}{2}e - \frac{123}{16}e^3\right)C_{22} - \cos i_c\,(1-e^2)^{-\frac{3}{2}}C_{20}\right]}{sin(I+i_c)} \qquad (5.1)$$

where μ is the precessional angular velocity of the Hermean orbit, I is the inclination of the orbital plane of Mercury relative to a reference system precessing with the orbit, e is the eccentricity and n the mean motion of Mercury's orbit. The inclination varies between $5°$ and $10°$ while the eccentricity from 0.11 and 0.24, over 10^6 years (Peale, 1976). The current values of these two orbital parameters is $7°$ for the inclination and 0.206 for the eccentricity[1]. Our estimated values of C_{20} and C_{22} (Table 3.4), combined with Earth-based radar measurements of the amplitude of Mercury's obliquity (Margot et al., 2007) provide therefore the infromation necessary to estimate C/MR^2. A slightly revised obliquity of 2.06 ± 0.1 *arcmin* yields dimensionless polar moment of inertia $C/MR^2=0.354$.

The probable uncertainty of the ratio C/MR^2 is given by:

$$\left.\frac{\Delta(C/MR^2)}{(C/MR^2)_0}\right|_{max} = \left[\sum_i \left(f_i \frac{\Delta\eta_i}{\eta_i^0}\right)^2\right]^{1/2} \qquad (5.2)$$

where η_i are the three parameters C_{20}, C_{22} and i_c. The superscript 0 indicates the nominal values of the parameters, and $f_i = -0.87,\ 0.87$ and -0.98 respectively for $\eta_i = C_{20}$, C_{22} and i_c (Peale, 1988), represent the relationship between the measured parameters and the ratio C/MR^2. The obliquity shows the strongest effect in the determination of the internal structure leading to the uncertainty of the dimensionless polar moment of inertia $\sigma_{\bar{c}} \cong 0.017$.

5.2.2 The nature of Mercury's core

The estimation of Mercury's gravity field with the MESSENGER radio tracking data and the possibility of precision measurements of Mercury's spin geometry with radar interferometry techniques (Margot et al., 2007) should unambigously determine the existence and extent of a molten core (Peale et al., 2002). Earth-based radar measurements of Mercury's pole position lead to measure the amplitude of libration, which is the maximum deviation of the angular orientation of Mercury about its spin axis relative to its orientation for uniform rotation $\psi=1.5n$, where n is the orbital mean motion. The crucial conditions that the liquid core not follow the *88-day* physical libration, but that it does follow the *~300 000-year* precession of the spin axis, are easily satisfied if the coupling between the core and the mantle is viscous in nature. Alternative core-mantle coupling mechanism of pressure forces on irregularities on the Core Mantle Boundary (CMB), gravitational coupling between an axially asymmetric mantle and an

[1] http://ssd.jpl.nasa.gov/

axially asymmetric solid inner core, and magnetic coupling between the conducting liquid core and a conducting layer at the inner surface of the mantle do not frustrate the first condition (Peale et al., 2002).

The physical libration of the mantle about the mean resonant angular velocity arises from the periodically reversing torque on the permanent deformation as Mercury rotates relative to the Sun. The amplitude of this physical libration is given by (Peale, 1976):

$$\phi_0 = \frac{3}{2}\left(\frac{B-A}{C_m}\right)\left(1 - 11e^2 + \frac{959}{48}e^4 + \cdots\right) \tag{5.3}$$

where $A<B<C$ are the principal moments of inertia of the entire planet, and e is the orbital eccentricity. The moment of inertia C_m in the denominator of Eq. 5.3 is that of the mantle (plus crust) alone, since the core does not follow the libration. The full core, and for the time being the solid inner core, are assumed axially symmetric so they do not contribute to B-A.

The second degree and order gravitational harmonic coefficients (unnormalized) are expressed in terms of the moment differences as follows:

$$\begin{aligned} C_{20} &= -\frac{C-A}{MR^2} + \frac{1}{2}\frac{B-A}{MR^2} = -(5.05 \pm 0.02) \times 10^{-5} \\ C_{22} &= \frac{B-A}{4MR^2} = (8.08 \pm 0.22) \times 10^{-6} \end{aligned} \tag{5.4}$$

where M and R are Mercury's mass and radius[2]. A coordinate system on Mercury sufficiently close to the principal axis system has to be defined. Margot (2009) has corrected the orientation model for Mercury provided by the International Astronomical Union (IAU) including oscillations in the spin rate called longitude librations. These effects result in positional errors on the surface of *~1.5 km* in latitude and up to several *km* in longitude. The updated orientation model was applied in our estimation process incorporating modern values of the spin orientation and a formulation for longitude librations, and restoring the dynamical significance to the prime meridian. The estimated second degree of the harmonic coefficients (Table 3.4) has confirmed the proximity of this coordinate system on Mercury to the principal axis system showing that the harmonic coefficients S_{22} and coefficients of degree *2* and order *1* are negligibly small.

The axis of minimum moment of inertia deviates from being aligned toward the Sun at each perihelion passage by no more than the very small obliquity, because Mercury's occupancy of the *3:2* spin orbit resonance means this axis tries to be aligned with the Sun at perihelion and any librations in longitude about this state should be completely damped (Colombo, 1965). The spin axis must be essentially coincident with the axis of maximum moment of inertia because internal dissipation will dump any wobble.

[2] http://ssd.jpl.nasa.gov/

Measurement of the amplitude ϕ_0 of the physical libration determines $(B-A)/C_m$ (Eq. 5.3), from which three known factors give:

$$\left(\frac{C_m}{B-A}\right)\left(\frac{B-A}{MR^2}\right)\left(\frac{MR^2}{C}\right) = \frac{C_m}{C} \leq 1 \tag{5.5}$$

A value of C_m/C of *1* would indicate a core firmly coupled to the mantle and likely solid. If the entire core or the outer part is fluid, $C_m/C \cong 0.5$ for the large core radius ($R_c \cong 0.75R$) in current models of the interior. Earth-based radar measurements of the amplitude of Mercury's forced libration of *35.8±2 arcseconds* combined with our estimated C_{20} and C_{22} yields $C_m/C=0.450$.

The probable uncertainty of the ratio C/MR^2 is given by:

$$\left.\frac{\Delta(C_m/C)}{(C_m/C)_0}\right|_{max} = \left[\sum_i \left(f_i \frac{\Delta\eta_i}{\eta_i^0}\right)^2\right]^{1/2} \tag{5.6}$$

where η_i are the four parameters C_{20}, C_{22}, i_c and ϕ_0. The superscript *0* indicates the nominal values of the parameters, and f_i = *-0.87, 0.87, -0.98* and *-1* respectively for η_i = C_{20}, C_{22}, i_c and ϕ_0 (Peale, 1988), represent the relationship between the measured parameters and the ratio C_m/C. The obliquity and libration in longitude show the strongest effect in the determination of the internal structure leading to the uncertainty of $\sigma_{C_m/C} \cong 0.033$.

The combination of radio tracking and earth-based radar measurements therefore confirms the presence of fluid layers in the core of the planet. Many predicted models of Mercury's interior structure have foreseen the fluid portion of the core as hypothesis that Mercury's magnetic field is the product of hydromagnetic dynamo in a liquid, metallic outer core. This mechanism as an explanation for Mercury's field requires both that a substantial fraction of Mercury's core is presently fluid and that there are sufficient sustained sources of heat or chemical buoyancy within the core to drive the convective motions needed to maintain a dynamo. Because it is known that either requirement is met in Mercury, and because of Mercury's weak field strength, more exotic dynamo models have also been considered. If the fluid outer core is sufficiently thin and the core-mantle boundary is distorted by mantle convective patterns, thermoelectric currents might be driven by temperature differences at the top of the core. These models, however, have predicted an interior structure more differentiated rather than it is given by the estimated gravity field coefficients. Therefore, more than *1 million* Monte Carlo models have been developed in order to justify the new results carried out by the mission MESSENGER (Smith et al., 2012). These models include a silicate crust and mantle, as well as an Fe-rich core that may contain solid and liquid layers and are constrained only by the mean radius (*2440 km*) and bulk density of Mercury (*5430 kg* m^{-3}). Comparison of the internal

structure models with the measured moment of inertia parameters indicates that the outer radius of the liquid portion of the core under the adopted modeling assumptions is *2030 ± 37 km*, and the density of the outer shell overlying the liquid core is *3650 ± 225 kg* m^{-3}. The procedure does not provide a size estimate for any solid inner component of the core (Smith et al., 2012).

5.3 Implications for MPO orbit evolution

The analysis of the MESSENGER radio tracking data with our batch-sequential estimation process aims at both confirming the results of the HgM002 solution published by the MESSENGER team and determining accurately the orbit evolution of the spacecraft of the ESA mission BepiColombo. Although the HgM002 and our solutions lead to analogous geophysical interpretation of the Mercury's interior structure and gravity mapping in the northern hemisphere, the orbit propagation of the BepiColombo spacecraft with the two gravity fields highlights significant changes in the evolution of the Mercury Planetary Orbiter eccentricity. The strong effect on this important orbital parameter is due to the perturbations of the zonal harmonics of the Mercury's gravity field that tend to change drastically the spacecraft orbit configuration.

5.3.1 Gravitational perturbations

The BepiColombo spacecraft will be inserted into two different polar orbits with the same pericenter altitude (*400 km*). The Mercury Planetary Orbiter will be in a low eccentric orbit (*e~0.16*) whereas the Mercury Magnetospheric Orbiter will be in higher orbit with an eccentricity of *~0.67*. Therefore, the perturbations that will act on the two spacecraft will have different influences. The main perturbations that must be considered are the following:

- Sun third body perturbation;
- Solar radiation pressure;
- Mercury non-sphericity effects (essentially zonal harmonics).

The perturbations mainly influence the eccentricity of the orbit (and hence the periherm altitude) and the argument of pericenter. The changes in the semi-major axis, inclination and ascending node due to the perturbations are poor. The effect of the solar radiation pressure is negligible when compared with the two other perturbations.

The Sun third body and gravitational perturbations are respectively dominant for MMO and MPO. The gravity field perturbations are obviously stronger for the spacecraft with the lower orbit. The principal effects are due to the oblateness of the planet that

causes the orbital plane to precess and the argument of pericenter to rotate. The precession rate (Vallado, 2007) is:

$$\dot{\Omega} = \frac{3}{2} C_{20} \frac{R^2}{a^{7/2}} (1 - e^2)^{-2} \sqrt{\mu} \cos(i) \tag{5.7}$$

where R is the Mercury's radius, a is the semi-major axis, e is the eccentricity, i is the inclination and μ is the gravitational parameter. Obviously, in case of a polar orbit, the orbital precession is zero. The change in argument of periherm (Vallado, 2007) is:

$$\dot{\omega} = -\frac{3}{2} C_{20} \frac{R^2}{a^{7/2}} (1 - e^2)^{-2} \sqrt{\mu} \left(2 - \frac{5}{2} \sin^2(i)\right) \tag{5.8}$$

~-28°/year with the estimated C_{20}.

The C_{30}-term describes the North-South mass asymmetry ("pear-shape"). For a polar orbit, it has mainly an effect on the eccentricity and the argument of pericenter, while the semi-major axis and the orbital plane remain constant. The changes in the eccentricity and in the argument of pericenter caused by C_{30} (Vallado, 2007) are given by the following formulas:

$$\dot{e} = \frac{3 C_{30} n}{2(1 - e^2)^2} \left(\frac{R}{a}\right)^3 \left(1 - \frac{5}{4} \sin^2(i)\right) \cos \omega \tag{5.9}$$

$$\dot{\omega} = -\frac{3 C_{30} n}{2(1 - e^2)^3} \left(\frac{R}{a}\right)^3 \left(1 - \frac{5}{4} \sin^2(i)\right) \left[\frac{\sin(i) \sin(\omega)}{e}\right] \tag{5.10}$$

Both effects increase as the semi-major axis of the orbit decreases and the eccentricity increases. The eccentricity and argument of pericenter rates show that these perturbations are stronger in the case of the MPO because the orbital parameters determine a higher sensitivity to C_{30}. The effect of C_{30} for the MPO is therefore about *60* and *25* times bigger than respectively for MESSENGER and the MMO.

Similar expressions tie the variations of the eccentricity and argument of pericenter to the other zonal harmonics. The magnitude of these perturbations decreases as the degree of the zonal harmonic increases. Therefore the main effect of the gravitational perturbations is given by the zonal harmonics up to degree *7*.

These gravity field coefficients define definitely the propagation of both eccentricity and argument of pericenter. In the case of the Mercury Planetary Orbiter the effect of C_{30} on these two orbital parameters is comparable with the effect of C_{40} zonal harmonic. The eccentricity rate as function of C_{40} (Vallado, 2007) is given by:

$$\dot{e} = \frac{15}{16} \frac{C_{40} n}{(1 - e^2)^3} \left(\frac{R}{a}\right)^4 \left(3 - \frac{7}{2} \sin^2(i)\right) \sin^2(i) \sin(2\omega) e \tag{5.11}$$

that is of the same order of magnitude of Eq. 5.9 when C_{40} is greater than C_{30} and the argument of pericenter is close to $\pm 45°$ or $\pm 135°$.

The ESA navigation team based the MPO orbit configuration on this tricky gravitational equilibrium. However, the expected values of the zonal harmonics (Garcia et al., 2010) were lower than the estimated coefficients provided by the MESSENGER mission. The model of the Hermean gravity field is therefore leading to important changes in the MPO mission scenario.

5.3.2 Determination of Mercury's gravity field zonal harmonics

The European Space Agency is interested in an accurate knowledge of gravitational and non-gravitational perturbations, which will determine the orbital evolution of both BepiColombo spacecraft. MESSENGER orbital phase represents therefore a unique opportunity to recover a detailed dynamical model about Mercury. Although solar and planetary radiation pressures were already roughly known, the Hermean gravity field was practically unidentified before MESSENGER orbital insertion in 2011. The analysis of MESSENGER radio tracking data provides the important chance to estimate the gravity perturbations that will act significantly on the Mercury Planetary Orbiter.

One of the main motivations of our work was therefore the need to provide a probabilistic assessment of the MPO orbit evolution, as it is known that zonal harmonics cause large secular effects on Keplerian elements. An unbiased propagation of the spacecraft state and state covariance requires that the estimate of the gravity field coefficients is carried out with only a minimum set of a priori constraints. This is especially important for the lower degree zonal harmonics, which are causing most of the change in the eccentricity. On the other hand, given the geometry of the orbit, the available data set and the large number of parameters that may need to be estimated, some constraints need to be imposed in order to avoid a runaway of the solution. In a widely used approach for terrestrial planets and the Moon, the a priori covariance of the gravity harmonics is inferred from Kaula's rule. However, a covariance analysis shows that the estimate of the harmonic coefficients up to $l=7$ can be carried out without the need of a priori information. Therefore, in the combined arcs solution only the $l>7$ harmonics were constrained using a power law, while no constraints were used in the estimate of the low degree harmonics.

A different approach was considered in the radio tracking data analysis that carried out the HgM002 solution (Smith et al., 2012). The MESSENGER team preferred limiting the power of the coefficients because of noise in areas that lack low-altitude coverage. So in the HgM002 solution, the Kaula power-law constraint $4 \times 10^{-5}/l^2$ was applied to coefficients for spherical harmonic degrees greater than $l=2$. That constraint was derived from scaling of gravitational power for the Moon.

The power level constraint of the gravity field does not change the representation of the gravity anomalies, as we reported in *Section 5.1*. However, each gravity field coefficients could be forced to fulfill the Kaula power-law that is not always reliable for the lower degrees. The estimated values of degrees $l=3$ and $l=4$ (Table 3.4) show significant differences in the zonal harmonics compared with the HgM002 solution (Smith et al., 2012). The results are still consistent because the zonal harmonics are close to the confident region ("best estimates") provided by the MESSENGER team (Smith et al., 2012).

The wide uncertainty region associated to C_{30} and C_{40} is essentially due to a good anti-correlation between these coefficients. Figure 5.4 shows the uncertainties of these zonal harmonics in the plane C_{30}-C_{40} for the HgM002 and our solutions with the estimation of 55 and 110 days. The three solutions are almost aligned along the principal axis of uncertainty ellipse highlighting the good anti-correlation between C_{30} and C_{40}. The green and blue dashed ellipses represent the formal uncertainties (10-σ) of the estimation process respectively with 55 and 110 days. The principal axes are almost parallel meaning that the correlation between these parameters is not fully broken up with additional 55 days. Although the uncertainty region is drastically reduced showing an improved knowledge of these zonal harmonics after the estimation of two full Mercury's days, MESSENGER high eccentricity and pericenter location in the northern hemisphere does not allow distinguishing accurately each gravity contribution of the different zonal harmonics.

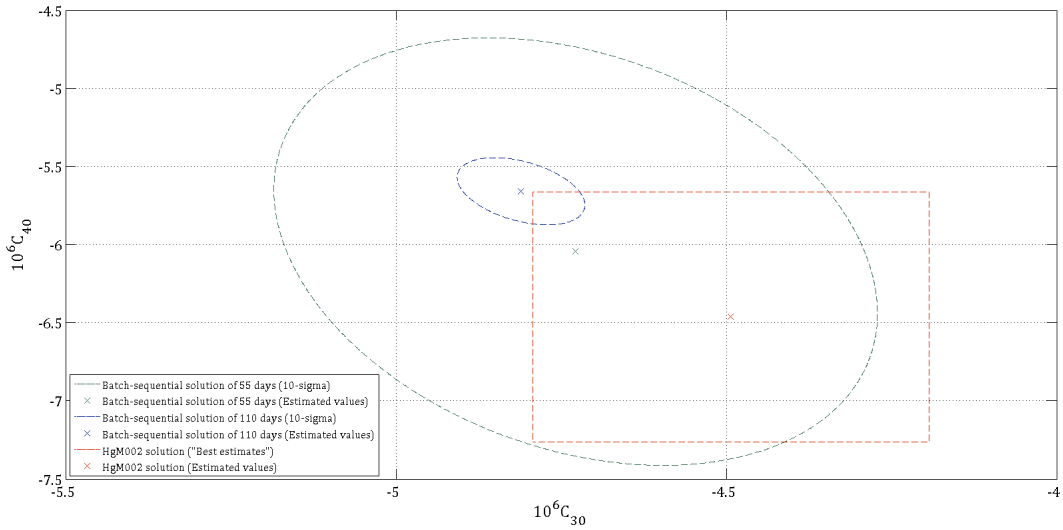

Figure 5.4 C_{30} and C_{40} correlation

The MESSENGER spacecraft orbit leads therefore to strong anti-correlations between all the zonal harmonics. Figure 5.5 shows the correlation matrix of the zonal harmonic coefficients up to degree $l=7$. The coefficients C_{l0} and C_{l+10} present high anti-

correlation that increases as the degree *l* increases reaching high anti-correlation level of about -0.95. Our estimation process has been developed therefore taking into account that either a priori uncertainties or power-law constraint could influence the estimated values of each zonal harmonic coefficient.

	C_{20}	C_{30}	C_{40}	C_{50}	C_{60}	C_{70}
C_{20}		-0.64	0.36	-0.29	0.25	-0.20
C_{30}	-0.64		-0.82	0.60	-0.48	0.38
C_{40}	0.36	-0.82		-0.89	0.73	-0.59
C_{50}	-0.29	0.60	-0.89		-0.93	0.79
C_{60}	0.25	-0.48	0.73	-0.93		-0.94
C_{70}	-0.20	0.38	-0.59	0.79	-0.94	

Figure 5.5 Correlation matrix of the zonal harmonics from degree 2 to 7

5.3.3 MPO orbit evolution

The MPO orbit design was mainly a compromise between science objectives and thermal load onto the spacecraft. Science objectives prefer a global, high-resolution coverage, implying a polar orbit at low latitudes. However, the closer the spacecraft will be to the Mercury surface, the larger the received thermal flux from the planet infra-red and albedo, which will come on top of the Sun's flux of up to about 10 Solar constants.

The approach adopted by the MESSENGER mission to endure the unfavorable thermal environment is an orbit design that limits the distance to the planet's hottest equatorial region by placing the periherm at *60°N* and selecting a highly eccentric orbit of *200×15193 km*. Only a small fraction (less than *5%*) of the orbit is spent at low altitude in the hottest thermal environment so that the spacecraft can take advantage of its thermal inertia to survive planetary heat load at *200 km*. As a consequence, high-resolution data can be obtained for only parts (about *25%*) of the Mercury surface, concentrated in the northern hemisphere at the low latitudes.

For BepiColombo a full high-resolution mapping coverage of the planet is one of the main scientific objectives, which requires an MPO orbit much closer to the planet at all times. A polar orbit at *400×1508* km with a *2.3-hour* period was selected with its apoherm on the equator on the Sun side when Mercury is at its perihelion. This is a subsolar point where thermal load on the spacecraft is at its maximum. Half a Mercury year later, at aphelion, the subsolar point occurs when the spacecraft is at its minimum distance to the planet (van Casteren and Novara, 2010).

The ESA navigation team has therefore provided a detailed mission analysis considering all the perturbations that will act on the spacecraft during the orbit (Garcia et al., 2010). The work aimed to describe the orbit evolution of both spacecraft showing all

possible mission scenarios. The crucial issue about the MPO orbit was concerning the gravity perturbations due to the C_{20} and C_{30}. Garcia (2010) pointed out that high values of these zonal harmonics entail high rate of the eccentricity and argument of pericenter. The report highlights that if C_{30} had the same order of magnitude as the C_{20}-term, it would cause the MPO to crash on Mercury's surface about *250* or *1000 days*. Although in the nominal case of that mission analysis C_{30} is one order of magnitude smaller than C_{20}-term, its effect is still as important as the Sun third body perturbation.

Despite this detailed mission analysis, the orbit configuration has not been modified because the gravitational potential of Mercury was almost unknown. Only the coefficients of degree 2, C_{20} and C_{22}, could be estimated from the data obtained by Mariner 10 in 1974-75 and improved by MESSENGER flybys in 2009. The first estimate of C_{30} from the MESSENGER flybys data was $0.5 \pm 1.9 \cdot 10^{-6}$ about one order of magnitude lower than the current estimated value. The eccentricity rate was consequently not alarming and the MPO orbit configuration was unchanged.

The orbital insertion of the MESSENGER spacecraft on March 11, 2011, gave the opportunity to update the Mercury's gravitational potential by means of radio tracking data analysis. The model of Mercury's gravity field allows a more accurate orbit evolution of both spacecraft of the mission BepiColombo. We reported on the latest orbital propagations of the Mercury Planetary Orbiter considering the models of the HgM002 and our solution.

Figure 5.6 shows the evolution of the following MPO orbital parameters during the extended mission period (two years):

A. Semi-major axis (*km*);

B. Inclination (*deg*);

C. Longitude of the ascending node (*deg*).

The semi-major axis does not strongly depend on the gravity field of the planet so its changes due to the gravitational perturbations are very small. Both gravity models determine negligible oscillations of the semi-major axis that remains almost constant during the two years. Although the small semi-major axis changes were also predicted in the nominal case of the ESA mission analysis report (Garcia et al., 2010), the evolution of the MPO inclination reported in Figure 5.6-B differs substantially from the previous orbit propagation. The ESA navigation team carried out a periodic function of the MPO inclination with amplitude of *0.06°* considering only the C_{20} and C_{30} terms. The strong gravity field entails a much higher oscillation amplitude of the MPO inclination that reaches *0.3°*. However, these inclination changes do not jeoperdize the mission requirements concerning the spacecraft safety and scientific goals.

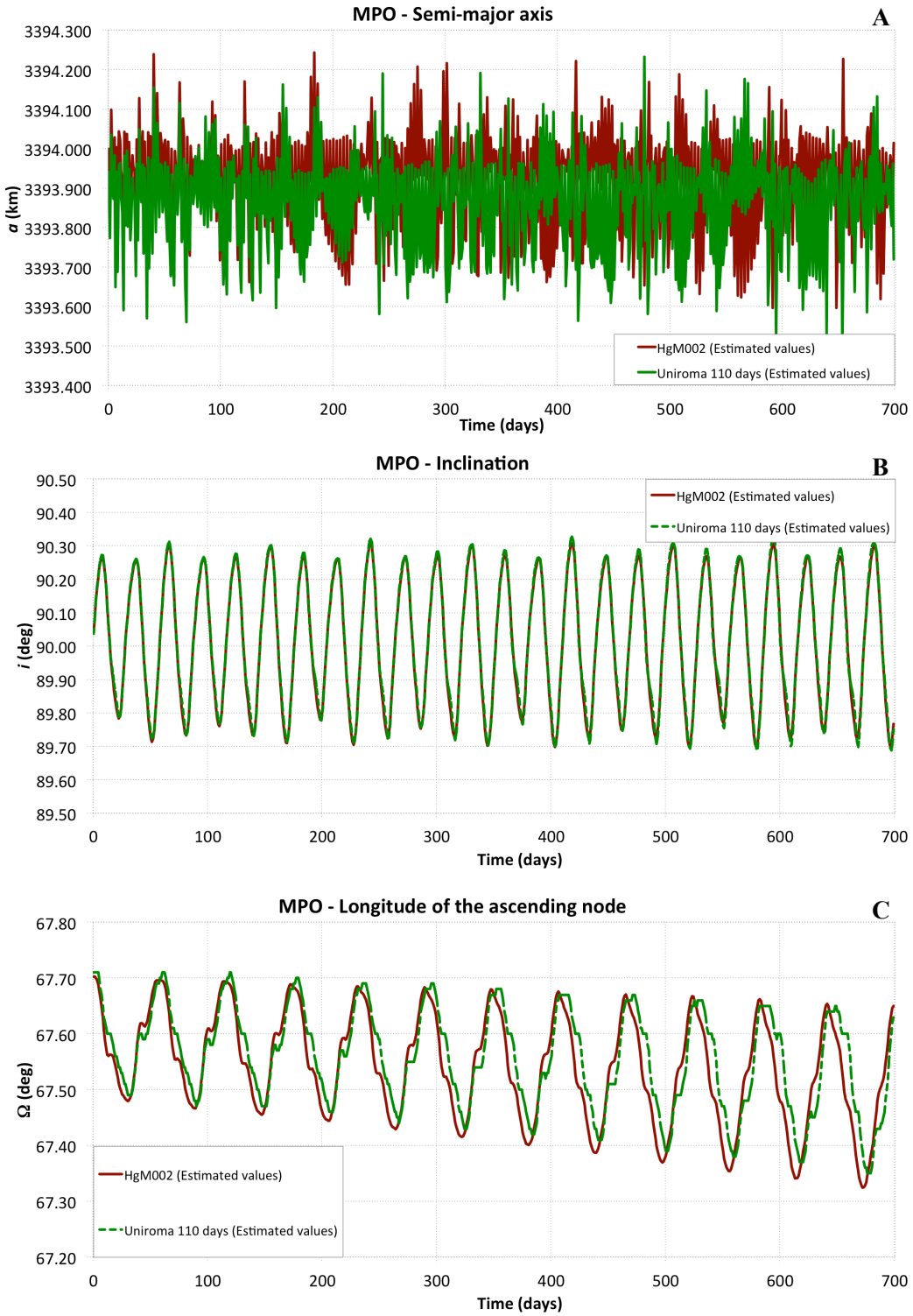

Figure 5.6 MPO orbit parameters during the two years of mission: **A.** Semi-major axis **B.** Inclination **C.** Longitude of the ascending node

The high frequency oscillation of the MPO inclination lead to a periodic variation of the longitude of the ascending node as described in Eq. 5.7. The orbital propagation with the HgM002 and our gravity model provides similar sinusoidal function of this orbital parameter. Furthermore, the longitude of the ascending node tends to decrease reaching the acceptable value of *~67.4°* at the end of the extended mission.

The main effects from the Hermean gravity field (especially zonal harmonics) are secular perturbations of the eccentricity and argument of pericenter. Figure 5.7 reports on the rate of these orbital parameters and the propagation of the MPO pericenter altitude during the mission. The C_{20} is responsible for the high negative rate of the argument of pericenter, expressed in Eq. 5.8, which drifts the orbit periherm from the northern hemisphere to mid-latitudes in the southern hemisphere. The HgM002 and our solution provide analogous propagation of the argument of pericenter in the first months of the mission. However, the difference between the estimated C_{30} lead to changes in the ω propagation. The odd zonal harmonic provides positive rate of this orbital parameter in the southern hemisphere contrasting the effect of C_{20}. Eq. 5.10 shows that higher is C_{30} lower is the overall negative rate of the argument of pericenter.

Figure 5.7-B shows the MPO eccentricity propagation during the mission. The HgM002 and our solution provide significant changes in the evolution of this orbital parameter. The eccentricity rate depends strongly on C_{30} and C_{40} zonal harmonics as described in *Section 5.3.1*. Eq. 5.9 expresses the contribution of the odd zonal harmonic to the eccentricity rate. The high negative C_{30} entails therefore high positive rate. However, the high negative C_{40} determines a negative contribution to the eccentricity rate when the argument of pericenter is negative, as showed in Eq. 5.11. Thus, joint changes of C_{30} and C_{40} zonal harmonics along the preferential direction given by the major axis of the ellipse in Fig. 5.4 lead to substantial differences in the MPO eccentricity evolution. The HgM002 gravity model determines an increase of the orbit eccentricity to a level of about *0.21* as a parabolic function of the time. The higher C_{40} entails higher negative contribution to the eccentricity rate when the argument of pericenter is about *30°*. Our model of Mercury's gravity field, characterized by higher C_{30} and lower C_{40} respect to the HgM002 values, generates an almost linear increment of the orbit eccentricity during the mission. At the end of the second extended year, the eccentricity is about 0.24.

The strong effects that the zonal harmonics determine on the argument of pericenter and eccentricity represent therefore an unexpected problem for the orbit configuration of the BepiColombo spacecraft. The high value of the eccentricity leads to lower pericenter altitude as shown in Figure 5.7-C. Both gravity models provide a substantial decrease of the pericenter altitude from *400 km* to *250-150 km* at the end of the extended mission. The wide gap between the eccentricity and pericenter altitude propagations with the HgM002 and our solution is essentially due to the uncertainties of the Hermean gravity field. Therefore, we propagated the MPO state vector initial conditions and covariance matrix taking into account the uncertainties and correlations of the Hermean gravity field coefficients. We mapped the evolution of the state vector covariance matrix during the mission.

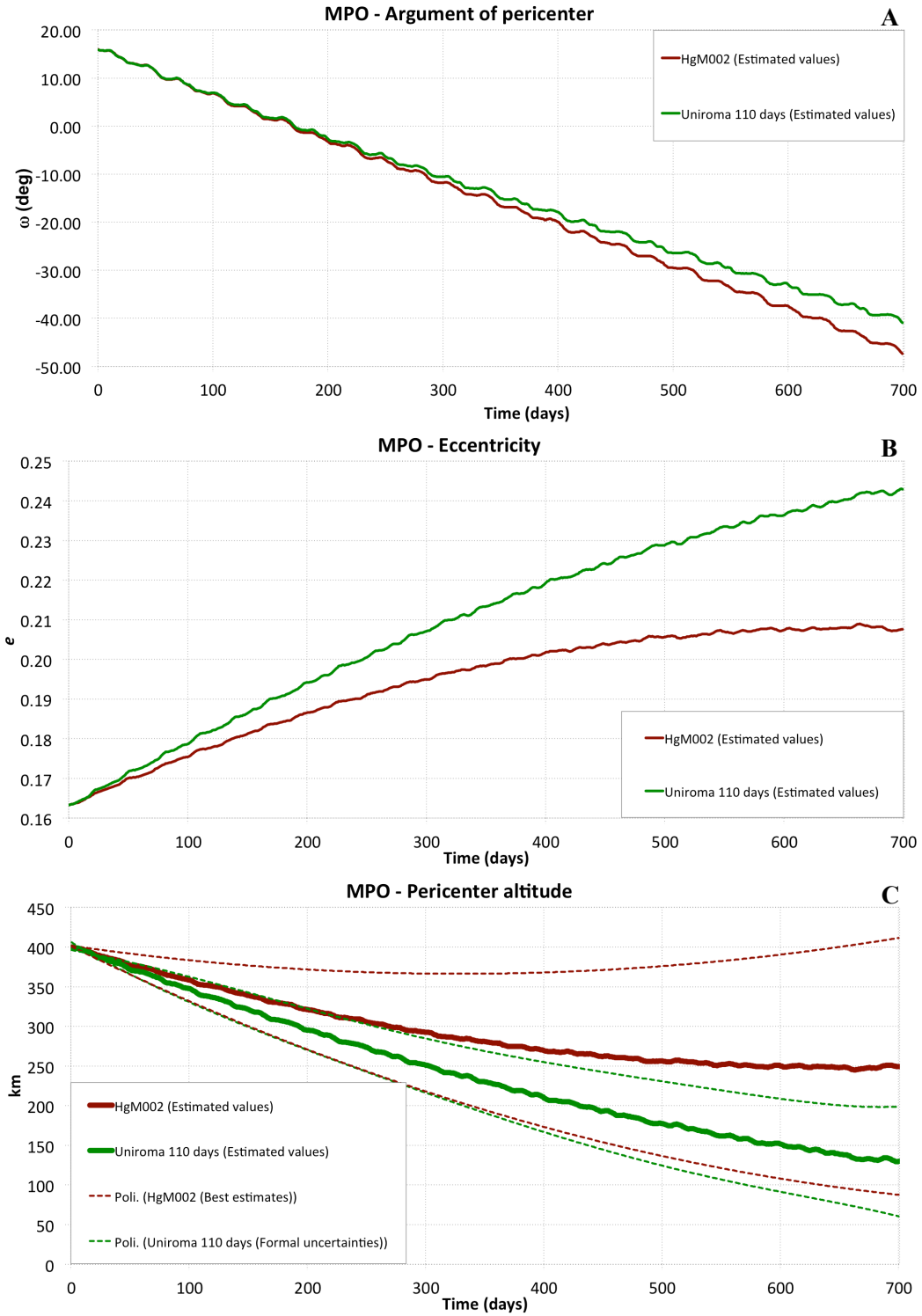

Figure 5.7 MPO orbit parameters during the two years of mission: **A.** Argument of pericenter **B.** Eccentricity **C.** Pericenter altitude

In Figure 5.7-C the red and green dashed lines represent the pericenter altitude uncertainties respectively associated to the "best estimate" reported in (Smith et al., 2012) and our covariance matrix (*10-σ*) at the end of the batch-sequential filter. The "best estimate" and our covariance matrix of the gravity field coefficients provide high pericenter altitude uncertainties of respectively *±150 km* and *±70 km* at the end of the extended mission.

Although this result suggest that the MESSENGER orbit is not well suited to an accurate prediction of the gravity perturbations of the MPO pericenter altitude, both models of the Hermean gravity field highlight the criticality of current mission configuration. The thermal resistance of the Mercury Planetary Orbiter requires a minimum altitude at the subsolar point of about *350 km*. The secular perturbations of the orbital parameters lead to subsolar point altitude of *230-300 km* as reported in Fig. 5.8. Both gravity models determine a decrease of the subsolar point altitude lower than the thermal threshold imposed by the spacecraft design.

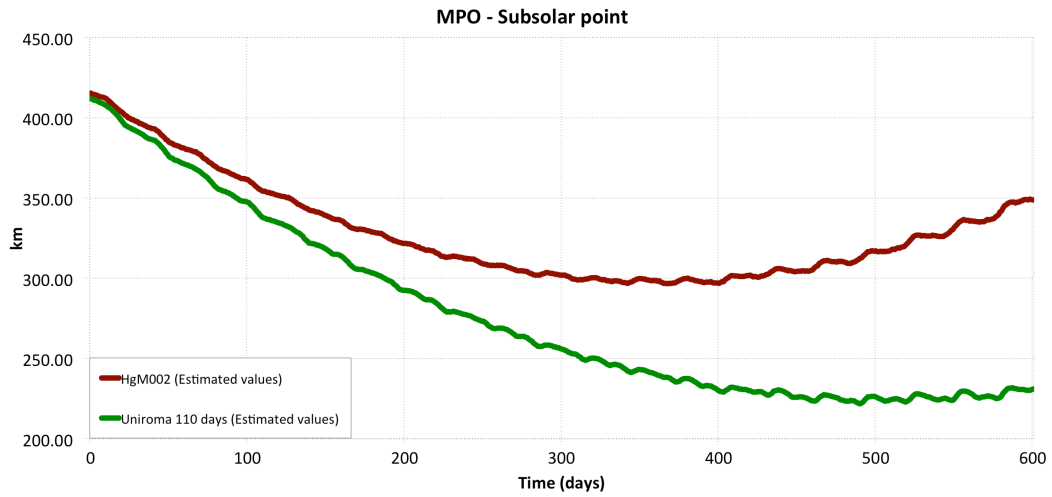

Figure 5.8 MPO subsolar point altitude during the mission

The European Space Agency concerned about this possible orbital evolution is assessing different solutions considering the demanding economic and scientific constraints. Garcia (2010) pointed out two possible orbital configurations that were called North and South approaches. Both mission scenarios rely on the final Mercury approach before insertion into orbit of both spacecraft. The North and South approaches of MPO and MMO differ only in longitude of the ascending node and argument of periherm by *180 degrees*. The current orbit design foresees the South approach with initial $\Omega_S=67.7°$ and $\omega_S=16°$ for MPO. Therefore, the North approach, with initial $\Omega_N=247.7°$ and $\omega_N=196°$ for MPO, resolves easly the orbital evolution problems due to the secular perturbations. The high argument of pericenter would warrant a decrease of the orbit

eccentricity so that the pericenter tend to higher altitudes. Although this solution would fully fulfill the economic and scientific constraints of the European Space Agency, it does not satisfy JAXA requirements. The MMO is equipped with Star Trackers for the precise attitude reconstruction during the orbit. These attitude sensors use different star maps to recognize costellations system leading to accurate determination of the spacecraft orientation. The Star Trackers of the MMO are already provided by elaborated maps of the sky nortern hemisphere that will be continously pointed by the sensor during the orbit in a south pole approach. The drastical change of the orbital approach requires a considerable update of the star maps for the sky southern hemisphere. However, the pressing scheduling of the mission operations does not allow making this solution possible.

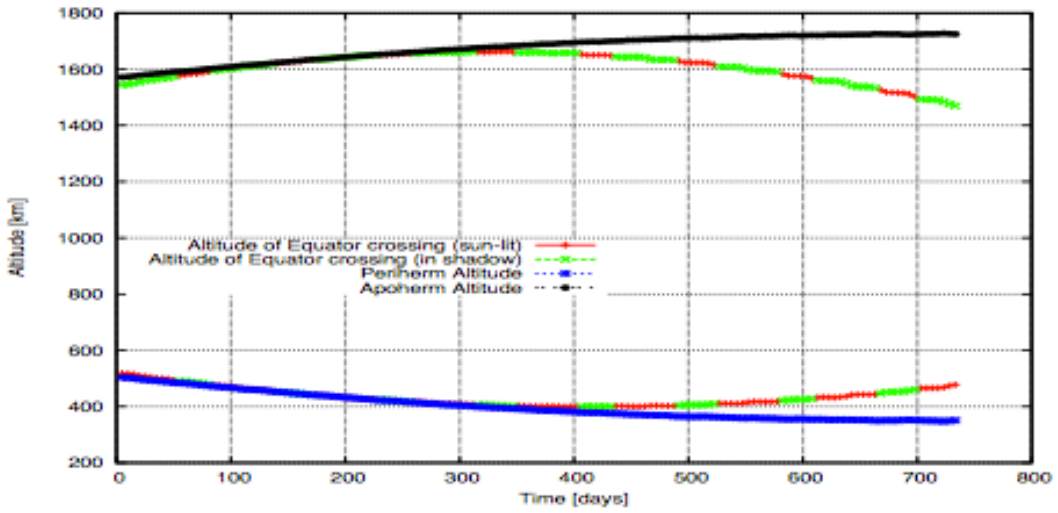

Figure 5.9 MPO altitude at equator crossing for a South pole approach to an initial *505×1570 km* orbit (Jehn, 2012)

The agency is so assessing the feasibility of other two options in order to solve this critical issue. The storage of additional propellant for orbital maneuvers that correct periodically the orbital parameters is for the time ruled-out. Although this option has the advantage of maintaining unchanged the mission scientific goals, the current lift-off mass of the composite spacecraft exceed the maximum weight threshold of the launch vehicle (Ariane 5). Therefore, there are not any margins to store more propellant on board the MPO. The more plausible solution for the spacecraft thermal safety is a small change in the initial periherm and apoherm altitudes. Starting from higher pericenter altitudes allows not come through the thermal limit of *350 km* at the subsolar point because of the gravitational perturbations. The ESA navigation team is studying different possible MPO orbits that not only satisfy the thermal resistance requirements but also do not penalize the mission scientific goals. Jehn (2012) pointed out an initial MPO orbit characterized by

a periherm altitude of about *500 km* that satisfy both thermal and scientific requirements. Figure 5.9 shows the altitude at equator with an initial *505x1570 km* polar orbit highlighting that the subsolar point does not reach altitudes lower than *400 km*.

Unfortunately, the current MESSENGER radio tracking data are not sufficient to determine accurately the evolution of the MPO periherm and subsolar point altitudes, as shown in Figure 5.7-C. However, the recent mission extension till 2013 and the planned change of eccentricity could help breaking up or reducing some of the correlations that currently affect the gravity solutions and subsequently the MPO orbit evolution. The additional data could converge to lower uncertainties in the harmonic coefficients C_{50}, C_{60} and C_{70}, which are also important in producing secular effects. Those coefficients are still not well determined, as the formal uncertainties are larger than the estimated values. In March 2012, NASA brought down considerably MESSENGER apocenter altitude to about *10 000 km* with the same pericenter altitude higher in the northern hemisphere at about *80°N*. The new orbit configuration is still not suitable to an accurate mapping of Mercury's southern hemisphere. However, the analysis of new MESSENGER data could be therefore crucial to improve the knowledge of gravity field coefficients for an accurate prediction of the MPO orbit evolution.

Chapter 6

Conclusions

The thesis has presented the research results obtained from focusing on the task to define a geodetic model of Mercury from the MESSENGER radio science data. We have developed orbit determination procedures able to provide a model of Mercury's gravity field. The estimated degree *2* shows consistency with the HgM002 solution (Smith et al., 2012), supporting the proposed value of the moment of inertia factor and the ensuing indication of a large core. Indeed, C_{20} and C_{22} provide important constraints on the interior structure of Mercury because they are directly related to the radial density distribution. Earth-based radar measurements of Mercury's pole position confirm that the planet occupies a Cassini state in which the axis of rotation remains coplanar with the orbit normal and the normal to the Laplace plane as the spin vector and the orbit normal precess together about the latter with a period of *~300 000-year*. The occupancy of a Cassini state allows the determination of the dimensionless polar moment of inertia from Mercury's obliquity, *2.06±0.1 arcmin* (Margot, 2009), and the quadrupole coefficients C_{20} and C_{22}. Radar observations also show that the amplitude of the *88-day* physical libration in longitude is so large that the mantle and the crust must be librating independently from the core. The decoupling between the mantle and core gives the relationship that connects the polar moment of inertia of the mantle with the libration amplitude in longitude, *35.8±2 arcseconds* (Margot, 2009). The estimated C_{20} and C_{22} provide the information necessary to estimate $C/MR^2=0.354 \pm 0.017$ and $C_m/C=0.450 \pm 0.033$, which strongly indicate the presence of the liquid portion of the outer core.

One of the main goals of our work was the estimation of Mercury's gravity field coefficients in order to provide an accurate prediction of BepiColombo orbit evolution. The ESA dual-spacecraft mission foresees an orbital configuration that relies obviously on the gravity perturbations and the third body effect due to the Sun. Both probes will be inserted into polar eccentric orbits with pericenter altitudes of about 400 km. The

Mercury Magnetospheric Orbiter, a spinning spacecraft for studying the magnetosphere of Mercury, will be into an orbit of high eccentricity so the third body effect due to the Sun is dominant. The Mercury Planetary Orbiter, a three-axis stabilized and nadir pointing spacecraft with an instrument suite of *11* instruments dedicated to remote sensing, will be into a low eccentric orbit so the gravitational perturbations are dominant.

Differently from the approach presented in the HgM002 solution (Smith et al., 2012), our MESSENGER radio tracking data analysis of the first six months was carried out with no a priori of gravity field coefficients up to degree *7*. Both HgM002 and our solution provide fully consistent representations of the gravity field in the northern polar region (Figure 5.2). Indeed, the MESSENGER orbital geometry, with its large eccentricity and the pericenter at *~60°N*, allows an excellent determination of the gravity field only at high northern latitudes. Figure 5.1-C shows the high uncertainties of the surface gravity anomalies in the southern hemisphere that extremely jeopardize the estimation of zonal harmonic coefficients.

The main effects of the Hermean gravity field on the Mercury Planetary Orbiter are secular perturbations of the eccentricity and the argument of pericenter (Figure 5.7). The spacecraft thermal resistance requires severe tolerance on the subsolar point that depends essentially on these two orbital parameters. The combined variations of the eccentricity and the argument of pericenter determine significant change of the subsolar altitude. The current spacecraft design determines a threshold of the altitude on the equator of about *350 km* that represents the minimum height at which the spacecraft instrumentation may survive. The high value of C_{30} in both HgM002 and our solution brings the spacecraft over and below the threshold (Figure 5.7-C). The actual recovered Mercury's gravity field therefore jeopardizes not only the possible extended year but also the nominal mission.

The estimation of the Hermean gravity field, however, is still strongly uncertain because of the unfavorable orbital configuration of the MESSENGER spacecraft. The high uncertainties of the zonal harmonics provide a wide range of possible evolutions of the MPO pericenter altitude. In *Section 5.3.3*, we reported on the propagation of pericenter altitude central value and formal uncertainty considering the covariance matrix of the estimated gravity field coefficients carried out in our solution. Figure 5.7-C shows uncertainties of about *±70 km* (*10-*σ) highlighting poor reliability in the prediction of the minimum distance between MPO and Mercury's surface. The high anti-correlation of the zonal harmonic coefficients (Table 5.5), due to MESSENGER low coverage of the southern hemisphere, causes this wide uncertainty region that may lead to different mission scenarios.

The European Space Agency aims therefore to solve this critical issue according to economic and scientific requirements. Although additional propellant for orbit correction maneuvers may be the trivial solution, the current lift-off mass of the composite exceeds considerably the maximum acceptable weight of the launcher vehicle Ariane 5. A more feasible solution that guarantees the spacecraft thermal resistance is an initial orbit with higher periherm and apoherm altitudes. Indeed, the ESA navigation team is investigating

on different possible MPO orbits that not only fulfill the thermal resistance requirements but also do not penalize the mission scientific goals. The current BepiColombo orbital configuration, presented in *Section 4.1*, fully satisfies the overall scientific goals of the instrumental suites on board both spacecraft. The MPO orbit was opportunely selected to cover the surface of Mercury with high-resolution images and to estimate accurately the Hermean gravity field up to degree *25*. In *Chapter 4*, we reported on the state-of-the-art of the gravity experiment showing the numerical simulations that provide updated realistic estimate of the uncertainties in the determination of Mercury's gravity field (with relative accuracy of about 10^{-4} for degree *2* to 10^{-1} for degree *20*), geoid (accurate at *2-3 cm* over spatial scales of *300 km*) and the tidal Love number k_2 (*1-2%* of relative accuracy). The correction of the initial orbital configuration that satisfies thermal requirements must meet gravity and imaging resolution keeping unchanged these scientific goals. Although Jehn (2012) pointed out an initial MPO orbit characterized by a periherm altitude of about *500 km* that could fulfill both thermal and scientific requirements, the actual knowledge of the Hermean gravity field does not allow propagating accurately the MPO orbit evolution.

In March 2012, the MESSENGER orbit underwent a significant change of the eccentricity, with a corresponding decrease of the apocenter altitude. The orbit period has been reduced to ~*8h*, while the line of apsides and the pericenter altitude did not change significantly. Although these changes allowed only a better coverage of the high latitudes, the reduction of the spacecraft altitudes at the equator and over the southern hemisphere should reduce the correlations of the zonal harmonics and lead to a more stable solution.

The main future work will be therefore the inclusion of these new data in the solution that could carry out an improved model of Mercury's gravity field and lead to more reliable predictions of the MPO orbit evolution. The refinement of the gravity field coefficients, especially the zonal harmonics, could allow the ESA navigation team to correct the designed orbital configuration fully satisfying both thermal and scientific requirements.

Bibliography

Acuna, M. H., et al. "Global Distribution of Crustal Magnetization Discovered by the Mars Global Surveyor MAG/ER Experiment." *Science* 284, 1999: 790-793.

Aharonson, O., M. T. Zuber, and S. C. Solomon. "Crustal remanence in an internally magnetized non-uniform shell: a possible source for Mercury's magnetic field?" *Earth and Planetary Science Letters* (Elsevier) 218, no. 3 (2004): 261-268.

Anderson, B. J., et al. "The Global Magnetic Field of Mercury from MESSENGER Orbital Observations." *Science*, 2011: 1860-1862.

Anderson, B. J., et al. "The Magnetometer Instrument on MESSENGER." *Space Sci. Rev.*, 2007: 417-450.

Anderson, J. D., G. Colombo, P. B. Esposito, E. L. Lau, and G. B. Trager. "The Mass, Gravity Field, and Ephemeris of Mercury." *Icarus*, 1987: 337-349.

Andrews, G. B., et al. "The Energetic Particle and Plasma Spectrometer Instrument on the MESSENGER Spacecraft." *Space Sci. Rev.*, 2007: 523-556.

Asmar, S. W., et al. "Planetary Radio Science: Investigations of Interiors, Surfaces, Atmospheres, Rings, and Environments." A White Paper submitted to the 2009 Planetary Sciences Decadal Survey, 2009.

Asmar, S. W., J. W. Armstrong, L. Iess, and P. Tortora. *Spacecraft Doppler Tracking: Noise Budget and Accuracy Achievable in Precision Radio Science Observations.* Pasadena CA 91109: Jet Propulsion Laboratory, 2005.

Benkhoff, J., et al. "BepiColombo - Comprehensive exploration of Mercury: Mission overview and science goals." *Planetary and Space Science* (Elsevier) 58 (January 2010): 2-20.

Benz, W., W. L. Slattery, and A. G. W. Cameron. "Collisional stripping of Mercury's mantle." *Icarus*, no. 74 (1988): 516-528.

Berner, J. B., S. H. Bryant, and P. W. Kinman. "Range Measurement as Practiced in the Deep Space Network." Proceedings of the IEEE, 2007.

Bertotti, B., G. Comoretto, and L. Iess. "Doppler tracking of spacecraft with multifrequency links." *Astronomy and Astrophysics* 269 (1993): 608-616.

Bertotti, B., L. Iess, and P. Tortora. "A test of general relativity using radio links with the Cassini spacecraft." *Nature* 425 (2003): 374-376.

Bida, T. A., R. M. Killen, and T. H. Morgan. "Discovery of calcium in Mercury's atmosphere." *Nature* 404 (2000): 159-161.

Boyton, W. V., et al. "MESSENGER and the Chemestry of Mercury's Surface." *Space and Science Reviews*, 2007: 85-104.

Broadfoot, A. L., D. E. Shemansky, and S. Kumar. "Mariner 10: Mercury Atmosphere." *Geophys. Res. Lett.* 3 (1976): 577-580.

Cameron, A. G. W. "Formation of the prelunar accretion disk." *Icarus* 62 (1985): 319-327.

Cavanaugh, J. E., et al. "The Mercury Laser Altimeter Instrument for the MESSENGER Mission." *Space Sci. Rev.*, 2007: 451-479.

Coffey, J. *Mercury Magnetic Field.* 07 07, 2011. http://www.universetoday.com/35873/mercury-magnetic-field/.

Colombo, G. "On the rotational period of the planet Mercury." *Nature*, 1965: 575-577.

COMPLEX. "1990 Update to Strategy for Exploration of the Inner Planets." *Committee on Lunar and Planetary Exploration.* Washington: National Academy Press, 1990. 47 .

COMPLEX. "Strategy for Exploration of the Inner Planets: 1977-1987." *Committee on Lunar and Planetary Exploration.* Washington: National Academy of Sciences, 1978. 97.

Connerney, J. E. P., and N. F. Ness. *Mercury's magnetic field and interior.* Tucson, AZ: F. Vilas, C.R. Chapman, M.S. Matthews (Eds.), Mercury, University of Arizona Press, 1988, 494-513.

Domingue, D. L., et al. "Mercury's Atmosphere: A Surface-Bounded Exosphere." *Space Science Reviews* 131, no. 1-4 (2007): 161-186.

Fegley Jr., B., and A. G. W. Cameron. "A vaporization model for iron/silicate fractionation in the Mercury proto planet." *Earth and Planetary Science Letters*, 1987: 207-222.

Garcia, D., R. Jehn, J. Schoenmaekers, and P. de Pascale. "BepiColombo Mercury Cornestone." Consolidate Report on Mission Analysis, ESOC, Robert-Bosch-Str. 5, 64293 Darmstadt, Germany, 2010.

Genova, A., M. Marabucci, and L. Iess. "A batch sequential filter for the orbit determination of the BepiColombo radio science experiment." *Journal of Aerospace Engineering Sciences and Applications* 4, 2012: 17-30.

Goldsten , J. O., et al. "The MESSENGER Gamma-Ray and Neutron Spectrometer." *Space Sci. Rev.*, 2007: 339-391.

Harmon, J. K., and M. A. Slade. *Science* 258 (1992): 640-642.

Hawkins, S. E., et al. "The Mercury Dual Imaging System on the MESSENGER Spacecraft." *Space Sci. Rev.*, 2007: 247-338.

Hayakawa, H., Y. Kasaba, H. Yamakawa, H. Ogawa, and T. Mukai. *Adv. Space Res.*, 2004: 2142-2146.

Hide, R. "Fluctuations in the Earth's rotation and the topography of the core-mantle interface." *Phil. Trans. Royal Soc. London* A328 (1989): 351-363.

Iafolla, V., and S. Nozzoli. "Italian spring accelerometer (ISA) a high sensitive accelerometer for "BepiColombo" ESA CORNERSTONE." *Planetary and Space Science*, 2001: 1609-1617.

Iess, L., and G. Boscagli. "Advanced radio science instrumentation for the mission BepiColombo to Mercury." *Planet. Space Sci.* 49 (2001): 1567-1608.

Iess, L., et al. "ASTRA interdisciplinary study on enhancement of end-to-end Accuracy for Spacecraft TRAcking techniques." Technical Note 1, Rome, 2012.

Jehn, R. *Orbit Evolution of BepiColombo's MPO and MMO spacecraft.* MAS Technical Note No.86, Robert-Bosch-Str. 5, 64293 Darmstadt, Germany: ESOC, 2012.

Kabin, K., et al. "Global MHD modeling of Mercury's magnetosphere with applications to the MESSENGER mission and dynamo theory." *Icarus*, 2008: 1-15.

Kaula, W. M. *Theory of Satellite Geodesy.* Waltham: Blaidesdell, 1966.

Killen, R. M., A. Potter , A. Fitzsimmons, and T. H. Morgan. "Sodium D2 line profiles: clues to the temperature structure of Mercury's exosphere." *Planetary and Space Science* (Elsevier) 47, no. 12 (1999): 1449-1458.

Killen, R. M., et al. "Evidence for space weather at Mercury." *Journal of Geophysical Research* 106, no. E9 (2001): 20.

Kortenkamp, S. J., E. Kokubo, and S. J. Weidenschilling. "Formation of planetary embryos." *Origin of the Earth and Moon*, 2000: 85-100.

Korth, H., et al. "Determination of the properties of Mercury's magnetic field by the MESSENGER mission." *Planetary and Space Science*, 2004: 733-746.

Leary, J. C., et al. "The MESSENGER Spacecraft." *Space Sci. Rev.*, 2007: 187-217.

Lewis, J. S. *Origin and Composition of Mercury.* Mercury, Tucson: F.Vilas, C.R. Chapman, M.S. Matthews (University of Arizona Press), 1988, 651-669.

Lewis, J. S. "Physics and chemistry of the solar system." 446-447. Elsevier Academic Press, 2004.

Margot, J.-L. "A Mercury orientation model including non-zero obliquity and librations." *Celest. Mech. Dyn. Astr.*, 2009: 329-336.

Margot, J.-L., S. J. Peale, R. F. Jurgens, M. A. Slade, and I. V. Holin. "Large Longitude Libration of Mercury Reveals a Molten Core." *Science*, 2007: 710-714.

Margot, J.-L., S. Padovan, S. J. Peale, and S. C. Solomon. "Abstract P41A-1573." *American Geophysical Union Fall Meeting.* San Francisco, CA, 2011.

McAdams, R. W., R. W. Farquhar, A. H. Taylor, and B. G. Williams. "MESSENGER Mission Design and Navigation." *Space Sci. Rev.*, 2007: 219-246.

McClintock, W. E., and M. R. Lankton. "The Mercury Atmospheric and Surface Composition Spectrometer for the MESSENGER Mission." *Space Sci. Rev.*, 2007: 481-521.

McClintock, W. E., et al. "MESSENGER observations of Mercury's exosphere: detection of magnesium and distribution of constituents." *Science* 324 (2009): 610-613.

McNutt Jr., R. L., S. C. Solomon, R. Grard, M. Novara, and T. Mukai. "An international program for Mercury exploration: sinergy of MESSENGER and BepiColombo." *Advances in Space Research* (Elsevier), 2004: 2126-2132.

Milani, A., A. Rossi, D. Vokrouhlicky, D. Villani, and C. Bonanno. "Gravity field and rotation state of Mercury from the BepiColombo Radio Science Experiments." *Planetary and Space Science*, 2001: 1579-1596.

Milani, A., and G. F. Gronchi. *The theory of orbit determination.* Cambridge University Press, 2008.

Ness, N. F., K. W. Behannon, R. P. Lepping, and Y. C. Whang. "Observations of Mercury's magnetic field." *Icarus* 28 (1976): 479-488.

Ness, N. F., K. W. Behannon, R. P. Lepping, and Y. C. Whang. "The magnetic field of Mercury." *J. Geophys. Res.* 80 (1975): 2708-2716.

Ness, N. F., K. W. Behannon, R. P. Lepping, Y. C. Whang, and K. H. Schatten. "Magnetic field observaions near Mercury: Preliminary results from Mariner 10." *Science* 185 (1974): 151-160.

Neukum, G., J. Oberst, H. Hoffmann, R. Wagner, and B. A. Ivanov. "Geologic evolution and cratering history of Mercury ." *Planet. Space Sci.*, 2001: 1507-1521.

Peale, S. J. "Does Mercury have a molten core?" *Nature* 262 (1976): 765-766.

Peale, S. J. *Rotational dynamics of Mercury and the state of its core.* IN: Mercury (A89-43751 19-91), Tucson, AZ: University of Arizona press, 1988, 461-493.

Peale, S. J. *The Proximity of Mercury's Spin to Cassini State 1.* Santa Barbara, CA 93106: Department of Physics, University of California, 2005.

Peale, S. J., R. J. Phillips, S. C. Solomon, D. E. Smith, and M. T. Zuber. "A procedure for determining the nature of Mercury's core." *Meteoritics & Planetary Science*, 2002: 1269-1283.

Potter, A. E., and T. H. Morgan. "Discovery of sodium in the atmosphere of Mercury." *Science*, no. 229 (1985): 651-653.

Potter, A. E., and T. H. Morgan. "Potassium in the atmosphere of Mercury." *Icarus* 67 (1986): 336-340.

Prockter, L. M., et al. "Evidence for Young Volcanism on Mercury from the Third MESSENGER Flyby." *Science*, 2010: 668-671.

Schlemm II, C. E., et al. "The X-Ray Spectrometer on the MESSENGER Spacecraft." *Space Sci. Rev.*, 2007: 393-415.

Schubert, G., M. N. Ross, D. J. Stevenson, and T. Spohn. *Mercury's thermal history and the generation of its magnetic field.* Mercury, Tucson, Az.: F.Vilas et al., Univ. Ariz. Press, 1988.

Schulte, H.-R. "RSE DeltaV Requirement Identification." *BC-ASD-TN-xxxxx.* EADS ASTRIUM, 2009.

Schulz, R., and J. Benkhoff. "BepiColombo: payload and mission updates." *Advances in Space Research* 38 (2006): 572-577.

Smith, D. E., et al. "Gravity Field and Internal Structure of Mercury from MESSENGER." *Science*, 2012: 214-217.

Solomon, S. C., R. L. McNutt, Jr., R. E. Gold, and D. L. Domingue. "MESSENGER Mission Overview." *Space Sci. Rev.*, 2007: 3-39.

Spohn, T., et al. "BELA - The BepiColombo Laser Altimeter." *SAO/NASA ADS Astronomy*, 2005.

Sprague, A. L., W. J. Schmitt, and R. E. Hill. "Mercury: Sodium atmospheric enhancements, radar-bright spots, and visible surface features." *Icarus* 136 (1998): 60-68.

Srinivasan, M. E., M. E. Perry, K. B. Fielhauer, D. E. Smith, and M. T. Zuber. "The Radio Frequency Subsystem and Radio Science on the MESSENGER Mission." *Space Sci. Rev.*, 2007: 557-571.

Stevenson, D. J. "Planetary magnetic fields." *Earth Planet. Sci.* , 2003: 1-11.

Stevenson, D. J. "Planetary science: Mercury's mysteries start to unfold." *Nature*, 2012: 52-53.

Tapley, B. D. *Fundamentals of Orbit Determination.* New York, NY: Springer-Verlag, 1989.

Tapley, B. D., B. E. Schutz, and G. H. Born. *Statistical Orbit Determination.* New York, NY: Elsevier Academic Press, 2004.

Tortora, P., L. Iess, J. J. Bordi, J. E. Ekelund, and D. C. Roth. "Precise Cassini navigation during solar conjuction through multifrequency plasma calibrations." *J. Guidance Control Dyn.* 27 (2004): 251-257.

Vallado, D. A. *Fundamentals of Astrodynamics and Applications.* Microcosm Press - Springer, 2007.

van Casteren, J., and M. Novara. *BepiColombo Mission.* 2200 AG Noordwijk, The Netherlands: ESA/ESTEC, 2010.

Vaughan, R. M., D. R. Haley, S. Shapiro Hongxing, and J. O'Shaunghnessy D. *Momentum Management for the MESSENGER Mission.* AAS 01-380, Laurel, Maryland: The Johns Hopkins University Applied Physiscs Laboratory, 2002.

Weidenschilling, S. J. "Iron/silicate fractionation and the origin of Mercury." *Icarus* 35 (1978): 99-111.

Weidenschilling, S. J., and J. N. Cuzzi. "Formation of planetesimals in the solar nebula." *Protostars and Planets III* (ed. by E.H. Levy, J.I. Lunine (University of Arizona Press, Tucson)), 1993: 1031-1060.

Wetherill, G. W. "Provenance of the terrestrial planets." *Geochimica et Cosmochiminica Acta*, no. 58 (1994): 4513-4520.

Yamakawa, H., H. Ogawa, Y. Kasaba, H. Hayakawa, T. Mukai, and M. Adachi. "Current status of the BepiColombo/MMO spacecraft design." *Advances in Space Research*, 2004: 2133-2141.

Zuber, M. T., et al. "Topography of the Northern Hemisphere of Mercury from MESSENGER Laser Altimeter." *Science*, 2012: 217-220.

Zurbuchen, T. H., et al. "MESSENGER observations of the composition of Mercury's ionized exosphere and plasma environment." *Science* 321 (2008): 90-92.